THE DEVELOPMENT OF GENETICALLY ENCODED IMAGING METHODS TO STUDY REDOX STATE AND MATURATION OF CYTOCHROME *C* PROTEIN

by

SELEN MANİOĞLU

A Thesis Submitted to the
Graduate School of Engineering
in Partial Fulfillment of the Requirements for
the Degree of

Master of Science
in
Biomedical Science and Engineering

KOC UNIVERSITY
JUNE 2016

Koç University

Graduate School of Sciences and Engineering

This is to certify that I have examined this copy of a master's thesis by

Selen Manioğlu

and have found that it is complete and satisfactory in all respects,
and that any and all revisions required by the final
examining committee have been made.

Committee Members:

_____

Halil Bayraktar, Ph.D. (Advisor)

_____

Alper Kiraz, Ph.D.

_____

Yasin Karadağ, Ph.D.

Date: _____

ABSTRACT

Genetically encoded fluorescent reporters for biological signaling and advance microscopy techniques play a key role to elucidate the mechanism of changes in cells under oxidative stress, therefore provide quantitative methods to monitor signaling and measure response to external stimuli at higher spatiotemporal resolution. The use of these methods is highly preferable due to their low toxicity, high signal-to-noise ratio, allowing signal detection from various cell types and specificity for complex biological pathways.

Redox mechanism is an essential pathway for living organisms in order to maintain and preserve biological homeostasis. It fulfills the completion of respiratory chain for energy production, cellular reduction, and regulation of free radical species and initiation of apoptosis. Oxidative damage and unbalanced redox propagation can facilitate deleterious situations like aging, neurodegenerative diseases, and hypoxia. Thus, a better understanding of redox mechanism included structures can reveal invaluable information on its interplay in intracellular signaling.

Cytochrome *c* (Cyt *c*), a member of redox active heme proteins family, is localized in the inner membrane of mitochondria where a great number of intracellular redox reactions take place. Its main function is to transfer electrons across mitochondria's membrane in electron transport chain of adenosine triphosphate (ATP) production. Therefore, the key role of Cyt *c* in mitochondria's redox mechanism highlights it as a good candidate for advancing our knowledge on the redox biogenesis and lead the way to the diagnosis and treatment of many redox mechanism related diseases.

Here, we demonstrated a method for monitoring and determining the redox state of Cyt *c* in microbial purified proteins and studied the maturation and interaction of Cyt *c* with Cyt *c* heme lyase in living cells with fluorescence resonance energy transfer (FRET). The oxidation state of Cyt *c* was determined through the photochromic FRET (pcFRET) method where the emission of the fluorescent reporter attached to Cyt *c* was modulated by the redox state driven absorption changes of Cyt *c*. The continuous changes of Cyt *c* oxidation state induced by various redox compounds were clearly demonstrated. Finally, we studied the heme lyase induced hemin insertion and folding of Cyt *c* in living cells and redox protein interactions by using a single-cell fluorescence signal tracking method. We also reported a novel method of frame-by-frame, fluorophore coefficient corrected FRET tracking for the characterization of the retrieved signal coming directly from living cells.

ÖZET

Biyolojik imleşim ve ileri mikroskobik görüntüleme teknikleri için kullanılan genetik olarak şifrelenen floresan habercileri, oksidatif stres altında hücrede gerçekleşen değişim mekanizmalarını açıklamada önemli bir rol oynarlar. Bu sebeple imleşimin görüntülenmesi ve dışarıdan gelen uyarıcıya verilen tepkinin yüksek uzamsal zaman çözünürlüğünde ölçülmesi için sayısal metotlar sağlar. Düşük toksiklik, yüksek imleşim-parazit oranı farklı hücre tiplerinden imleşim alabilme ve kompleks biyolojik yollarda hassasiyet gibi özelliklerinden ötürü bu metodlar çokça tercih edilmektedir.

Canlı organizmaların dengeleşimlerini sağlaması ve koruması için redoks mekanizması önemli bir metobolik yoldur. Görevleri arasında enerji üretimi solunum çemberini tamamlamak hücresel redüksiyon özgür radikallerin düzenlenmesi ve apaptoziz başlatılması yer alır. Oksidatif hasar ve dengesiz redoks yayılımı yaşlanma, nörodejaneratif hastalıklar ve hipoksi gibi istenmeyen sonuçlara sebebiyet verebilir. Bu yüzden redoks mekanizmasına dahil ögelerin daha iyi anlaşılması hücre içi imleşim görevi hakkında faydalı bilgileri ortaya çıkarabilir.

Redoks aktif demir proteinleri ailesinin bir üyesi olan Cytochrome *c* (Cyt *c*), pek çok hücre içi redoks reaksiyonunun gerçekleştiği mitokondrinin iç membranında bulunmaktadır. Asıl görevi, mitokondrinin membranı üzerinden ATP üretiminde yer alan elektron taşıma çemberine elektron transfer etmektir. Bu yüzden Cyt *c*'nin mitokondrinin redoks mekanizmasındaki kilit rolü, redoks biyogenezini anlamamız için kendisini iyi bir aday olarak

öne çıkarmakta ve redoks mekanizması kaynaklı hastalıkların tanısı ve tedavisine ışık tutmaktadır.

Bu çalışmada mikrobik proteinlerden arındırılmış Cyt *c*'nin redoks durumunun görüntülenmesi ve saptanması gösterilmiş, canlı hücrelerde floresan rezonans enerji transferi (FRET) sayesinde Cyt *c*'nin olgunlaşması ve Cyt *c* Heme Lyase proteiniyle olan etkileşimi çalışılmıştır. Cyt *c*'nin oksidasyon durumu fotokromik FRET (pcFRET) metoduyla tespit edilmiştir ki, bu metotta redoks durumuna bağlı olarak değişiklik gösteren Cyt *c* absorpsiyonu, Cyt *c*'ye bağlı olan floresan habercisinin emisyonunu modüle etmektedir. Cyt *c*'nin farklı redoks bileşenleri ile uyarılan sürekli oksidasyon durumu değişimi açıkça gösterilmiştir. Son olarak canlı hücrelerde Cyt *c*'e heme lyase proteini yardımıyla hemin kofaktörünün yerleştirilmesi, Cyt *c*'nin katlanması ve redoks proteinleri etkileşimleri tek hücre floresan sinyali izleme metoduyla çalışılmıştır. Aynı zamanda canlı hücrelerden direkt olarak alınan sinyalin karakterizasyonu için her resimde düzeltilmiş florofor katsayısı kullanan orijinal bir FRET izleme metodu raporlanmıştır.

ACKNOWLEDGEMENTS

I am deeply grateful to my advisor Dr. Halil Bayraktar for the guidance he had given throughout the past five years and for the opportunity to join his research group. I would like thank him for his continuous support and valuable consultation in the course of my dissertation and contribution to my development as a researcher. I was lucky to have him as my mentor for learning the substantial academic skills I had to practice today and tomorrow.

I am thankful to Dr. Erdem Alaca for supporting my master studies unconditionally and I also would like to thank my thesis committee members for their valuable contributions and comments.

I am very proud to be a member of Koc University family and therefore I would like to express my appreciation to Ayşe Abla for her warm kindness all the time, Nesrin Atağ and GSSE office members for their assistance in all time consuming paperwork of mine. I am grateful to Koç University and Foundation for providing me this productive scientific environment and research facilities.

My sincere thanks also goes to my former lab mates Müge Atış and Begüm Akalın who were my first colleagues to work, travel and have a great time in graduate school. Their presence in the lab was an indescribable support and joy for me. I also thank to our new member Ateeq Ur Rehman who accompanied me in the lab this year.

I really appreciate the entertaining chocolate rituals of Göktuğ Gönel and extreme incentive of Berkay Yılmaz that convinced me to move on. My dear neighbor Deniz Çonkar was always there to find me what I need and Adeel Afridi was kind enough to listen me for

long hours during our coffee sessions. Apart from their unconditioned support and encouragement all the time, I am really thankful to Artür Manukyan for our rollicking statistics discussions, Haroon Qureshi for his unique tricks and advices in molecular biology and Zeynep Kaya for her limitless help in cell culture related experiments.

In particular, I am grateful to Büşra Harmanda for her irreplaceable motivation and cheer during my difficult times and sharing her brilliant friendship and knowledge with me. Lastly, I offer my heartfelt thanks to Bekir Aksoy for his incredible uplifting optimism and support throughout this year and superhuman patience and understanding in distressing times.

I also want to thank Aunt Elçin and Uncle Uğur Koçak for their sincere concern and contribution to my university studies.

Finally, I must express my very profound gratitude to my family, my mother- Mine, father-Serdar, brother-Sinan for providing me the unfailing support and continuous encouragement throughout my years of study and through the process of researching and writing this thesis. This accomplishment would not have been possible without them. Thank you.

This work was financially supported by the Scientific and Technological Research Council of Turkey (TUBITAK) under Grants 112T823, and 112E580.

TABLE OF CONTENTS

LIST OF TABLES

LIST OF FIGURES

NOMENCLATURE

Cyt *c*	Cytochrome *c*
ATP	Adenosine triphosphate
FRET	Fluorescence resonance energy transfer
pcFRET	Photochromic fluorescence resonance energy transfer
GFP	Green fluorescent protein
FP	Fluorescent protein
GCaMP	Genetically encoded calcium modulating protein
CaM	Calmodulin
CID	Chemically inducible dimerization
ChR2	Channelrhodopsin-2
NpHR	Halorhodopsin
ROS	Reactive oxygen species
OXPHOS	Oxidative phosphorylation system
mETC	Mitochondrial electron transport chain
IMS	Inter membrane space
Complex III	Cytochrome *c* reductase
Complex IV	Cytchrome *c* oxidase, CcO
Apo-Cyt *c*	Apo-Cytochrome *c*
DTT	Dithiothretiol
E	FRET efficiency
J	Spectral overlap
F_v	Normalized Venus emission spectrum
$\varepsilon_{Cyt\ c}$	Cyt *c* molar extinction coefficient.
Φ_D	Fluorescent quantum yield of the donor
R_0	Förster radius
EMCCD	Electron multiplying charge coupled device
IF	Immunofluorescence

I_{FRET}	FRET channel intensity
I_{CFP}	Donor channel intensity
I_{YFP}	Acceptor channel intensity
n_{FRET}	Net FRET
r_{FRET}	Raw FRET
α	Acceptor correction coefficient
β	Donor correction coefficient
NFRET	Normalized FRET

Chapter 1 : INTRODUCTION

As a central hub for redox pathway, mitochondria harbors numerous protein members that actively facilitate the major part of the whole mechanism and maintain the continuity of engaged processes. Cyt *c* is one of the crucial subunits found in the inner membrane of mitochondria. It is responsible for the perpetuity of the electron transport chain in ATP production by transferring electrons and initiating the apoptotic activation cascade by its release to cytosol. Considering its substantial contributions to biological persistence and expiration, the highly conserved genetic material of Cyt *c* across the spectrum of species provides not just a glimpse into evolutionary biology but brings it forward as a useful redox mechanism reporter candidate.

The recent studies on redox biogenesis revealed its significance on serious biological irregularities such as ageing, apoptosis, neurodegenerative diseases, under developed skeletal systems and cancer metastasis. However, developing a sufficient treatment for these disorders requires detailed information on the intracellular dynamics of the mechanism to have an appreciable diagnosis. The intricate and correlative structure of the redox mechanism provide major challenges to design a target specific and robust reporter for studying its subcomponents individually.

Despite the challenges, developments in microscopy and molecular biology fields gave rise to novel tools like a genetically encoded sensor and probes having high spatio-temporal resolution at the cellular level than conventional methods, similar genetic material of the system to increase target specificity and multiple triggering modes open to progression and modification for a specific case. Therefore, utilizing genetically encoded tools and their

derivatives may help us to advance our knowledge on the intracellular signaling taking place between the sub members of redox biogenesis.

In this study, we give a review of genetically encoded techniques for monitoring intracellular activities along with the vital presence of the redox mechanism and its pivotal member, Cyt c, for our biological sustainability. Later, we present two genetically encoded reporter design models for estimating the redox state of Cyt *c*.

Chapter 2 provides a literature review on the designing aspect and applications of genetically encoded tools for studying biological processes, the importance of redox biogenesis for cell homeostasis and the key role of Cyt *c* in mitochondria's redox cycle as a promising candidate for a mechanism reporter.

Chapter 3 describes the design and operation of genetically encoded pcFRET technique for direct redox state measurement of Cyt *c* in purified microbial proteins. The physical phenomena of the method is explained and experiments for monitoring the oxidation state of Cyt *c* are performed for displaying the quantitative and qualitative strength of the technique.

Chapter 4 details the genetic design, implementation in live cell microscopy experiments with mammalian cells and signal characterization of FRET methodology based samples for studying the interplay of Cyt *c* protein, the redox state determiner cofactor and catalyzer protein Cyt *c* heme lyase in folding mediated protein maturation. The fundamental findings underlying the crosstalk between folding components are discussed. A robust method for the characterization of the retrieved FRET signal coming directly from the cells, corrected for fluorophore coefficient, and tracked for a number of consecutive frames is also proposed and explained.

In this thesis, a summary of the accomplished work is reported and an outlook on the future directions is given.

Chapter 2 : LITERATURE REVIEW

2.1. Genetically encoded tools for studying cellular signaling network

Living systems embody a complex inter- and intracellular communication for adapting to continuous changes in their environment. The efficiency of this complex communication relies upon the utilization of highly concerted signal transduction networks, responsible for converting input signals retrieved from the outside and generating a corresponding cellular response. These specific response constituting networks involve countless signaling molecules, such as ligands, kinases, phosphatases, secondary messengers, etc. having meticulous space and time control over their dynamics[1,2]. The delicate presence of this strict spatiotemporal control in signal transduction is sustained with the activation of numerous molecular mechanisms which ensure the cell's control over its dynamics, intracellular trafficking, metabolism and gene expression. As an example, scaffold proteins act as pacemakers in the partitioning of multiple signaling enzymes into specific macromolecular structures and leading these tethered complexes to different subcellular localizations[3,4]. Furthermore, the anchored signaling enzymes may enhance the spatio control over diffusible signaling molecules by amplifying gradient dynamics and micro domains of signaling activity[5,6].

Therefore, it is necessary to anatomize the molecular mechanisms that take part in highly dynamic signal transduction processes in the native setting of a living cell, tissue or organism,

as this ensures the integrity of the entire signaling network with its regulatory mechanisms as well. However, the conventional methods for signal transduction studies, which usually requires cell fixation and lysis processes, are limited in terms of advanced spatiotemporal resolution, and often ignores the biological relevancy of single-cell individuality such as numerous unique oscillations occurring in a cell population. Likewise, classic cell perturbation methods also fail in providing the required spatio and temporal resolution for monitoring the interplay between specific signaling molecules. Hence, a remarkable number of genetically encoded tools have been developed for direct and dynamic visualization of signaling processes in living systems along with target oriented precise manipulations of signaling molecules. Since these novel gadgets have a genetic encoding property, they can be easily and efficiently implemented to living systems as a DNA material. After completing the *de novo* protein synthesis of this genetic sequence, they localize in targeted subcellular compartments and can be tracked through the use of their labeling signals. The hybrid examples of these genetically encoded tools raise the bar for investigating the role of specific signaling mechanisms and molecules in cellular responses[7].

2.1.1. Genetically encoded biosensors for monitoring intracellular signaling networks

Our understanding of signal specificity has been incredibly advanced, since our first real-time studies on signal dynamics in living cells[8]. In the past, chemical dyes were utilized for the optical detection of cellular signaling events. As a relevant example, the fluorescent dye and Ca^{2+} indicator, Fura-2 was extensively employed in the first studies of Ca^{2+} signaling[9] and still stands the test of time as a fluorescent marker for live cell imaging since its invention in the 1980s. However, they are not promoted much due to their viability effective toxicity, non-reversible utilization in long term experiments and high possibility of non-specific

interactions with different regions other than targeted sites which introduces low signal-to-noise ratio problems as well[10].

Another breakthrough discovery in dynamic signal monitoring studies was the discovery of green fluorescent proteins (GFP) by Osamu Shimomura in 1962[11]. GFP is a naturally expressed fluorescent protein in the *Aequorea victoria* jellyfish species. After the isolation of GFP coding DNA sequence, Chalfie and Prasher managed to express GFP outside of *Aequorea victoria* in different model organisms[12,13]. This genetically encoded implementation of FP extended its biological applications since this property enables the linking of GFP to any protein of interest and labeling of protein for fluorescence microscopy experimentation[14]. Furthermore, Tsien introduced different mutations into a GFP sequence that resulted in a color shift of fluorescence emission to other wavelengths, therefore creating a palette of fluorescent proteins that involves the entire visible spectrum from blue to red[15]. In 2008, Shimomura, Tsien and Chalfie were awarded the Nobel Prize in Chemistry for the discovery of GFP and its demonstrated applications in biological studies[16]. Consequently, the advances in FP technology along with improvements in the microscopy field, has facilitated the monitoring of a wide range of signaling networks with augmented spatio-temporal resolution over the past two decades[7]. Hence, an abundance of FP-based biosensors were developed for tracking various signaling molecules such as cyclic nucleotide messengers, ligands, phosphoinositides, kinases, phosphatases and many others[17–19].

In the general design, all biosensors include a sensing element that is matched with a reporting unit. The sensing unit often consists of endogenous proteins or *de novo* peptide sequences that shoots for targeted biochemical activity, whereas a reporting unit involves one or more fluorescent proteins that designate the biochemical state of the sensing element.

In the simplest biosensor design, a single FP that is linked to a protein or protein domain of interest reports the localization of target protein with its fluorescent signal dispersion which does not occur at any innate location. Concurrently, a FP protein can be fused with a sensing domain that specifically binds to a molecule of interest dwelling in the cellular membrane, like pleckstrin homology (PH) of Akt protein that recognizes 3' phosphoinositides residing in the cellular membrane[20]. (Figure 2-1A) Thus, the synthesis or diminishment of the target molecule will determine the probe's localization in or out of the membrane, which can be monitored from the fluorescence intensity change at the compartment of interest.

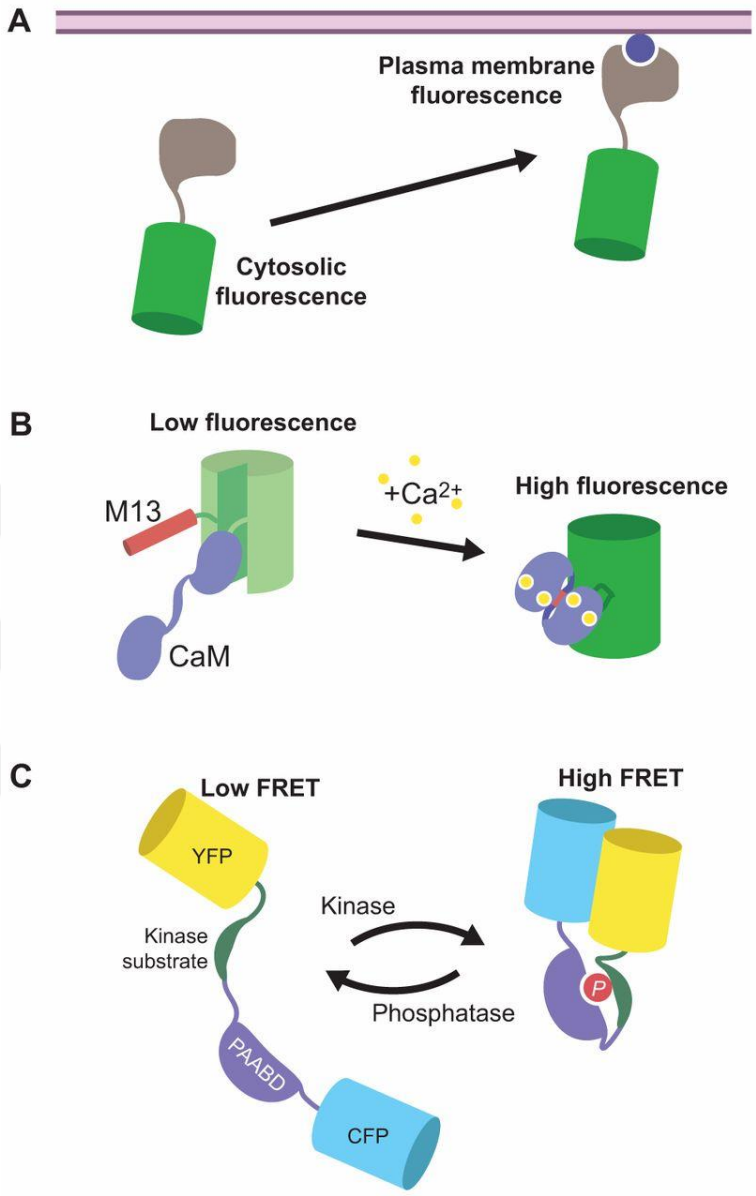

Figure 2-1: Different types of FP-based biosensor designs[7]

Another variant of the single-FP biosensor design benefits from the chromophore's photophysical properties for informing the biological events. In this approach, the sensing unit contains a molecular switch that is embedded in the fluorescent protein. A prominent example of this design, GCaMP, a genetically encoded intensity-based Ca^{2+} indicator, is generated through the fusion of GFP, calmodulin (CaM) and M13[21]. GCaMP comprises a circular permuted version of GFP, derived from connecting the native N- and C- termini of the protein

and generating new termini from its core β-barrel structure. (Figure 2-1B) As for the molecular switch structure, intermediate calcium binding protein CaM and CaM-binding peptide sequence M13 are inserted at the new C- and N- terminus respectively. The x-ray crystallography studies of GCaMP revealed that the chromophore site of the permuted GFP is subjected to a solvent in the calcium-free dark state and, therefore, founded in its protonated form without fluorescence emission. Upon calcium binding, CaM wraps around M13 peptide to give a conformational change in the molecular switch that creates a new domain between CaM and permuted GFP, and somewhat prevents the solvent access to the chromophore site concluding in a high fluorescence intensity and non-pronated form[22]. The convenient but influential working mechanism of GCaMP gave rise to a new palette of intensity-based Ca^{2+} indicators having different shades of FPs spanning from blue to red that covenant a great potential for dynamic multicolor imaging of intracellular signaling[23,24].

Lastly, a greater part of FP-based biosensors characterizes a conventional phenomenon based design where molecular switch structure is sandwiched between two FPs suitable for performing Förster resonance energy transfer (FRET)[25–27]. FRET is a biophysical phenomenon which gives a measure for non-radiative energy transfer between donor and acceptor fluorophores through dipole-dipole coupling. The first requirement for an efficient energy transfer from donor to acceptor is an adequate amount of overlap between the emission spectrum of the donor and the excitation spectrum of the acceptor. Apart from that, a close spatial proximity (<10nm) between two chromophores and correct dipole-dipole orientation are required for energy transfer to occur. In the biosensor design, when the targeted molecules is activated, it undergoes a conformational change which alters the distance and orientation between two fluorophores to generate a FRET signal[28].

The modular feature of these biosensors made them extremely handy tools for incorporating various molecular switch structures where the FRET signal is positively correlated with the proximity between design components. Moreover, FRET biosensors have founded a large place in biomedical studies due to their versatility and provided efficient tools in a fast and standardized manner for quantitative analysis of biological events both in high-throughput and sub-cellular sensitivity[19,29]. As an example, several FRET-based kinase activity reporter (KAR) designs have been made by comprising a kinase-specific substrate to a phosphoamino-acid-binding domain (PAABD) and inserting this molecular switch structure between donor and acceptor FPs. (Figure 2-1C) When the substrate is phosphorylated with collateral kinase, it binds to PAAABD and facilitates a conformational change in the molecular switch structure, therefore, resulting in a FRET signal generation[30–32].

2.1.2. Genetically encoded tools for perturbing biochemical reactions in living systems

Genetically encoded biosensors are substantial reporters for tracking the engendering events in a dynamic and concomitant network where specific signaling molecules are tightly regulated to compose a rational cellular response. But the monitoring of signaling events by itself is not sufficient to possess a spatio-temporal precise control over signaling dynamics. For this reason, genetically encoded perturbation tools promise an invaluable potential to control and manipulate intracellular signaling events with high specificity and spatio-temporal resolution compared to conventional genetic and pharmacological methods. These perturbation tools embody two stimulation techniques that are based on chemically and optically driven molecular switch structures for target specific control of signaling events.

Chemically driven perturbation tools

A large proportion of cellular proteins are processed through oligomerization which is carried out by a variety of mechanisms[33]. Therefore, it is possible have an exact stimulation of separate biochemical events through externally initiated dimerization[34]. Chemically inducible dimerization (CID) is a conventional technique for governing protein synthesis related reactions[35]. In this method, the composite proteins are produced through binding two specifically interacting domains under the existence of rapamycin, an immunosuppressive compound which is relatively straightforward to implement in living systems since protein constituents are already genetically encoded and rapamycin is a small enough molecule that can penetrate through cellular membrane. CID is a common methodology for manipulating the protein activity by means of a displacement driven strategy, wherein the localization of the chimeric protein synthesis shifts from the substrate-poor region to the substrate-rich region upon the introduction of rapamycin. Advanced spatial localization control is achievable with focal activation caged rapamycin as well[36]. For instance, Inoue et al. demonstrated precise and rapid perturbation of Rac enzymatic activity by means of reversible activation and inhibition of Rac- GTPase composite structure through its induced translocation in the plasma membrane[37].(Figure 2-2A)

Even though the initial cytosolic localization of the protein that will undergo the oligomerization process poses a risk for abnormal enzymatic activity. This unwanted effect can be dismissed with some modifications on CID strategy such as initial localizing of the protein into an inactive site[35]. Moreover, other studies have also shown that CID is suitable for target specific allosteric regulation of multiple number of proteins. Recently, Karginov et al. managed to perturb the enzymatic activities of a group of kinases through rapamycin based

on activation and deactivation by comprising rapamycin recognition domains to catalytic site of each kinase enzyme[38].

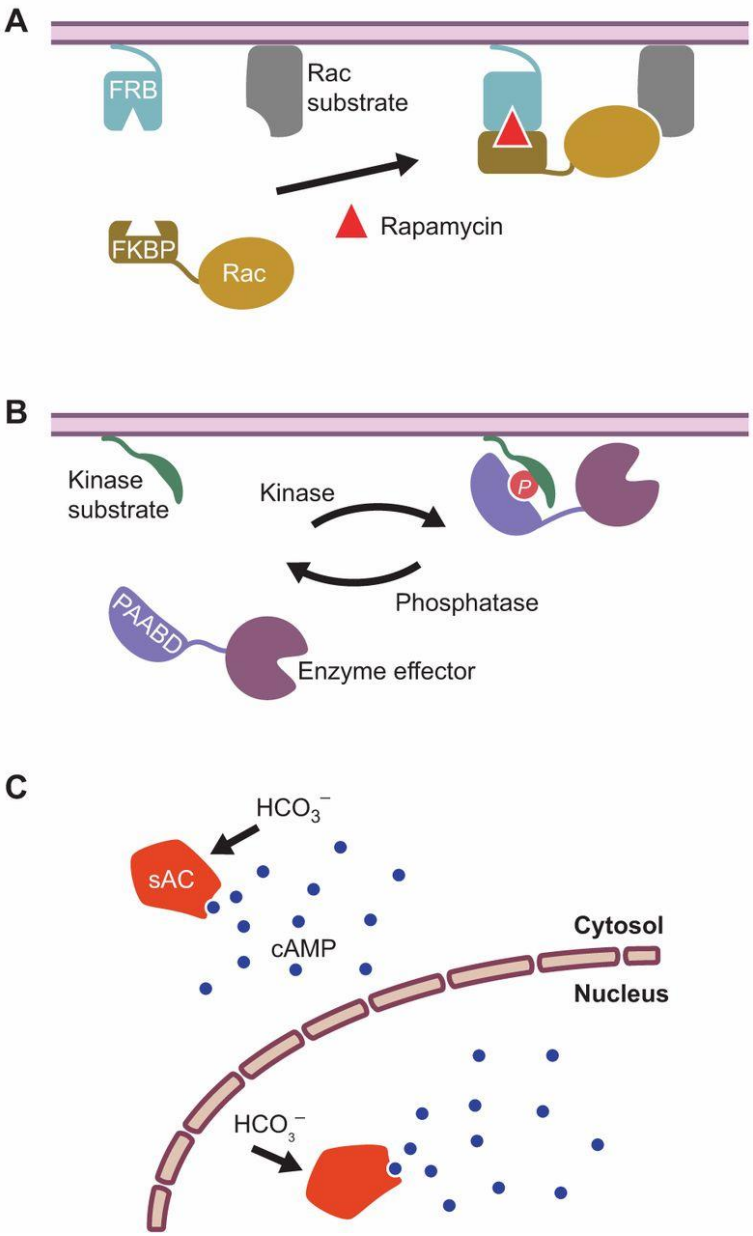

Figure 2-2 : Different types of genetically encoded chemically driven perturbation tools [7]

Furthermore, CID is more versatile and compatible for the control of multi-enzymatic events and signaling mechanisms compared to conventional chemically driven techniques

which are limited in simultaneous adaptability to several pathways. (Figure 2-2B) Recently, Sample et al. developed a technique for precise spatiotemporal control of cyclic adenosine monophosphate's (cAMP) enzymatic activity with soluble adenylyl cyclase (sAC) induced perturbation that is capable for duration, magnitude and localization manipulation. (Figure 2-2C) In this methodology, a truncated sAC is employed as on orthogonal agent to activate the generation of cAMP from ATP and for targeted localization in different subcellular compartments, whereas conventional techniques directly operate on cAMP concentrations causing widespread fluctuations of cAMP inside the cell.

Optically driven perturbation tools

Optically induced perturbations provide advanced target specific spatio-temporal resolution power in a non-invasive and, often, in an orthogonal way, even though it possess a limited reporter functionality in the monitoring case[39]. Since the optically driven techniques enables amelioration in both spatial and temporal resolution, it is possible to monitor and control impetuous signaling events specifically occurring either in subcellular sections or in a subgroup of cells. Therefore, many methods have been elaborated on to employ optical perturbation in signaling networks by means of natural or synthetic light sensitive proteins to govern protein-protein interactions, channel, and enzyme activities optically[40,41].

For instance, natural photoisomerization of chromophores can lead to prompt and bidirectional switch in some proteins' activation. The retinal in our bodies, is a common polyene chromophore that binds to opsin proteins responsible for visual transduction in the eye. Lately discovered channelrhodopsin-2 (ChR2)[42] and halorhodopsin (NpHR)[43], the new members of the bacterial opsin family, are natural optically-driven ion transport membrane proteins.(Figure 2-3A) When retinal absorbs a photon, its chromophore isomerizes and these

membrane proteins undergo a structural change to constitute a channel opening for ion transport and interaction with signaling transducer proteins[44,45]. Hence, these microbial rhodopsins are highly applicable for studying intracellular signaling in various biological events that involve an intensive exchange of ions or molecules through cellular the membrane such as muscle contraction, stem cell differentiation and, mostly neural signaling activities[46–49].

Another photoreactive structure, light-oxygen-voltage-sensing domain (LOV) is a sensory protein utilized by a big portion of living organisms including plants, bacteria, fungi and microalgae for sensing the changes in the outer environment. LOV domains of phototropins comprise a blue-light sensitive flavin mononucleotide (FMN) cofactor which initiates covalent bond formation between the chromophore and the reactive cysteine residue of the apo-protein[50]. This bonding initiates some changes in the conformation that result in the cleavage of C-terminal α-helix (Jα) which tightly associates to the domain structure in the dark. Previously, Wu et al. developed an impetuous and reversible light-driven tool through the fusion of GTPase-Rac1 biosensor to LOV- Jα photoactivatable protein[51]. (Figure 2-3B) In the dark, the Rac1 interaction domain was sterically blocked with the LOV domain through Jα helix hinging, whereas it was accessible to effector molecules after detangling of the helix linking achieved by blue-light irradiation. Later, other Rac1 focused light driven perturbation tools were developed for studying its function in cell migration of *Xenopus* and *Drosophila* model organisms[52,53].

Alternatively, light driven perturbation can be utilized for regulating protein-protein interactions that facilitate target specific displacement of proteins from one cellular complex to another[54]. For instance, plants possess phytochromes (Phy) as their photosensitive signaling proteins to coordinate their light-induced biological events. Phys are covalently bonded with

their phycocyanobilin (PCB) chromophores that can isomerize to give P_r (red absorbing) and P_{fr} (far-red absorbing) conformation upon light irradiation. When Phy is induced with red light, it explicitly binds to the phytochrome interaction factor (PIF) substrate to constitute Phy-PIF photoactivatable molecular switch structure. Levskaya et al. found that the photoswitchable property of Phy proteins are utilized for the activation of Rho-family GTPase through the translocation of effector substrate[55]. (Figure 2-3C) In this application, PhyB is attached to the plasma membrane, and directly binds to its effector substrate PIF after the photoisomerization of PCB upon red-light irradiation. This binding induces the translocation of PIF unit and the guanidine exchange factor (GEF) that is utilized for Rho-family GTPase activation, where PIF has been connected, from cytosol to plasma membrane.

Furthermore, fluorescent proteins can attain photoactivity functions by means of synthetic modifications and provide a light-driven enzymatic activity control. Dronpa, a quite similar version of GFP, is capable of reversible photoswitching upon light irradiation over many times.(Figure 2-3D) Its fluorescence is switched on and off with UV and blue light around 405 nm and 488 nm, respectively. The change in its fluorescence intensity is driven through the conformational state of the chromophore structure which is also present in GFPs. In fluorescence on mode, the chromophore is in cis formation, whereas it shifts to trans state in off mode. This engineered characteristic of Dronpa is utilized for light-driven activation of Cdc42 protein by inserting Dronpa to N- and C-termini of the Cdc42 GEF target domain[56]. Before light irradiation, Dronpa subgroups constitute a tetramer structure with a pair of composite proteins which prevent the interaction between Cdc42 GEF domain and Cdcd42 and forms a “caged” intersection. Upon blue-light excitation, Dronpa switches to the off mode causing disintegration of the Dronpa tetramer, release of intersectin part and successive activation of Cdc42 protein.

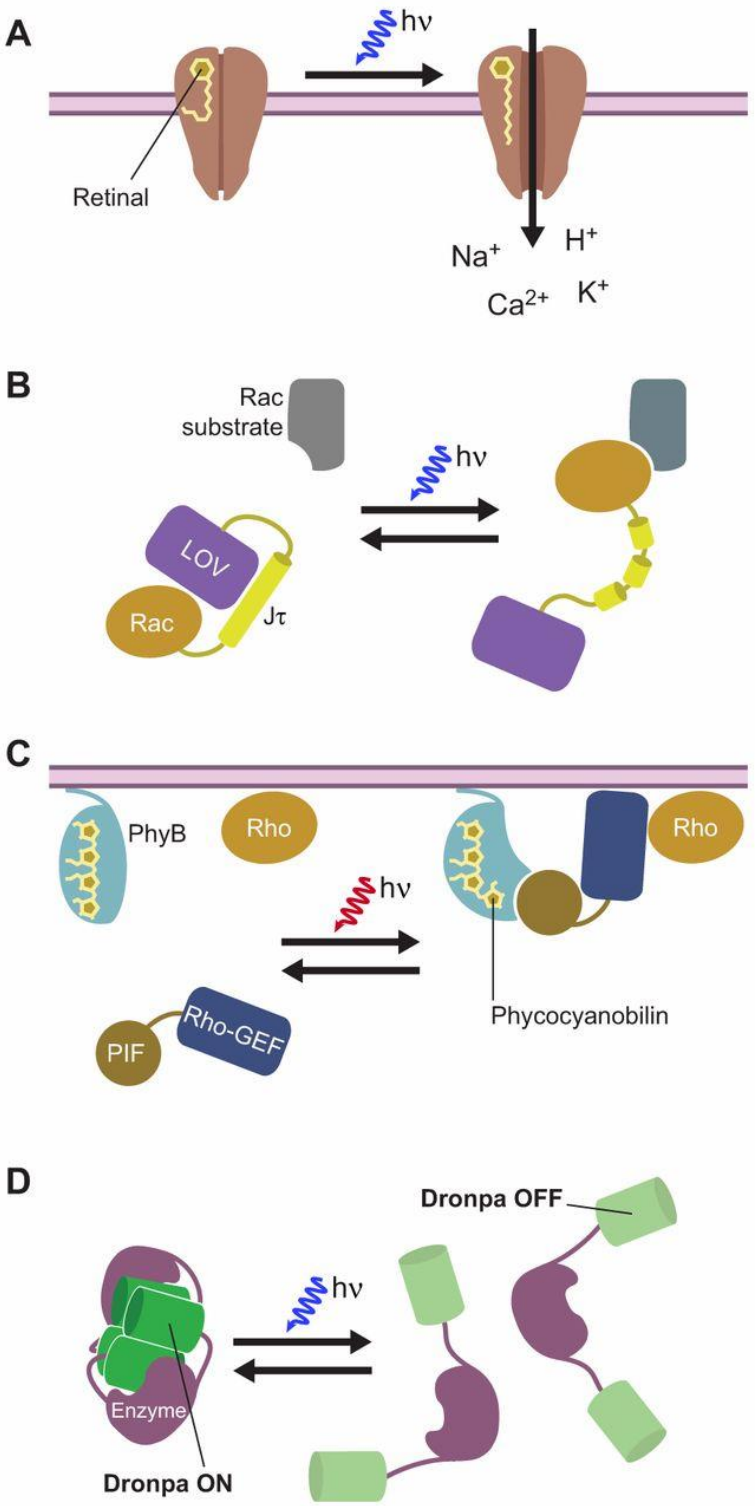

Figure 2-3 : Different types of genetically encoded optically driven perturbation tools[7]

Since genetically encoded tools provide dynamic monitoring and induced perturbation, it is possible to achieve a profound understanding in signaling networks and reveal the obscurities in signal integration and specific response generation through molecular mechanisms by employing combined genetically encoded molecular tools for visualization and stimulation of numerous biological events within living systems[57]. For instance, chemically driven targeted perturbation strategy is used for studying cell migration that is an intricate process involving numerous signaling and interaction throughout the movement[5]. In this study, they chemically perturb the activation of a membrane protein responsible for establishing spontaneous membrane protrusions and visualize its activity through labeled signaling molecules that are produced as a result of membrane protein's activity[58].

Similarly, some members of the rhodopsin protein family, a class of photoactivatable proteins, have become commonly used reporters for studying neural signaling network due to their light inducible ion transport channel constitution property. For instance, channelrhodopsins are utilized for visualizing the signal propagation through targeted synaptic connections by creating an action potential in a specific neuron upon light irradiation[59]. Moreover, their combination with genetically encoded Ca^{2+} indicators (GECIs), used for measuring neuronal activity through action potential or synaptic input endangered transitive Ca^{2+} flow, can reestablish the experimental methods for studying signaling networks in the neural system[40]. Even though the highly overlapping excitation spectra of photoactivatable channels (channelrhodopsin, halorhodopsin, etc.) and widely used GECIs (GCaMP, Cameleon etc.) can be problematic for simultaneous tracking and control of Ca^{2+} transients, new alternatives of spectrally shifted channelrhodopsins[60] and GECIs[61,62] are joined to genetically encoded tool kit under favor of some protein engineering modifications. In a recent study of Akerboom et al., they visualized and induced muscle contractions with

coexisting red-shifted GCaMP, RCaMP, and ChR2 (channelrhodopsin) in *C.elegans* model organism.

Consequently, precise and specialized analysis of numerous biological processes has become extremely important for comprehending the functioning in living systems. Therefore, genetically encoded tools promise an invaluable potential in advanced spatiotemporal visualization and perturbation of intracellular signaling within live biological systems. Furthermore, monitoring and perturbation combined genetically encoded tools are quite capable in target specific signal examination and dissecting the effective reasons for intermolecular relationship continuity. Ultimately, the advances in microcopy and molecular biology techniques gave rise to establishment of some commonly used genetically encoded tools that are mentioned in the above yielded many findings in signaling pathways, but still open for further improvements.

2.2. Importance of redox homeostasis in biological functionality

The living systems always strive for maintaining their inner balance which is open to alteration and impairment with external threats. In the 19th century, Claude Bernard remarked the significance of this delicate balance, *milieu intérieur*, for a sturdy continuity of the living system and this perpetual equilibrium is defined as homeostasis and believed to be oriented through redox signaling in today's biology. When a biological integrity faces with a threat, it directly responds to eliminate the challenge while avoiding any damage. Thus, oxidants, the signaling molecules of redox biogenesis, start to float around to induce responsive mechanisms with a rear up from their steady state rate of production-elimination cycle. The activation of redox signaling augments both pro-inflammatory cytokines and pro-oxidant

enzyme activities and they remain in this state until feedback mechanism returns the overall system from to “reactive” to steady state dynamics[63].

This tightly controlled balance is analogous to a philosophic ideology named as *aurea mediocritas*, the Golden Mean, believes that the maintained equality between our opposite behavior provoking motivations is the only way to adjust the life quality. Hence, the composure of this balance is not acquired just by leading in one favorable direction but also appeasing the opposite direction that would commutate the desired response. Therefore, the theory of the Golden Mean explains the way for obtaining a quality of life and how our inner equilibrium mechanism work for us to be heathy. Likewise, it is important to give a moderate response to threats that can perturb the balance and be aware that excess reaction can also lead a disturbance in the homeostasis as well.

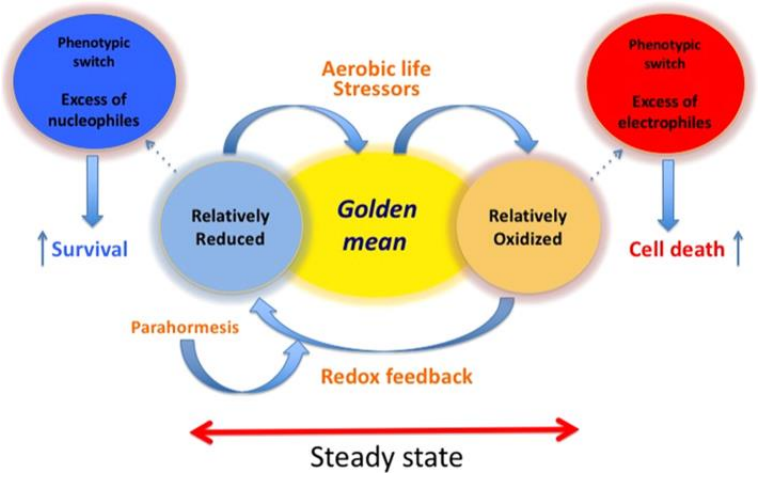

Figure 2-4 : The “Golden Mean” of redox homeostasis[63].

The stress concept in biology was first introduced by Hans Selye for defining abnormal physiological reactions to an input where cellular homeostasis is mostly found on the oxidative side of physiological steady state due to chemical, physical or biological challenges. Under these circumstances, biological integrity tries to eliminate the problem through feedback mechanism and restore the homeostasis back to its physiological steady

state. This effort of equalization may sometimes fail and lead to an abiding change in homeostasis, when feedback response is not sufficient to overcome the effect of the actuator. But it is not reasonable to consider the oxidants as stress facilitators due to their increased production rate that leads to induction of pro-inflammatory reactions under the presence of challenges, since these electrophiles also assist the upregulation of nucleophilic feedback response for steady state stabilization. Their presence can give rise to oxidative stress related problems such as inflammation and result in a permanent change of redox homeostasis, if the responsive feedback is not adequate to restore the steady state and physiological limits are violated.

Similarly, reactive oxygen species (ROS), the by-products of aerobic respiration and most common oxidants, are also contribute in cellular redox state determination by serving as "redox messengers" in intracellular signaling and regulation mechanisms at physiologically low levels[64]. But these reactive chemical oxygen species including hydrogen peroxide (H_2O_2), the hydroxyl radical (•OH), and superoxide (O_2^-) can induce various pathological conditions such as oxidative stress facilitated aging[65], neurological disorders[66], tumor progression in cancer[67], circadian clock related enzyme inhibition[68], and even cell death[64] at excessive levels.

Consequently, organisms are under the threat of direct or indirect confrontations caused by the detrimental consequences of aerobic life, xenobiotics, outside interactions that can perturb the redox equilibrium permanently. Thus, they increase the production rate of oxidative reactions and nucleophilic feedback response to prevent a stable shift in the redox homeostasis. However, oxidative stress may arouse if these innate immunity systems fail in maintaining the physiological redox state against challenges.

In the trite description, it is possible to estimate the redox state mathematically with Nernst equation through the redox potential of a specific redox couple. But this calculation

only provides a numeric value with the thermodynamic background of the reaction and ignores its biological condition that is essential for the real redox state. Therefore, a comprehensive redox state assessment is necessary by taking the concentration of relevant reagents and products, the rates of synthesis, degradation and regulation of all involved enzymatic reactions and transporters into account. Since redox biogenesis is a highly integrated and continuous mechanism, redox state of a molecule rely upon multiple concentrations and reaction kinetics rather than a simple ratio of its reduced and oxidized form concentrations.

2.2.1. Redox regulation in mitochondrial biogenesis

Since redox homeostasis concerns the tranquility of the whole biological integrity, it also takes part in the mitochondria, a vital player in cellular functionality by means of energy production and related mechanisms such as cell cycle sustain, programmed cell death, calcium signaling and various enzymatic pathways. Hence, the mitochondrial based events are actively regulated and protected from potential stress actuators through redox mechanism for maintaining its fundamental presence[69].

Mitochondria is one of the main hubs for ROS generation due to its continuous and massive ATP production through oxidative phosphorylation system (OXPHOS) to nurture the energy metabolism. The redox state of the biological system adjusts the mitochondrial amount needed for countervailing the energy demand and defines the role of redox signaling molecules like ROS in preserving the biological homeostasis[70]. Accordingly, the redox homeostasis of mitochondria during energy production is complementary for cell signaling networks and have a control over cell survival, migration, proliferation, and transformation. In a mitochondrial dysfunction, these redox regulators activates specific transcription factors

located in the nucleus and mitochondria responsible for the initiation of mitochondrial biogenesis[71]. Thus, they prevent the compensation of the cell metabolism through degradation of malfunctioning mitochondria by employing an oxidant-mediated protection process for controlling its functionality[72].

However, unsupervised accumulation of ROSs, respiratory chain by-products, because of mitochondrial abnormalities during ATP production can lead to a series of detrimental consequences[73]. The excess amount of these oxidants may build up oxidative stress and permanent alteration in the redox state by activating the immune effector enzymes driven inflammation, causing mitochondrial damage, inducing DNA mutation, and further production of oxidant species[74]. Therefore, the anomalous generation of ROSs, acting as redox signaling molecules, can prevent the stabilization efforts of the response mechanism, and ultimately cause a significant damage in biological homeostasis.

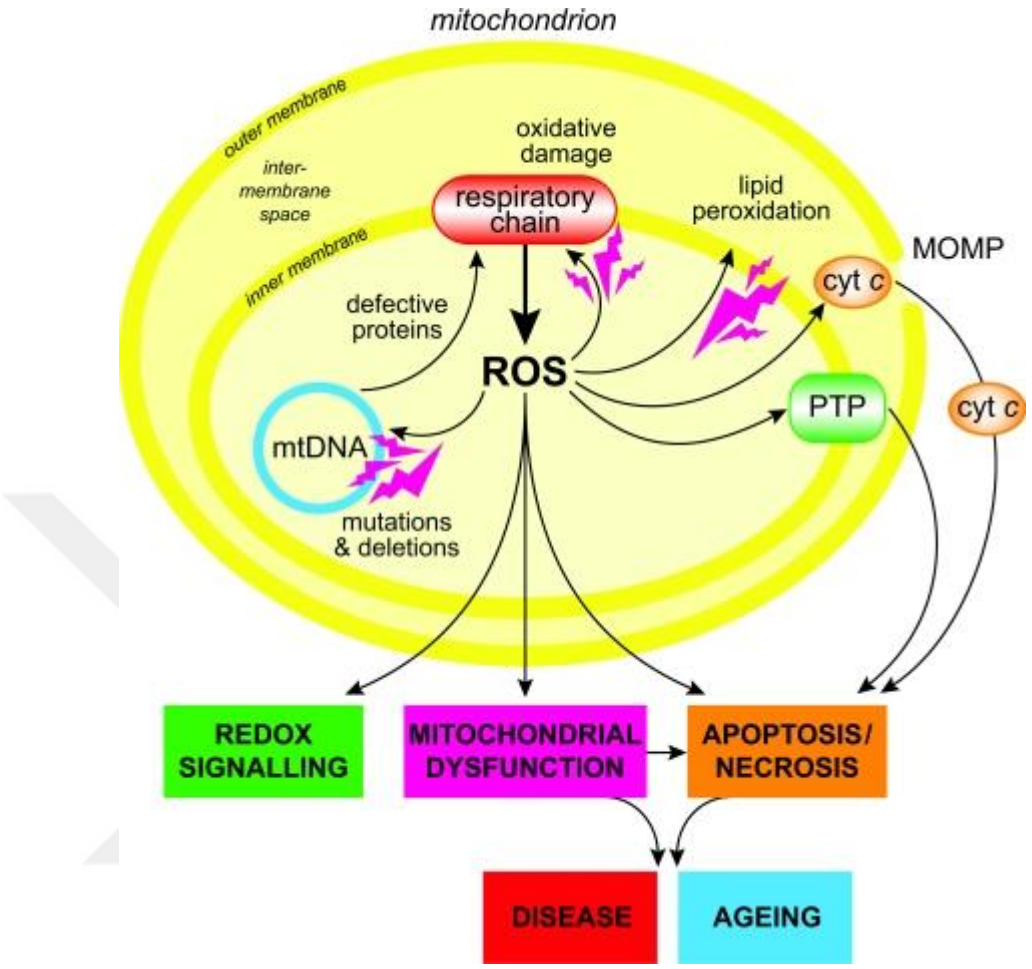

Figure 2-5 : Overview of mitochondrial ROS production[75].

Consequently, developing translational applications and tools for monitoring the flux of redox signaling molecules can give invaluable information in sources oxidative stress generation and redox signaling pathway alterations in biological organisms. Furthermore, it is pivotal to determine the characteristics, locations and kinetics of mitochondria centered ATP production related ROS within cellular and subcellular compartments by using genetically encoded probes and sensors capable of measuring ROS level and correlated redox state in living systems[76].

A comprehensive study of mitochondrial redox dynamics through ATP production involved enzymes, molecules and metabolites can give insight into multidimensional redox

signaling network across the biological metabolism for understanding their unrevealed role in oxidative stress promotion and physiological redox state preservation[77]. The utilization of redox sensitive, mitochondria specific, genetically encoded probes and sensors can provide high spatio-temporal monitoring of mitochondrial metabolism and, therefore, decipher the fine –tuned regulation of the redox players that are capable of generating versatile responses to maintain the redox homeostasis[78]. Moreover, their critical linkage and contribution in energy production sustainment through redox balance can unveil the undetermined mitochondria related consequences conducing toward oxidative stress, circadian clock dysregulation, neuronal circuity malfunction, cancer tumor regression and cell death. Ultimately, a better understanding of these double-edged sword like redox biogenesis components with genetically encoded tools can shed light on biological integrity's decision making process for protecting itself from any energy failure and its related detrimental consequences[79].

2.2.2. The key role Cytochrome c in mitochondria's redox mechanism

As mentioned above, mitochondria is the main fuel station of eukaryotic cells for its executive position in ATP production through OXPHOS and crucial for a sturdy cellular functioning[70]. Moreover, it is a semi-autonomous organelle and capable of inducing the synthesis of some respiratory chain involved proteins with its own genome[71]. The essential OXPHOS process is completed by means of mitochondrial electron transport chain (mETC) located in the inner membrane which links the matrix to intermembrane space (IMS) where ATP synthesis takes place.

Cytochrome *c* (Cyt *c*), a member of heme protein family, is a small protein found in the intermembrane of mitochondria and responsible for the electron transfer between

Complexes III and IV of mETC that is comprised of four multisubunit protein complexes (I – IV)[80]. Besides from its acknowledged electron carrying role in the respiratory pathway of ATP production, Cyt *c* also appears in protein import and the stabilization of respiratory chain complexes and supercomplexes of mitochondrial energy production process[81]. Furthermore, this small molecule like acting unique protein serves as a messenger between mitochondrial operation and cellular setting and, for this reason, it is capable of initiating the programmed cell death in biological dysregulation[82].

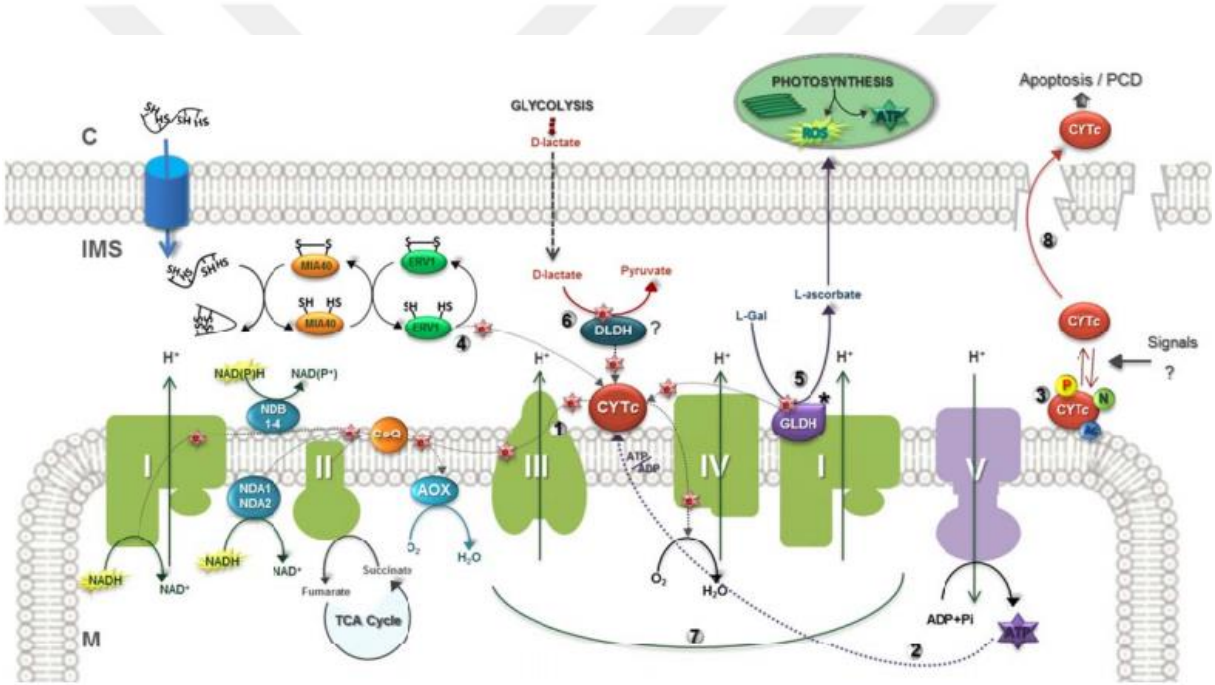

Figure 2-6 : Cyt *c* as a multifunctional respiratory pathway protein[83].

Two types of c-type cytochrome are found in the mitochondria, the redox sensitive heme protein Cyt *c* that is responsible for the electron transfer between Complex III (Cyt *c* reductase) and Complex IV (Cyt *c* oxidase, CcO) and, inner membrane located Cyt *c*1 that composes a complementary section of Complex III[84]. As for their structure, they possess heme prosthetic group that is covalently attached via two thioether bonds established between two reduced cysteines of the heme-binding motif (C_1XXC_2H) located in the preserved apo-

Cytochrome *c* (apo-Cyt *c*), and two vinyl groups of heme *b*[85]. The covalent binding of heme cofactor endows the stabilization of apo-Cyt *c* to prevent its prompt impairment[86]. The maturation of Cyt *c* structure is a complicated routine which requires the transfer of the synthesized apo-Cyt *c* and heme from cytoplasm or matrix to assembly destination IMS initially[87]. After their translocation to IMS, they are preserved in the reduced redox state until heme cofactor attachment.

After the succeeding biogenesis of Cyt *c*, it proceeds with its canonical function of electron transportation between Cytochrome bc_1 reductase and CcO through respiratory pathway that is located in the IMS of mitochondria[88]. Therewithal, the rate of this electron delivery from Cyt *c* to CcO is governed by ATP that acts as a feedback inhibitor agent for the interaction between two proteins due to high affinity ATP binding sites comprising of Cyt *c*[89].

This relatively small role of Cyt *c* acts as a rate-limiting step for the complete fulfillment of mETC in eukaryotic cells and preserves the continuity of aerobic energy production[90]. Thus, the absence or malfunctioning of Cyt *c* biogenesis may exert fatal consequences for the biological development such as abnormal or decelerated embryogenesis in mammalian organisms and promotes several human disease under restricted levels of Cyt *c* in signaling networks[91]. Its deficiency can also alter the phenotypic characteristics of plants displaying reduced biological mass due to slowed down growth rate caused by Cyt *c* scarcity driven reduction of energy production[92].

Consequently, Cyt *c* is an essential soluble heme protein found in the IMS of mitochondria and serves as an electron chaperone between Complexes III and IV primarily[93]. Apart from the indispensable presence of Cyt *c* for the aerobic respiratory chain, the irregularities during the maturation of its holoprotein form or knockout of its coding sequence can exert detrimental consequences in the developmental stage and its scarcity is also linked

to several human diseases. Similarly to its canonical electron shuttling in the respiratory chain, it fulfills the electron delivery duty in a mitochondrial pathway for the import of several IMS proteins[94]. Moreover, it works as an electron carrier for the synthesis of the ascorbic acid antioxidant and the oxidation D-lactate to pyruvate for preventing the catalysis of cytotoxic compound methylglyoxal. Likewise, Cyt *c* is responsible for the stabilization and/assembly of respiratory chain involved complexes and supercomplexes[95]. Lastly, its departure from mitochondria to cytosol enables the initiation of the programmed cell death cascade and determines the cell's fate[96].

The versatile nature of Cyt *c* attributes the check point title for its services in multiple redox reactions and nominates this exclusive protein as a promising candidate for modulating the whole respiratory pathway of a cell[93]. Therefore, Cyt *c* focused genetically encoded redox indicators (GERIs) can provide invaluable information on mitochondrial redox network through the analysis of integrated multiple pathways including Cyt *c* and the maintenance of cellular redox homeostasis.

Chapter 3 : DIRECT MONITORING OF CYTOCHROME *C* REDOX STATE USING PHOTOCHROMIC FRET

Redox activity of heme proteins such as c-type Cytochromes regulates many important cellular functions on energy metabolism and electron transfer[82]. The cellular stress and the reduced metabolic activity of the cell can vary the oxidative state of these proteins. Cytochrome *c* (Cyt *c*) is among the most-studied electron carrier protein and localize in the inter-membrane space of mitochondria[97]. Its main function is to transport charge between the Cytochrome *c* reductase and the Cytochrome *c* oxidase of the respiratory chain. Cyt *c* has also a crucial role for initiating apoptotic signaling[98]. If the folding of Cyt *c* and its redox activity are observed at spatiotemporal resolution, the heterogeneous events can be resolved by simultaneously collecting fluorescence signals from many cells[99]. In the cell models, programmed cell death was previously characterized by the release of Cyt *c* labeled with GFP or fluorescein derivative FlAsH[100–102]. Alternatively, dihydrorhodamine 123 and mitotracker-red are used indirectly as fluorescent probes to measure a single oxidation event[103,104].

Small molecule probes cannot be targeted to a specific population of cells and poorly localize due to its non-specificity in the mitochondria, nucleus or cell membrane that results in low signal-to-noise ratio. The dyes can aggregate; therefore cause phototoxicity or respiratory inhibition, which limits their long time use in neurons. Therefore, the direct and continuous measurement of Cyt *c*'s redox state still remains elusive. New molecular probes and methods

are needed to resolve multiple oxidation events reversibly in bulk samples and living systems[105,106].

One would like to attach a fluorescent protein not only to use it for localizing the protein but also for measuring Cyt *c*'s redox activity at a spatiotemporal resolution, therefore obtain cell's progress on energy and response to external stimuli. Since it is a highly dynamic protein and has significant role for initiating apoptosis and as an electron carrier[93], a new fluorescent method that fluorescently measure the redox state of Cyt *c* can provide invaluable information on electron transport process in neurons and cardiomyocytes[107].

Cyt *c* contains a heme (protoporphyrin IX) chromophore that is covalently linked by two thioether bonds to a Cys-X-X-Cys-His (X=amino acid) motif of protein via vinly groups on the heme[108,109]. The Cyt *c* Heme Lyase catalyzes the binding of heme residing in a small cavity where a small molecule can bind to the heme[110]. The redox reaction of Cyt *c* results in an absorption change that indicates the oxidation state of the Cyt *c*. It has a large soret peak at 408 nm that shifts significantly to 415 nm at the reduced Cyt *c*. It has also distinguished α and β peaks at 520 and 550 nm respectively. The absorption intensity at these wavelengths increases as the Cyt *c* heme reduces from ferric to ferrous state[111].

Many different spectroscopic methods were previously used to study these spectral changes in bulk samples[112–114]. Direct absorption measurements of a Cyt *c* requires high protein concentration and it is not possible to distinguish the redox state of the Cyt *c* in cells by conventional imaging methods. Fluorescence readout could be a more sensitive method to measure Cyt *c*'s redox state directly. Similarly, phosphorylation reactions, kinase activity and membrane potential have been measured fluorescently using genetically engineered fluorescent reporters[30,49,115].

However, the fluorescence of the Cyt *c* is very dim due to the non-fluorescent endogenous cofactor therefore it is not possible to detect signal changes in cells. In recent studies, Alexa-660 labeled Cyt *c* was used to measure the heme dynamics[116]. Alternatively, genetically encoded fluorescence probes would be used to monitor Cyt *c*'s redox events at the spatiotemporal resolution. A key challenge is to overlay the Cyt *c* oxidation state by the fluorescent intensity change of the reporter protein. Here we demonstrate that photochromic fluorescence energy transfer (pcFRET) can be used to measure the changes in redox state of Cyt *c* reversibly. pcFRET is an important tool for studying the dynamics of macromolecules[117,118]. We recently used pcFRET to resolve the protein dynamics of microbial rhodopsins and clearly resolved the intermediate states of the photocycle by using the fluorescent dye labeled rhodopsin[119].

FRET is generally used as a fluorescence method to determine the distance change between the donor and acceptor fluorophore[120]. In pcFRET, the fluorescent probe is used to measure spectral overlap of fluorescent donor with non-fluorescent acceptor therefore can be used as spectroscopic ruler. The magnitude of quenching by the acceptor strongly depends on the spectral separation between the emission of the donor and the absorption of the acceptor. Even though the distance between donor and acceptor remains unchanged, the spectral separation can be measured fluorescently.

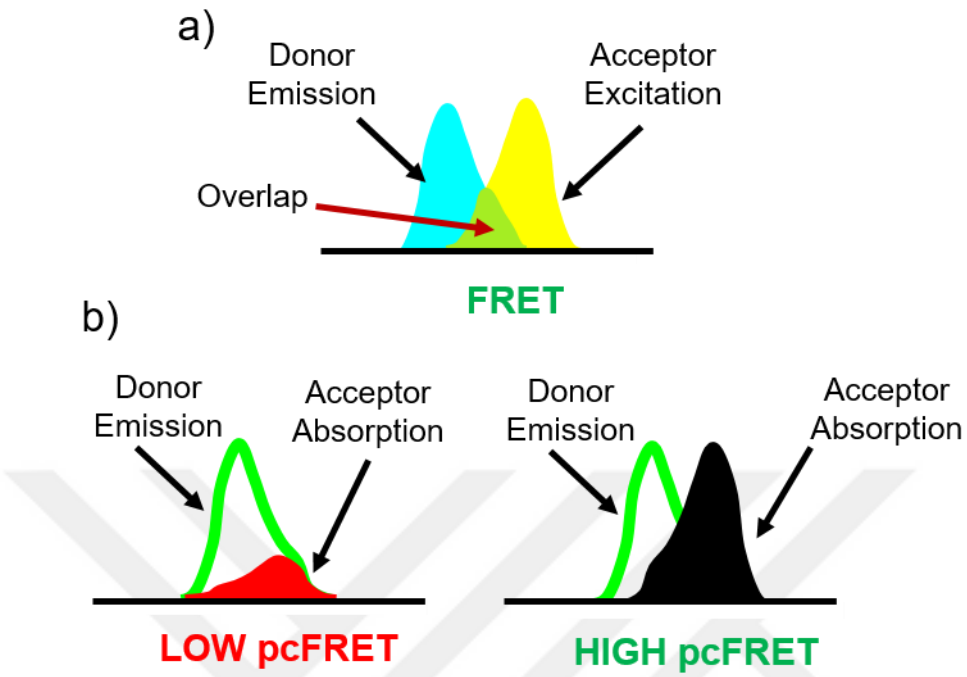

Figure 3-1 : The significance of the spectral overlap between the donor and acceptor for FRET and pcFRET signal. a) The spectral overlap between the donor emission and acceptor excitation is fixed mandatory for receiving a FRET signal. b) The degree of absorption change in the acceptor that overlaps with the donor emission defines the pcFRET magnitude and enables the modulation of the spectral overlap.

Cyt *c* can be conjugated to a fluorescence protein and thereby quench its fluorescence selectively at a specific region of the emission spectrum. The magnitude of the FRET signal gets stronger as the degree of overlap between the emission of donor and the absorption of the acceptor increases. The redox reaction of Cyt *c* does not alter the conformation significantly that was studied by electron spin resonance and visible spectroscopy. The absorption wavelength at 530 and 550 nm for the reduced state of Cyt *c* increases four folds after addition of reducing agent such as dithiothretiol (DTT).

We demonstrated that enhanced Venus fluorescence protein can be used as a donor to measure the redox activity of Cyt *c*[121]. The broad emission peak (max. at 530 nm) of Venus overlaps with the absorption of both α and β bands that would be selectively reduce the emission where the magnitude of change is higher. The C-terminus of Cyt *c* was tagged with Venus as a reporter. The Cyt *c*-Venus fusion protein (Cyt *c*-Venus) is characterized and the redox activity of Cyt *c* with redox reagents was measured by the ratiometric fluorescence emission of Venus. Multiple events of redox state of the Cyt *c* in bulk samples was demonstrated and revealed the redox state of Cyt *c* can be monitored by pcFRET. We also observed that the brightness of Cyt *c*-Venus expressing BL21 cells was less than the cells only expressed apoCyt *c*-Venus indicating that broad heme absorption around 530-560 nm quenches the fluorescence emission of the Venus.

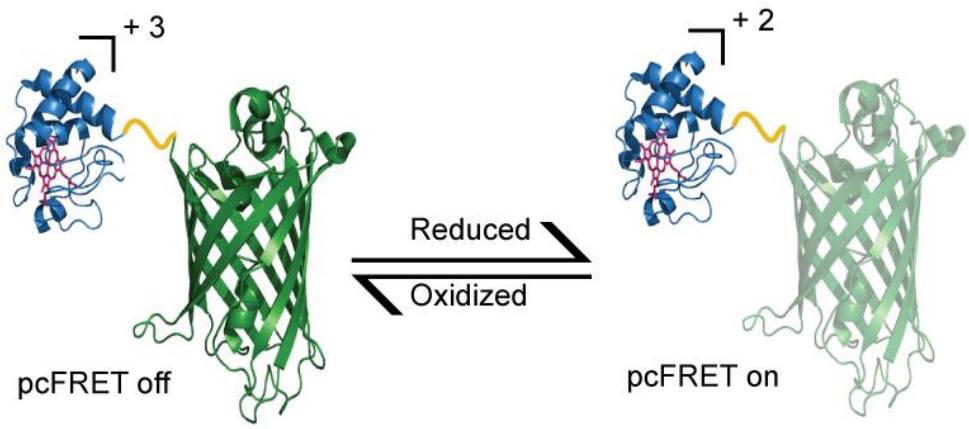

Figure 3-2 : The working principle of pcFRET method used for monitoring the redox state of Cyt *c* protein. Absorption spectrum of Cyt *c* alters depending on its oxidation state. When it is in the reduced form, the remarkable increase in the absorption peak around 550 nm causes efficient quenching in donor protein Venus' emission due to spectral overlap between donor's emission and acceptor's absorption. In the figure, possible 3D crystal structure of Cyt *c*-

Venus fusion protein is depicted where Cyt *c* (blue protein cartoon) is linked to Venus (green protein cartoon) via three adenine comprising linker (yellow lacer)[121].

3.1. Sample Preparation

3.1.1. Reagents

Potassium ferrocyanide, potassium ferricyanide, N,N,N',N'-tetramethyl-1,4-benzenediamine (TMPD) were obtained from Sigma-Aldrich (St. Louis, MO). Dithiothreitol (DTT), sodiumhydrosulfide, sodiumazide were obtained from VWR (West Chester, PA). CM sephadex C-50 was purchased from Sigma-Aldrich (St. Louis, MO). Chemicals were used as received without any further purification. BL21 (DE3) *E.coli* cells were purchased from Invitrogen (Carlsbad, CA).

3.1.2. Recombinant DNA construct design and protocol

The pBTR-1 (Amp_r) plasmid containing the iso-Cyt *c* gene and the yeast Cyt *c* heme lyase gene was kindly provided by Bruce E. Bowler of the University of Montana, Missoula, and Montana. It was used as a scaffold to construct Cyt *c*-Venus and apoCyt *c*-Venus fusion. The plasmid encoding Venus was kindly provided by Adam E. Cohen of Harvard University, Cambridge, and Massachusetts.

After PCR amplification of plasmids using the forward and reverse primers (Table 1), two non-existing restriction sites (NotI-HF and BamHI-HF) were introduced to backbone. For the expression of Cyt *c*-Venus construct, Venus gene is attached to C-terminus of the Cyt *c* plasmid through the corresponding restriction sites of digested pBTR-1 via standard subcloning method. Cyt *c* heme lyase that catalyze the heme insertion was coexpressed at the same vector. To prepare a template for apoCyt *c*-Venus, fragment encoding Cyt *c* heme lyase was removed and religated after blunt-filling recessed 3' of the Cyt *c*-Venus (Figure 3-3). The

sequence of each plasmid was verified at the sequencing center of Macrogen Inc (Amsterdam, The Netherlands) (Table 2).

Table 1 : The sequence of the primers used for the cloning of Venus region into pBTR-1 encoding Cyt *c* and Cyt *c* Heme Lyase.

Primer Sequence	Description
5’ – AAA AGC GGC CGC ACAGGC CCC TTT TCC T – 3’	Forward primer for Cyt *c* amplification
5’ – TTT TGC GGC CGC CTC ACT GGC TTT TTT CAA GTA GGT – 3’	Reverse primer for Cyt *c* amplification
5’ – AAA AGC GGC CGC AAT GGT GAG CAA GGG CGA G – 3’	Forward primer for Venus amplification
5’ – CCC CGG ATC CTC ACT TGT ACA GCT CGT CCA TGC CGA – 3’	Reverse primer for Venus amplification

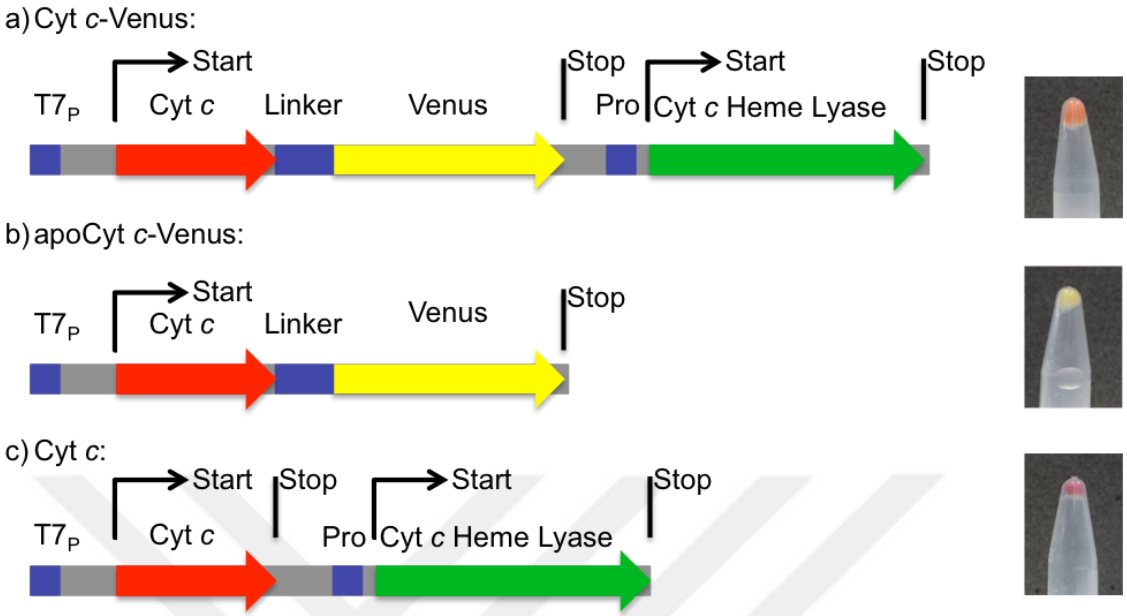

Figure 3-3: Schematic representation of the recombinant DNA constructs and the corresponding proteins expressed in *E. Coli* using these plasmids. a) Cyt *c*-Venus plasmid construct. b) ApoCyt *c*-Venus plasmid construct. Cyt *c* Heme Lyase was removed from the plasmid. c) Cyt *c* encoding plasmid construct.

Table 2 : Nucleotide sequence of Cyt *c*-Venus encoding region. The sequence of the plasmid was verified at the sequencing center of Macrogen Inc. (Amsterdam, The Netherlands). (Red : Cyt c, Blue : NotI Restriction Site, Green : Venus)

ATGACTGAATTCAAGGCCGGTTCTGCTAAGAAAGGTGCTACACTTTTCAAGACTAGATGT
CTACAATGCCACACCGTGGAAAAGGGTGGCCCACATAAGGTTGGTCCAAACTTGCATGGT
ATCTTTGGCAGACACTCTGGTCAAGCTGAAGGGTATTCGTACACAGATGCCAATATCAAG
AAAAACGTGTTGTGGGACGAAAATAACATGTCAGAGTACTTGACTAACCCAGCCAAATAT
ATTCCTGGTACCAAGATGGCCTTTGGTGGGTTGAAGAAGGAAAAAGACAGAAACGACTTA
ATTACCTACTTGAAAAAAGCCAGTGAGGCGGCCGCAATGGTGAGCAAGGGCGAGGAGCTG
TTCACCGGGGTGGTGCCCATCCTGGTCGAGCTGGACGGCGACGTAAACGGCCACAAGTTC
AGCGTGTCCGGCGAGGGCGAGGGCGATGCCACCTACGGCAAGCTGACCCTGAAGCTGATC
TGCACCACCGGCAAGCTGCCCGTGCCCTGGCCCACCCTCGTGACCACCCTGGGCTACGGC
CTGCAGTGCTTCGCCCGCTACCCCGACCACATGAAGCAGCACGACTTCTTCAAGTCCGCC

3.1.3. Expression and purification

The Cyt *c*-Venus, apoCyt *c*-Venus and Cyt *c* were expressed separately in *E. coli* BL21 (DE3) and purified according to previous methods (Figure 3-4). The expression level of each construct is similar to that of the unlabeled Cyt *c* as indicated by 10 % SDS page stained with Coomassie blue. Briefly, for expression of proteins, a 5 ml overnight culture in Luria-Bertani (LB) broth was grown at 37 ^{o}C. Then 100 μl were transferred into 100 ml LB broth medium containing heme and 50 μg ml^{-1} ampicillin. Cells were grown at an overnight culture and harvested by centrifugation. After resuspension in lysed solution, they were sonicated for 5 minutes (30 sec. on-10 sec. off) and centrifuged at 18.000 rpm for 20 minutes. The supernatant was collected and concentrated using 30 kDa centrifugal filter (Millipore) to remove impurities. It was washed with 20 mM phosphate buffer at pH 8.0 before loading into CM column. The sample were purified by using CM cation exchange column. Briefly, 1.0 gr. of CM was added to phosphate buffer to prepare slurry solution and poor into 10x1 cm flex column (Thomas scientific). Then, the sample was loaded into the column and washed several times with the phosphate buffer. An orange color solution was retained the column.

The Cyt *c*-Venus was eluted by varying the ionic strength from 50 mM to 500 mM NaCl in the phosphate buffer and collected in small tubes. The purified samples were characterized by SDS gel electrophoresis. We observed a single broad band that was an indication of Cyt *c*-Venus which was purified at high concentration. From the absorption spectrum, the Cyt *c*-Venus oxidation state was determined at the reduced form. The oxidized Cyt *c* -Venus was prepared by adding 500 μM of $[Fe(CN)_6]^{+3}$. Then excess $[Fe(CN)_6]^{+3}$ was removed by using centrifugal 30 kDa cutoff filter.

All samples were prepared in 50 mM phosphate buffer at pH 7.0 which is obtained by mixing 50 mM sodium dibasic and sodium monobasic solution in a 1.6:1 ratio unless

otherwise specified. The concentration of Venus, reduced-Cyt *c* and oxidized Cyt *c* were determined by their extinction coefficients ($\varepsilon_{\text{Cyt } c}(Fe^{+3})$ = 9.8 mM^{-1} at 550nm; $\varepsilon_{\text{Cyt } c}(Fe^{+2})$= 29.4 mM^{-1} at 550nm; $\varepsilon_{\text{Venus}}$ = 92.2 mM^{-1} at 518nm).

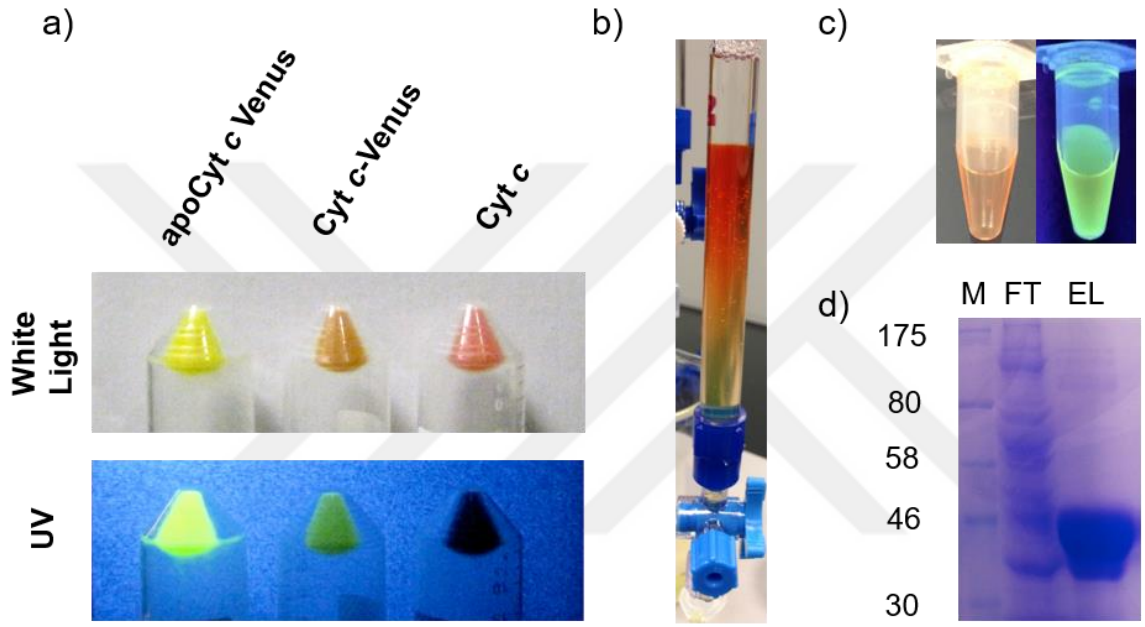

Figure 3-4 : Expression of constructs in *E. Coli* and purification of Cyt *c*-Venus. a) Pelleted *E. coli* expressing apoCyt *c*-Venus, Cyt *c*-Venus and Cyt *c* proteins b) The cell lysate was loaded on the CM sephadex column. After washing several times, orange color Cyt *c*-Venus binding to CM at low ionic strength was observed. c) Eluted Cyt *c*-Venus under white light (left) and UV illumination (right). d) The purification and expression of Cyt *c*-Venus was verified by SDS gel electrophoresis. Both the flow through and elution fractions were loaded on a SDS gel. A distinct band around 40-42 kDA (Cyt *c* : 12-15 kDa, Venus 27 kDa) can be seen in the third lane. (FL, flow through fraction, EL, elution fraction, M, Marker (kDa)).

3.2. Characterization

3.2.1. Spectroscopic characterization

The fusion proteins were washed twice with phosphate buffer, concentrated with a centrifugal filter and transferred to small measurement cuvettes with 10 μM concentration. The absorption spectrum of proteins was measured at 25 ºC by UV-3600 UV-Vis-NR spectrophotometer (Shimadzu Instruments). The fluorescence of each sample was measured separately at 25 ºC by FluoroMax-3 spectrophotometer with 1 nm/min scan.

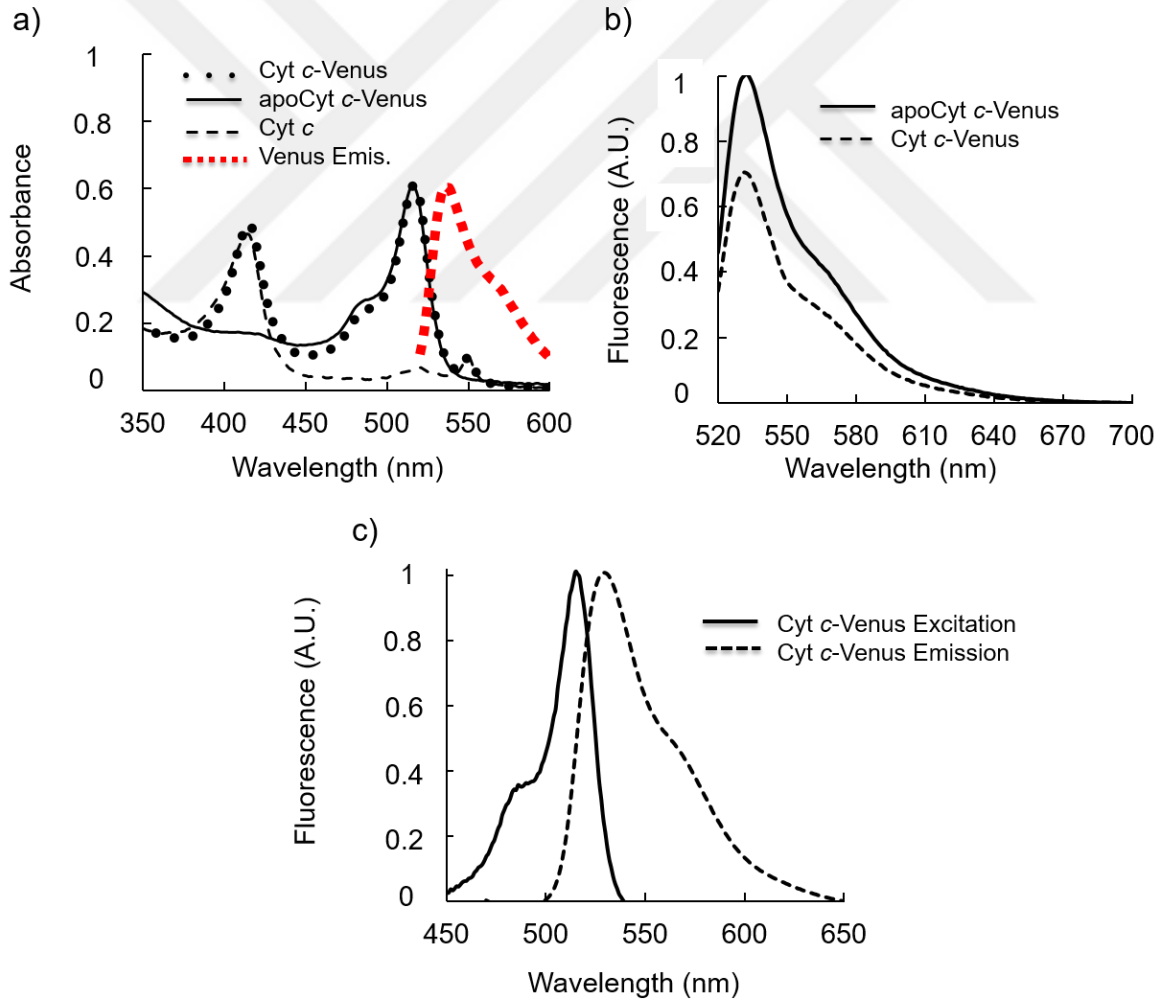

Figure 3-5 : Spectroscopic characterization of recombinant DNA constructs. a) Absorption spectra of Cyt *c*-Venus, apoCyt *c*-Venus, Cyt *c* proteins expressed in BL21 *E.Coli* cells. b)

Normalized fluorescence emission of Cyt *c*-Venus (solid line) and apoCyt *c*-Venus (dashed line) in BL21(DE)3 cells. The fluorescence intensity from Cyt *c*-Venus was reduced due to the energy transfer from Venus to Cyt *c*. c) Fluorescence excitation and emission spectra of Cyt *c*-Venus in 50 mM phosphate buffer at pH 7.0. The emission maximum was identical to the free Venus protein used as a control sample. An excitation spectrum was collected at an emission of 530 nm. An emission spectrum was collected at 488 nm excitation.

3.2.2. Fluorescence lifetime measurements

ApoCyt *c*-Venus and Cyt *c*-Venus at different oxidation states were prepared and characterized before the measurement. 100 µl of sample was dropped on to the coverslip. Nikon TE 2000 inverted fluorescence microscope with a 60X oil immersion objective, numerical aperture 1.49 were used for lifetime measurements using time-correlated single photon counting (TCSPC). A pulsed 488 nm laser beam obtained by frequency-doubling the 976 nm output of an ultrafast Ti:Sa laser (pulse width 140 fs, repetition rate 80 MHz - Chameleon Ultra II; Coherent) was sent to a single photon counting module (SPCM) serving as the start detector.

Fluorescence was collected using the same microscope objective, transmitted through the dichroic mirror FEL500 (Thorlabs) and emission filter HQ530/50 (Chroma) and detected by another SPCM serving as the stop detector. A time to amplitude converter (TAC) and a multipurpose data acquisition card serving as a multi-channel analyzer (MCA) were used to generate the histogram of coincidence detection events as a function of the delay time between start and stop pulses. The data was recorded using custom data acquisition software and analyzed with MATLAB (R2011a, The MathWorks, Natick, Massachusetts).

Fluorescence lifetime was calculated by using a single exponential curve fitting. The least-squares method was used in obtaining the fit parameters.

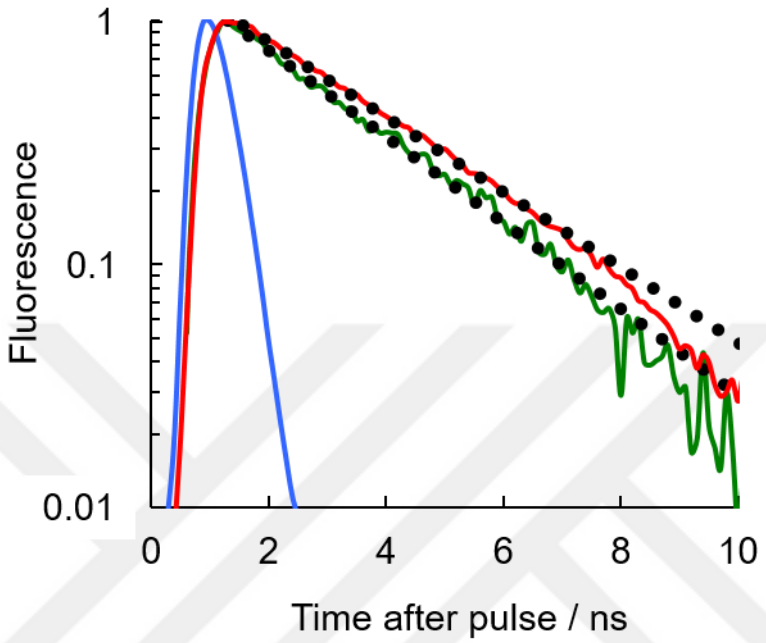

Figure 3-6 : Fluorescence life times of oxidized and reduced Cyt *c*-Venus. The oxidized Cyt *c*-Venus has 2.81 ns life time whereas the reduced one has 2.45 ns due to quenching in Venus's emission caused by the reduction of Cyt *c*. Fluorescence lifetime of Cyt c–Venus at the reduced (green) state, at the oxidized state (red) and internal response of the laser (blue) at the log scale. The lifetime was predicted by fitting the data to a single exponential decay function (circle).

3.2.3. Epifluorescence microscopy

Two holes were drilled on a glass microscope slide by Dremel 4000 equipped with diamond bits. Silica cover slips and slides were cleaned in piranha solution (a highly corrosive 3:1 mixture of concentrated H_2SO_4 and 30% aqueous H_2O_2) and assembled into a flow-cell using a 0.3 cm thick spacer (McMaster-Carr Corp., Princeton, NJ). The flow cell was filled with polylysine (Sigma Aldrich Co. LLC., St Louis, MO) and stand for 10 minutes.

After washing three times with buffer, the 30 µl sample is loaded to the flow cell. Then it was washed two times to remove unbounded *E. coli*.

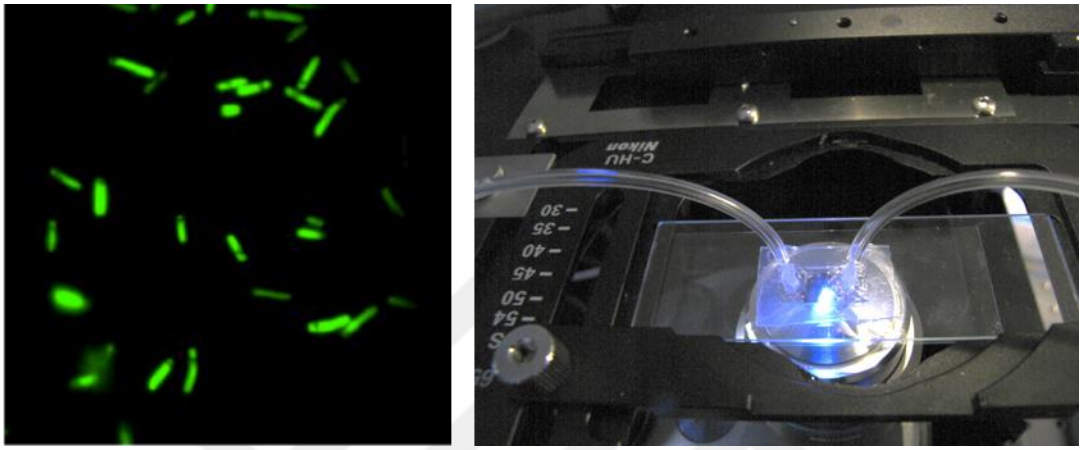

Figure 3-7 : Flow cell setup for epifluorescence microscopy experiments.

The samples were excited by a diode pumped solid-state 473 nm laser (DragonLaser), which is controlled with a custom software (Arduino v1.0.5) and microcontroller board (ATmega328, Arduino Uno, Italy). Nikon eclipse inverted fluorescence microscope with a 60X oil immersion objective, numerical aperture 1.40 were used for epifluorescence measurement. The fluorescence images of Cyt *c*-Venus and apoCyt *c*-Venus expressing cells were recorded by an Andor Luca S EMCCD. Images were analyzed with MATLAB and ImageJ (1.6.0v, Bethesda, Maryland). All experiments were performed at room temperature.

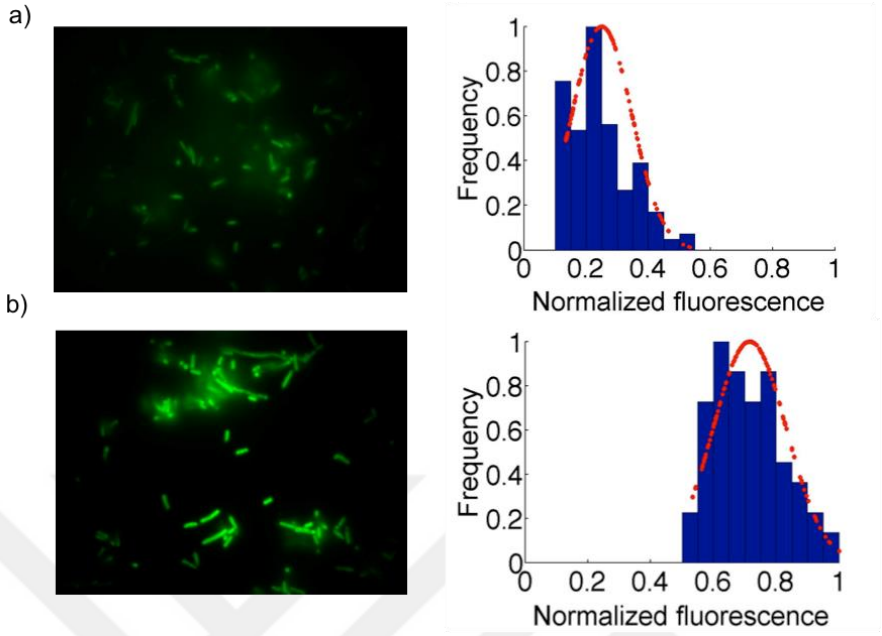

Figure 3-8 : The quantification of protein expression in BL21(DE3) cells. a) Cyt *c*-Venus expression. b) ApoCyt *c*-Venus expression. The images of the cells were analyzed with MATLAB (The MathWorks, Natick, MA).

The histogram (Cyt *c*-Venus, top and Apo Cyt *c*-Venus, bottom) represents the distribution of Venus fluorescence in the cells. The fluorescence intensities were normalized by using the maximum fluorescence from apoCyt *c*-Venus cells. Briefly, the fluorescence intensity of each pixel above a threshold was determined from images. Then, the values were counted to calculate the fluorescence distribution. All data was normalized before plotting. From a Gaussian fit (red dotted line), the average intensity and errors of Cyt *c*-Venus and apoCyt *c*-Venus were calculated as 0.25±0.09 and 0.71±0.11 respectively.

3.2.4. Förster radius (R_0) of Cyt c-Venus

The overlap integral of Cyt *c*-Venus was calculated using[122]:

$$J(\lambda) = \int_{\lambda_i}^{\lambda_f} F_v(\lambda)\varepsilon_{Cy}(\lambda)\lambda^4 d\lambda \qquad \text{(Eq. 1)}$$

Where F_v is the normalized Venus emission spectrum, $\varepsilon_{Cyt\,c}$ is the Cyt *c* molar extinction coefficient. In the spectrum, a region from 520 nm to 600 nm was selected to calculate the overlap integral. We consider $\varepsilon_{Cyt\,c}(Fe^{+2})$ = 29400 M^{-1} cm^{-1} at 550 nm as the reference to calculate molar extinction coefficients at all wavelengths. $J(\lambda)$ was calculated as $1.12x10^{-13}$ $M^{-1}cm^3$.

The Forster radius of Cyt *c*-Venus was calculated using[122]:

$$R_0 = [8.8x10^{-25}\kappa^2\Phi_D n^{-4} J(\lambda)]^{1/6} \qquad \text{(Eq. 2)}$$

where Φ_D is the fluorescent quantum yield of the Venus, κ is an orientation factor, n is the refractive index of the buffer, and J(λ) is the overlap integral. n and Φ_D were taken as 1.33 and 0.57[123] respectively. Since we used a flexible linker, Venus chromophore and the heme had a rapid and unrestricted rotation, so transition dipole of Cyt *c*-Venus can be regarded as isotropically degenerate that yields a value of 0.66 for the orientation factor. Moreover, Cyt *c* had a negligible structural change at different oxidation states[124]. It includes small coordination change of axial ligand but no effect on heme position in the Cyt *c*[125]. By considering all factors, the Förster radius (R_0) was determined as 4.9 nm.

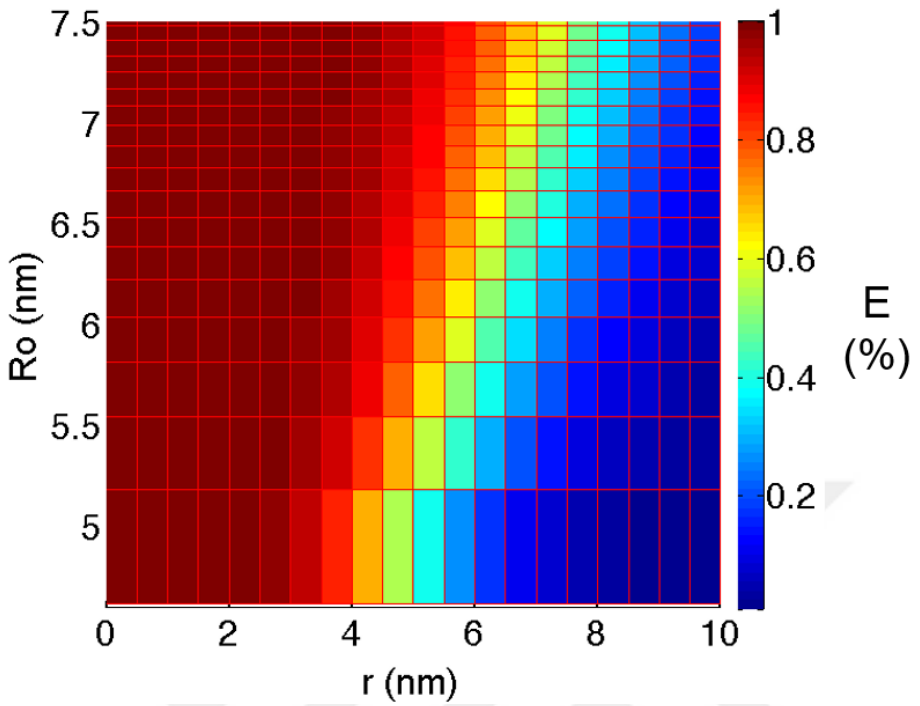

Figure 3-9 : The pcFRET efficiency color map is generated by means of simulations with variable R_o (nm) and r (nm).

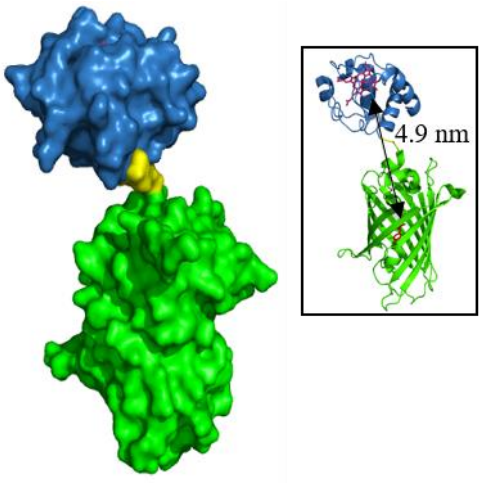

Figure 3-10 : The surface map of Cyt *c*-Venus complex. The crystal structures of Cyt *c* (blue, PDB ID-3CYT) and Venus (green, PDB ID-3V3D) were downloaded from Protein Data Bank. A linker composed of three alanine residues (yellow) was added to the N terminus of the Venus. To avoid any the steric effect that may arise from Cyt *c* and Venus crowding, the

surface map of the complex was calculated by using PyMol (Schrödinger LLC.) software. Energy minimization was also performed by using Swiss PDB-viewer. Identical surface maps were obtained. Then, C terminus of Cyt *c* was virtually combined to the N terminus of the Venus. The average measure from Cyt *c* heme center to Venus chromophore was 4.9 nm. (Inset, cartoon structure of the Cyt *c*-Venus complex, the heme and Venus chromophore were shown in red.)

3.2.5. Förster radius (R_0) from lifetime measurements

$$\frac{1}{\tau_{re}} = \frac{1}{\tau_{ox}} + \mathrm{k_{pcFRET}} \qquad \text{(Eq. 3)}$$

Where $\mathrm{k_{pcFRET}}$ is the rate constant of nonradiative energy transfer due to pcFRET. τ_{ox} and τ_{re} represents the fluorescence lifetime of the oxidized and reduced Cyt *c*-Venus respectively.

$$E = \frac{1}{1 + \left(\frac{r}{R_0}\right)^6} = 1 - \frac{\tau_{re}}{\tau_{ox}} \qquad \text{(Eq. 4)}$$

E is energy transfer from Venus to Cyt *c*. r and R_0 represent the distance from the Cyt *c* heme to Venus chromophore and Förster radius respectively. The Cyt *c*-Venus separation was calculated as 6.6 nm by using the τ_{ox} and τ_{re} that were measured from fluorescence lifetime measurements. All data were analyzed with MATLAB.

3.3. Results and Discussion

3.3.1. The redox activity of Cyt c by pcFRET

The fusion proteins was washed twice with phosphate buffer and concentrated with a centrifugal filter. For pcFRET measurements, the purified Cyt *c*–Venus, apoCyt *c*–Venus and Cyt *c* were prepared in 50 mM phosphate at pH 7.0 with 10μM protein concentration and transferred to small plastic cuvettes. The absorption spectrum of proteins was measured at 25 ^{o}C by UV-3600 UV-Vis-NR spectrophotometer (Shimadzu Instruments). The fluorescence of each sample was measured separately at 25 ^{o}C by FluoroMax-3 spectrophotometer. The same procedure was repeated for titrating samples with redox reagents. DTT, sodiumhydrosulfide, ferrocyanide, sodium azide and TMPD were used as a reducing agent. Ferricyanide was the only oxidizing agent in pcFRET experiments. All redox reagents were prepared at 500 mM in a small vial. apoCyt *c*-Venus and Cyt *c* were used as a control sample in all experiments.

The visible absorption profiles of the samples were recorded using a UV-Vis spectrophotometer (Figure 3-12a). Three sharp peaks for Cyt *c*–Venus were clearly resolved in the visible region. Cyt *c*–Venus has a 414 nm Soret band and a β-band at 550 nm indicating that Cyt *c* was isolated in the ferrous state. These absorption peaks of Cyt *c*–Venus were at identical positions to the Cyt *c* control sample that was expressed without Venus. We concluded that Venus attachment neither changed the coordination of heme nor affected the Cyt *c* folding.

The intense peak at 514 nm was an indication of Venus absorption. A small a-band of the Cyt *c* at 520 nm was unresolved due to significant spectral overlap of the Venus while the β-band was unaffected due to the reduced absorption of Venus at around 550 nm. A single

peak at 514 nm was observed for apoCyt *c*–Venus. By using the emission spectrum of Venus and Cyt *c* absorption, the Förster radius (R_0) of Cyt *c*–Venus was estimated to be 4.8 nm (Eqn. 2). It was close to our initial estimation of 4.9 nm obtained by virtual docking in PyMol software.

To perform the pcFRET, the reaction of Cyt *c*–Venus with DTT was recorded using a fluorometer. The Cyt *c*–Venus was prepared at the oxidized state and its emission spectrum was recorded. The oxidized Cyt *c*–Venus has a broad peak with a maximum at 537 nm that was indistinguishable from apoCyt *c*–Venus (Figure 3-12b). Then, 10 μM of Cyt *c*–Venus in the cuvette was mixed with DTT until the Cyt *c* was fully reduced in the solution. The intensity of Venus emission decreased after the addition of 0.25mM DTT to the cuvette. A small decrease at 550 and 537 nm was observed in the spectra (Figure 3-12a). Addition of more DTT resulted in a subsequent decrease in Venus emission that was expected due to the increasing overlap between Venus emission and Cyt *c* absorption. The change at around 537 nm was relatively small compared to the decrease at 550 nm at which the largest fluorescence decrease was measured. The fluorescence emission ratio of 550/537 nm ($F_{550/537}$) was calculated to be 0.49 for the reduced Cyt *c*. Upon addition of 0.5mM of $[Fe(CN)^6]^{+3}$, the heme in Cyt *c* –Venus was reoxidized and a rapid increase in the fluorescence emission was observed. The $F_{550/537}$ emission ratio was determined to be 0.79 at the oxidized state. In parallel, the absorption of Cyt *c*–Venus was measured using an absorption spectrophotometer in order to determine if the signal aroused from the overlap of absorption spectra (Figure 3-12b). The increased signal at 550 nm was apparent at the reduced state.

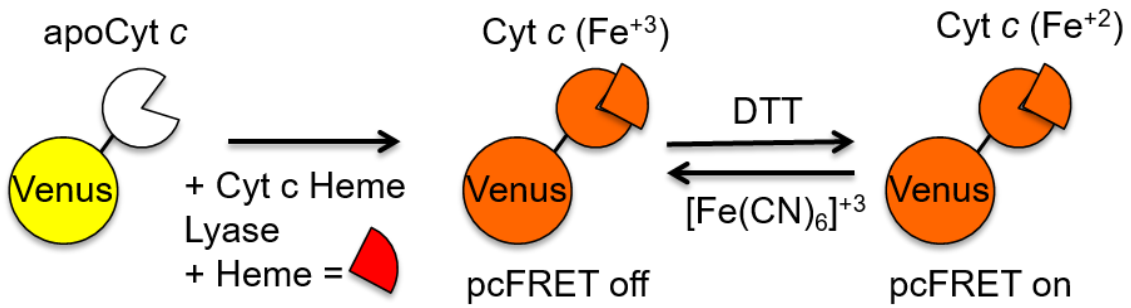

Figure 3-11 : Schematic depiction of Cyt c–Venus maturation process and pcFRET occurrence. Cyt c heme lyase catalyzed the insertion of heme into apoCyt c–Venus. pcFRET is activated by means of spectral overlap between the Venus donor to the non-fluorescent Cyt c acceptor after the reduction by DTT. Similarly, it is deactivated upon the addition of oxidizing reagent $[Fe(CN)_6]^{+3}$.

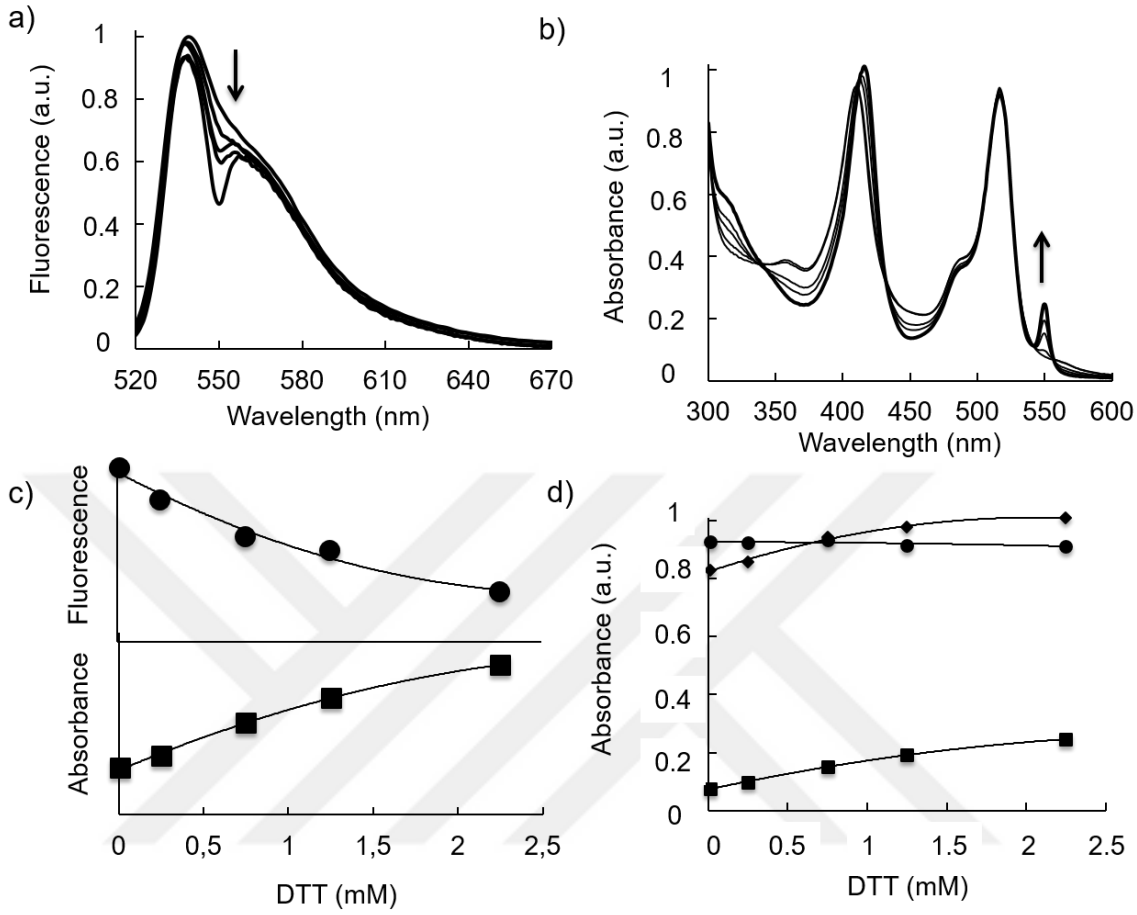

Figure 3-12 : pcFRET of Cyt c–Venus at varied DTT concentrations. a) The emission spectra of Cyt c -Venus. b) The absorption spectra of Cyt c– Venus. c) The Venus fluorescence was probed at 550 nm (top). The Cyt c absorption was probed at 550 nm (bottom). d) The titration of Cyt *c*-Venus with DTT. The normalized absorption changes at 414 nm (diamond), 515 nm (circles) and 550 nm (squares) were shown. The change of Venus absorption was undetectable while an increase was observed at 550 and 414 nm that was an indication of reduced Cyt *c* (Fe^{+2}) formation.

3.3.2. Continuous redox cycles of Cyt c with DTT and pcFRET performance of other redox reagents

To test whether photochromic FRET can be used to probe the redox change continually, the Cyt *c*–Venus was titrated reversibly using DTT and $[Fe(CN)_6]^{+3}$. 10.0 mM of reduced Cyt *c* (Fe^{+2})–Venus was transferred to the cuvette and pcFRET was characterized by the concomitant decrease at 550 nm. The redox state of Cyt *c* was identified by ratiometric analysis. The $F_{550/537}$ ratio was calculated to be 0.44 (Figure 3-13a, circles). Then, addition of 3.0 ml of $[Fe(CN)_6]^{+3}$ at 1.5 mM final concentration oxidized the Cyt *c* that led to an immediate absorbance decrease at 550 nm, shifting of the Soret peak to 407 nm and finally a broadened and smaller peak at 530 nm, consequently pcFRET did not occur. The fluorescence signal was higher at the oxidized state. $F_{550/537}$ was increased to 0.72. In the third step, the addition of DTT returned the $F_{550/537}$ ratio back to 0.45. The decrease in the pcFRET ratio indicates that the Cyt *c* was in the reduced state. We repeated changing the medium recursively and observed a similar identical fluorescence ratio for different oxidation states of Cyt *c*. The average of $F_{550/537}$ was 0.44 ± 0.01 and 0.69 ± 0.03 for the reduced and oxidized Cyt *c*–Venus respectively.

The pcFRET measurements were repeated with $[Fe(CN)_6]^{+2}$ used as a reducing agent. The fluorescence decreased in the presence of $[Fe(CN)_6]^{+2}$ and reversed as $[Fe(CN)_6]^{+3}$ was added into the Cyt *c*–Venus (Figure 3-13a, triangles). The average of $F_{550/537}$ was 0.56±0.08 and 0.75 ±0.04 for the reduced and oxidized Cyt *c*–Venus respectively. The changes in DTT and $[Fe(CN)_6]^{+2}$ were comparable and in the same magnitude that was opposite to Cyt *c* absorption in all steps. apoCyt *c*–Venus alone did not demonstrate any pcFRET at the same concentrations of DTT and $[Fe(CN)_6]^{+3}$ (Figure 3-13a, squares). The change in $F_{550/537}$ was

negligible, meaning that the Venus fluorescence emission was unaffected by the addition of redox reagents and cannot be explained by the changes around the Venus chromophore.

pcFRET was repeated with other redox reagents such asNaS_2O_4, NaN_3 and TMPD. The redox activity of Cyt *c* with different reagents was quantified by the ratio of pcFRET at the reduced and the oxidized state (Fig. 3B). The ratio varied from 0.61 to 0.78. The smallest change was observed for DTT, which had the largest pcFRET magnitude.

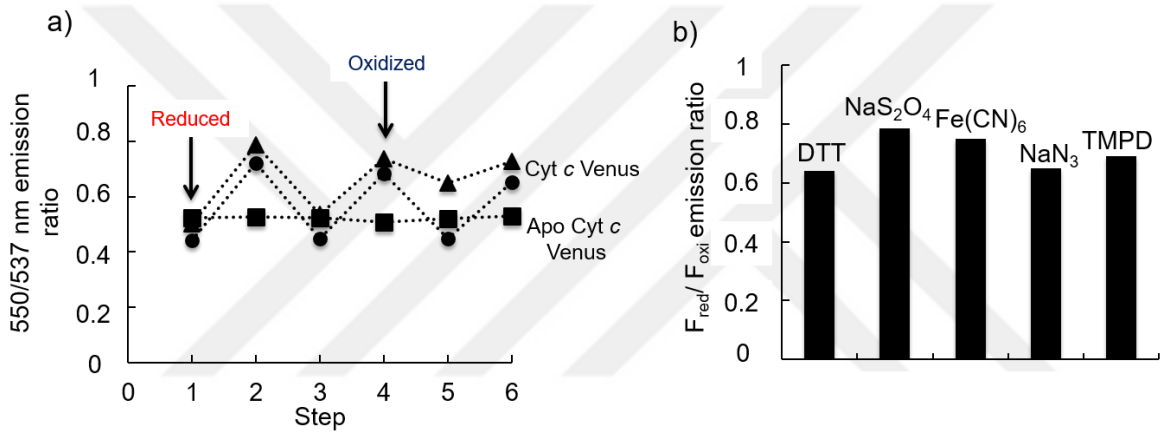

Figure 3-13: Monitoring Cyt c redox states by pcFRET. a) The odd and even steps indicating the Cyt c at reduced and oxidized states respectively. The cycle with DTT/$[Fe(CN)_6]^{+3}$ (circle), $[Fe(CN)_6]^{+2}/[Fe(CN)_6]^{+3}$ (triangle) and apoCyt c–Venus with DTT/$[Fe(CN)_6]^{+3}$ as a control sample (square). b) The ratiometric pcFRET measurement of Cyt c–Venus in the presence of different redox reagents.

Our results demonstrate that pcFRET can be used to convert Cyt *c* absorbance changes into fluorescence. The reduction of Cyt *c* resulted in higher spectral overlap with Venus. It quenched the emission of Venus fluorescence more than the oxidized Cyt *c*. The increase in $F_{550/537}$ was an indication of oxidized Cyt *c* formation and used to determine the redox state of Cyt *c*. FRET efficiency during the redox reaction was smaller than our initial predictions. On the basis of lifetime measurements, the change could be explained by a 6.6 nm separation

between Cyt *c* and Venus that was 1.8 nm longer than the Förster radius. A small Cyt *c* absorption and spectral overlap with Venus may result in less efficient energy transfer during the redox reaction. Radiative transfer and the protein orientation may explain the initial brightness change after the Cyt *c*–Venus formation in cells. However, the reduction of Venus lifetime supported the pcFRET mechanism, and concluded that heme quenched the fluorescence emission of the Venus.

Chapter 4 : FRET-BASED CYTOCHROME *C* MATURATION THROUGH HEMIN ATTACHMENT

Heme proteins of biogenesis system III are the key regulator of intracellular redox events, cellular respiration and energy metabolism[126]. Synthesis and posttranslational modification of hemin proteins are tightly controlled by chaperone and lyase enzymes that can modify proteins by correctly folding it and inserting cofactors such as protoporphyrin IX[127]. However, oxidative stress dependent changes at metabolic rate, slow maturation and misfolded proteins cause changes in redox cycle, therefore have been linked to aging and neurological diseases. The prosthetic hemin group is a key element of many redox enzymes that controls electron transfers between oxidase and reductase proteins in the mitochondria. Understanding the mechanism of heme protein maturation is crucial to establish relevant mathematical models of heme protein maturation and mechanism[128]. Cytochrome *c* (Cyt *c*) is key regulator proteins for energy metabolism and apoptosis if cells receive a signal from other metabolic pathways. Even though Cyt *c* protein has been studied extensively in previous studies, the intracellular maturation has not been understood[129]. Heme Lyase is a key enzyme for insertion of heme to Cyt c; therefore it controls the electron shuttle during the cellular respiration. However, heme lyase crystal structure has not been solved to understand binding interface between Cyt c and heme lyase. In previous studies, the catalytic domain of the heme lyase was studied by various bimolecular techniques. Despite its catalytic effect on heme insertion and recent studies, intracellular maturation of Cyt c and interaction with Heme Lyase remains elusive[130]. Here, we have studied cytochrome c maturation mechanism via binding to

cytochrome c heme lyase. Briefly, Cyt c and Heme lyase enzyme was attached to C and N terminus of Cerulean-Venus FRET pair respectively. Then, we have measured the fluorescence energy transfer after expressing both proteins in cells. Fluorescence resonance energy transfer provides a sensitive tool to study protein-protein interactions and protein conformational changes in living cells. It is the most effective tool to measure small conformation changes and characterize protein-binding events.

4.1. Sample Preparation

4.1.1. Reagents

Hyclone Dulbecco's Phosphate Buffer Saline (DPBS)/Modified (1X) with Calcium, Magnesium and Hyclone PBS (1X) without Calcium, Magnesium were obtained from Thermo Scientific (Waltham, MA, USA). Dulbecco's Modified Eagle Medium (DMEM) sterile filtered, Fetal Bovine Serum (FBS) sterile filtered heat inactivated, Penicillin-Streptomycin and 4,6-dioxoheptanoic acid (succinylacetone) were purchased from Sigma-Aldrich (St. Louis, MO, USA). 0.05% Trypsin-EDTA (1X) , Opti-MEM® (reduced serum media) and Turbofect® transfection reagent were obtained from Gibco (Life Technologies Ltd., Paisley, Scotland) and FuGENE® HD (FuGENE LLC, Wisconsin, USA) was purchased from Promega (Fitchburg, WI, USA). Chemicals were used as received without any further purification.

For immunofluorescence (IF) staining Triton X-100, BSA (powdered, lyophilized), paraformaldehyde, methanol free, 16% (Diluted with 1X PBS to 4%), Mowiol mounting media purchased from VWR Chemicals (Radnor, Pennsylvania, USA). β-tubulin Mouse mAB (monoclonal antibody) primary antibody and corresponding Goat anti-Mouse IgG2b Alexa Fluor® 555 conjugate secondary antibody and DAPI staining obtained from Cell Signaling,

(Danvers, MA, USA). IF antibodies and dyes were used according to manufacturer's prescription and protocol.

4.1.2. Recombinant DNA construct design and protocol

The mCerulean C, Venus, and C17V plasmids containing Cerulean FP, Venus FP and Cerulean attached via 17 amino acids (a.a.) linker to Venus FP genes, respectively, were kindly provided by Asst. Prof. Nathan Lack of Koç University Medicine School, Sarıyer, Istanbul. In FRET experiments, Cerulean FP considered as the donor and Venus FP as the acceptor the protein. The C17V plasmid, containing Cerulean and Venus comprised FRET pair standard, was used as a scaffold to construct C-Cyt *c*-V and C-Cyt *c* Heme Lyase-V recombinant plasmid DNA.

After the PCR amplification of Cyt *c* and Cyt *c* Heme Lyase encoding gene sequence from previously developed recombinant DNA construct Cyt *c*-Venus using the forward and reverse primers (Table 3), two non-existing restriction sites (XhoI (Forward) & HindIII-HF (Reverse) for Cyt *c*, XhoI (Forward) & KpnI (Reverse) for Cyt *c* Heme Lyase) were introduced to their flanking ends. For the expression of C-Cyt *c*-V and C-Cyt *c* Heme Lyase-V constructs, Cyt *c* and Cyt *c* Heme Lyase genes were attached between Cerulean and Venus FPs which are located in the N- and C- termini respectively. The inserts are ligated through the corresponding restriction sites (XhoI & HindIII-HF couple for Cyt *c*, XhoI & KpnI couple for Cyt *c* Heme Lyase) of digested C17V plasmid via standard subcloning method(Figure 4-1 & 4-2). The sequence of each plasmid was verified at the sequencing center of Macrogen Inc (Amsterdam, The Netherlands) (Table 4-5).

Table 3 : The sequence of the primers used for the cloning of Cyt *c* and Cyt *c* Heme Lyase encoding genes into C17V vector plasmid having Cerulean and Venus FPs as a FRET pair.

Primer Sequence	Description
5’ – AAA ACT CGA GTG ACT GAA TTC AAG GCC GGT – 3’	Forward primer for Cyt *c* amplification
5’ – AAA AAA GCT TCA CTG GCT TTT TTC AAG TAG – 3’	Reverse primer for Cyt *c* amplification
5’ – AAA ACT CGA GTG AAT TCA CAA AAA ATG GGT – 3’	Forward primer for Cyt *c* Heme Lyase amplification
5’ – AAA AGG TAC CCA TCC GGT CCT TAG CAT TGT – 3’	Reverse primer for Cyt *c* Heme Lyase amplification

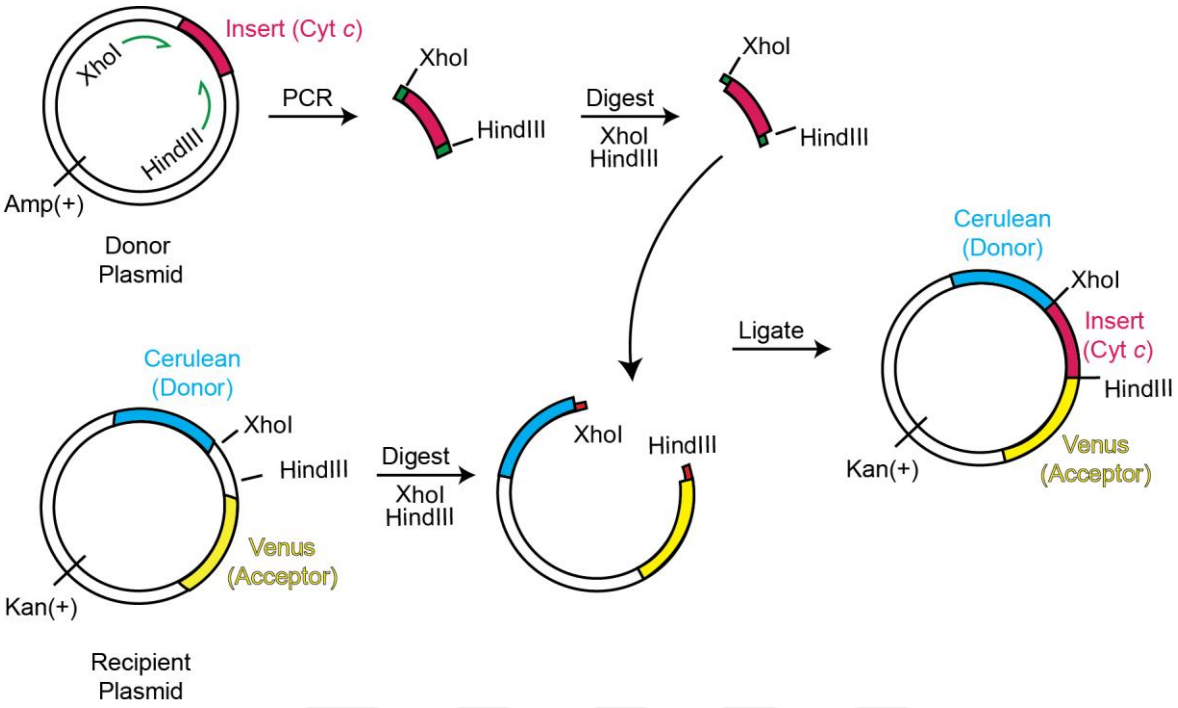

Figure 4-1 : Schematic of the cloning protocol for preparing C-Cyt *c*-V plasmid construct.

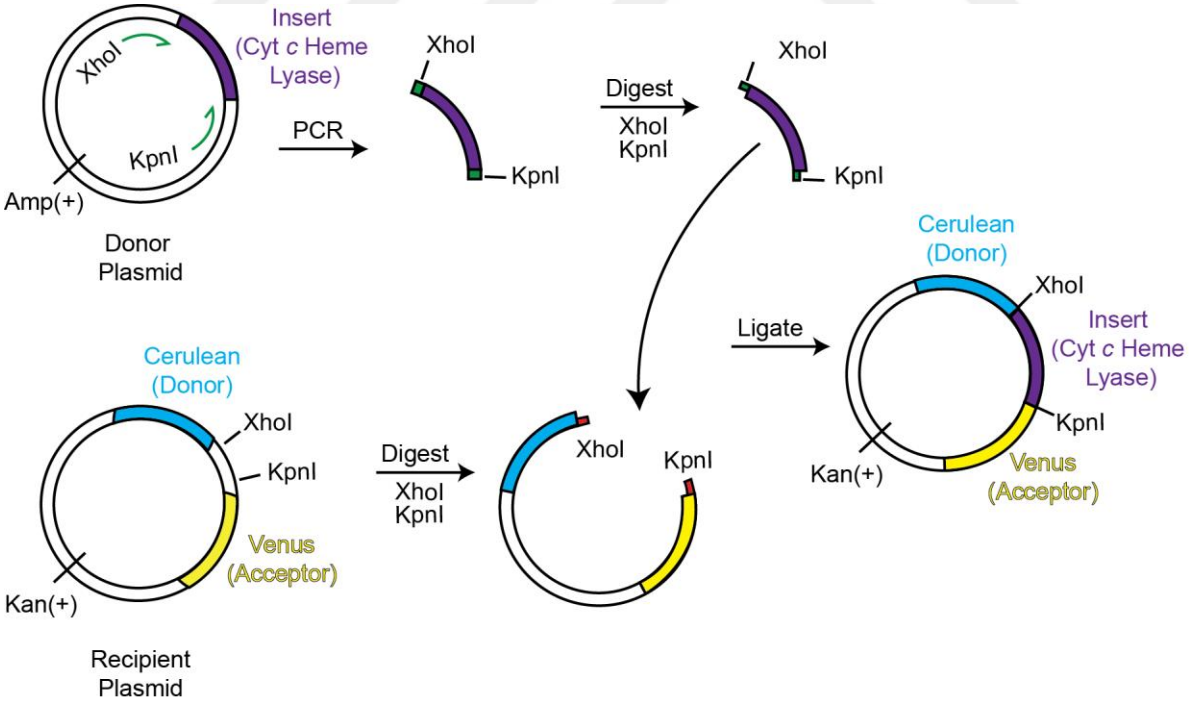

Figure 4-2 : Schematic of the cloning protocol for preparing C-Cyt *c* Heme Lyase-V plasmid construct.

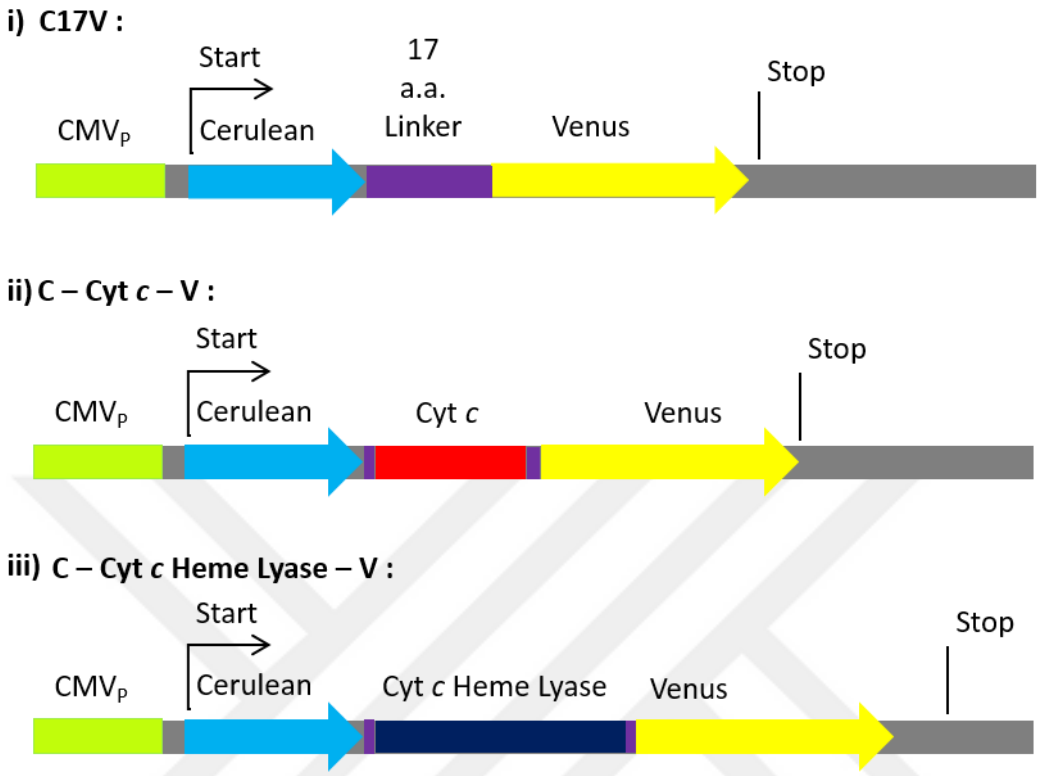

Figure 4-3 : Schematic representation of the recombinant DNA constructs. i) C17V ii) C-Cyt *c*-V iii) C-Cyt *c* Heme Lyase-V plasmid construct.

Table 4 : The nucleotide sequence of C-Cyt *c*-V encoding region. The sequence of the plasmid was verified at the sequencing center of Macrogen Inc. (Amsterdam, The Netherlands). The simulated recombinant DNA construct and Macrogen sequencing results were aligned in Serial Cloner Freeware2.6.1 (Franck Perez) for verifying the matching. (Cyan: Cerulean, Orange: XhoI restriction site, Red: Cyt *c*, Dark Blue: Hind III restriction site, Green: Venus)

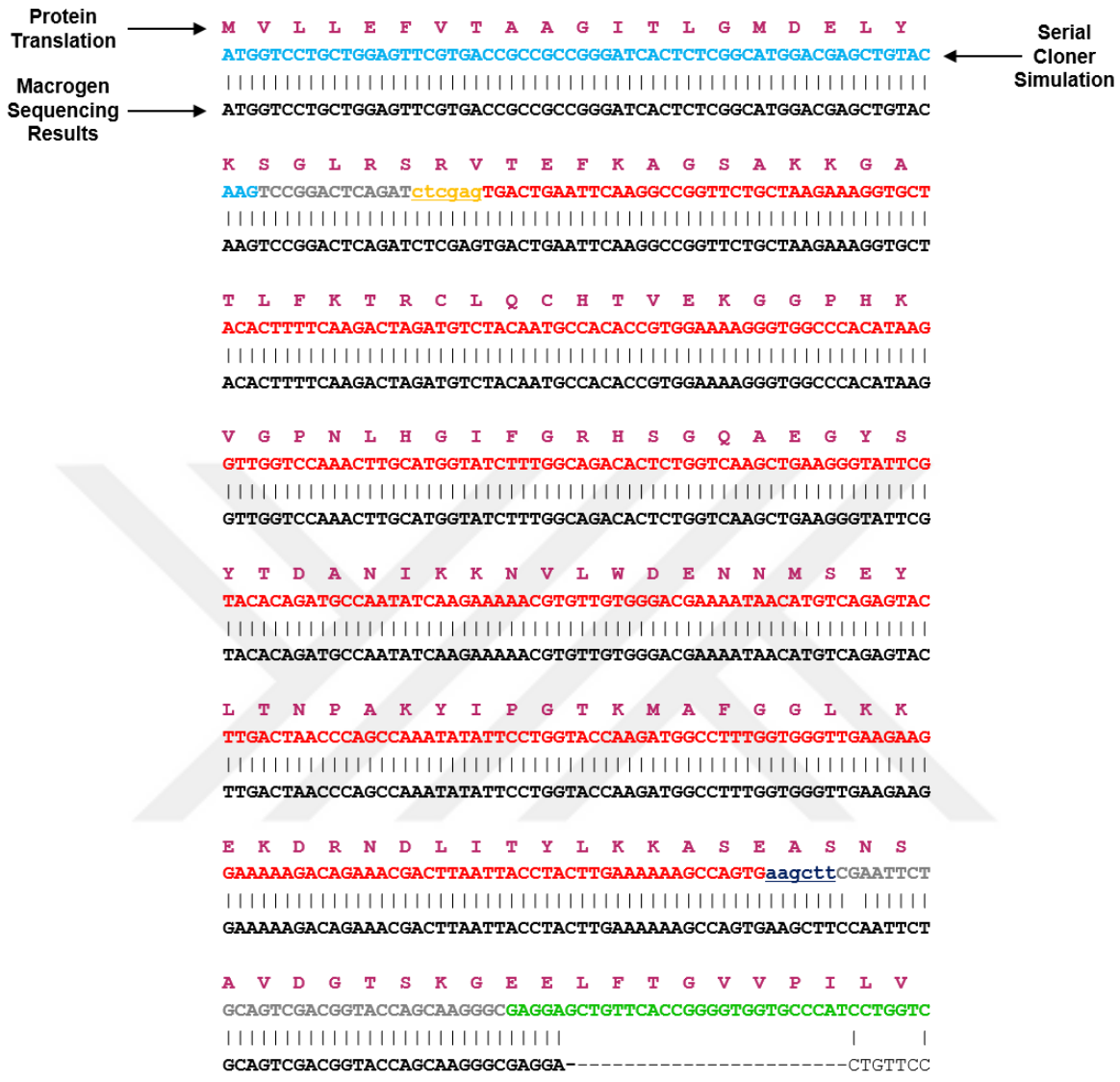

Table 5 : The nucleotide sequence of C-Cyt *c* Heme Lyase-V encoding region. The sequence of the plasmid was verified at the sequencing center of Macrogen Inc. (Amsterdam, The Netherlands). The simulated recombinant DNA construct and Macrogen sequencing results were aligned in Serial Cloner Freeware2.6.1 (Franck Perez) for verifying the matching. (Cyan: Cerulean, Orange: XhoI restriction site, Purple: Cyt *c* Heme Lyase).

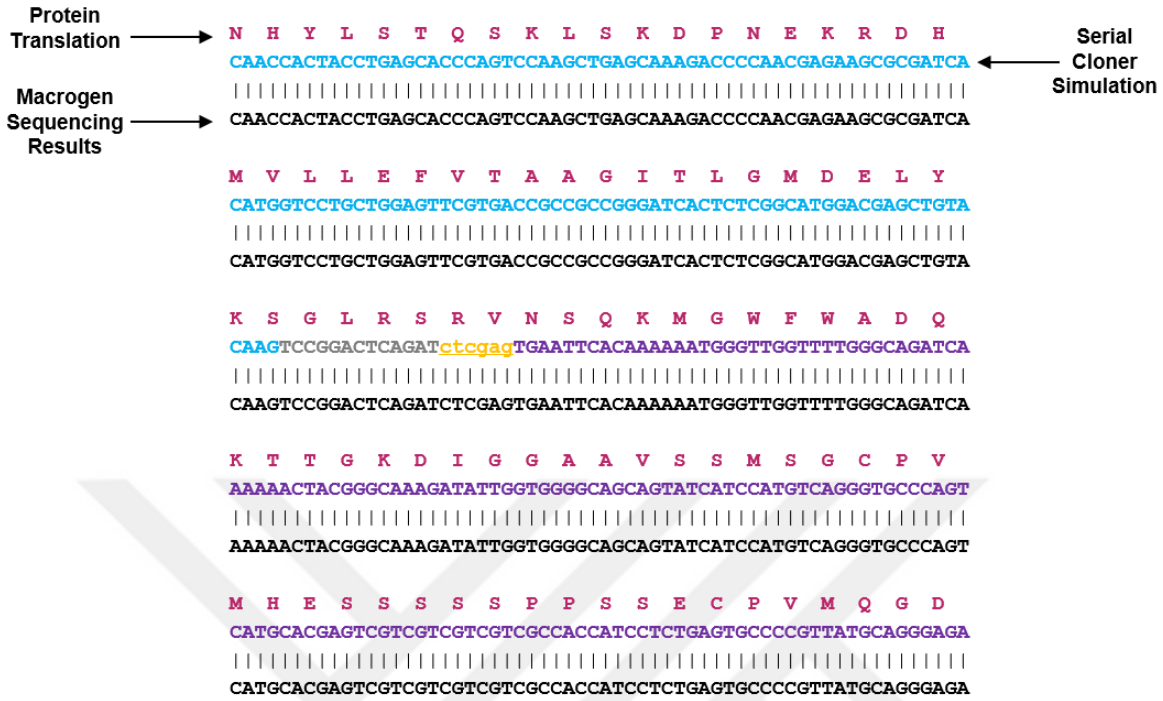

4.1.3. Cell culture maintenance and transfection

Cell culture

HEK293T and HELAS3 cells, used for live cell and IF experiments, were kindly provided by Nathan Lack and Nurhan Ozlu, respectively, from Koç University, Istanbul. Complete DMEM solution composed of DMEM with high glucose, 10 % FBS and 1 % Penicillin/Streptomycin was used for the regular growth of the cells in fibronectin coated cell culture plates that are placed inside the incubator at 37^0C with 5 % CO_2 supplement. Cells were passaged every two days to avoid overpassaging and overgrowth.

When plate confluency reaches >70%, cells are harvested. For harvesting the cells, aspirate the medium and gently wash away unattached cells with pre-heated PBS (with Ca^{+2} and Mg^{+2}). Then supply 1ml of 0.05% trypsin EDTA solution to detach the cells from plate substrate by weakening adherent molecules and incubate the plate for 3-5 min in the

incubator. Later, provide 3ml of complete DMEM solution on top of it to neutralize the effect of trypsin EDTA. After transferring this harvested cell solution to a 15 ml falcon tube, cells are pelleted through centrifugation for 5 min at 1400 rpm. For a 6-well and 12-well plate, $0.3x10^6$ cells in 2ml and $0.1x10^6$ cells in 1 ml are seeded, respectively, by adding the calculated volume of harvested cell solution after counting with hemocytometer at a 1:10 dilution factor (DF).

$$\frac{\#\text{ of cells}}{\text{ml}} = \frac{\#\text{ of cells in 4 wells of hemocytometer}}{4} * \text{DF} * 10.000 \qquad \text{Eq. 5}$$

For storage purposes, a plate with >80% confluency is divided into at least 3 vials. All the steps through cell collection is the same as described above. After centrifugation, cell pellet is resuspended with complete DMEM having 30% FBS 10% DMSO to transfer harvested cells into cyrotube vials and store at -80^0C.

Transfection

One day before the transfection, cells are seeded on 12-well plates with $0.1x10^6$ cells/well confluency. Cells are ready to transfect approximately 18 hours after the seeding process where they reach around 50% confluency. In a clean Eppendorf tube, the transfection cocktail including DNA, OPTIMEM® and transfection reagent is prepared. For a single well, the transfection cocktail contains 500 ng DNA, 100 µL OPTIMEM® (reduced serum media) and 1.5 µL FuGENE® HD or TurboFect™ transfection reagent (1000 ng DNA:3 µL transfection reagent ratio is applied). The solution is mixed by gentle finger-tipping and span for 5 seconds to avoid bubbling. Later, it is incubated for 30 min at room temperature (R.T.) and placed on wells in a dropwise manner. The cells are sufficiently transfected and ready for image acquisition 6 hours after the transfection.

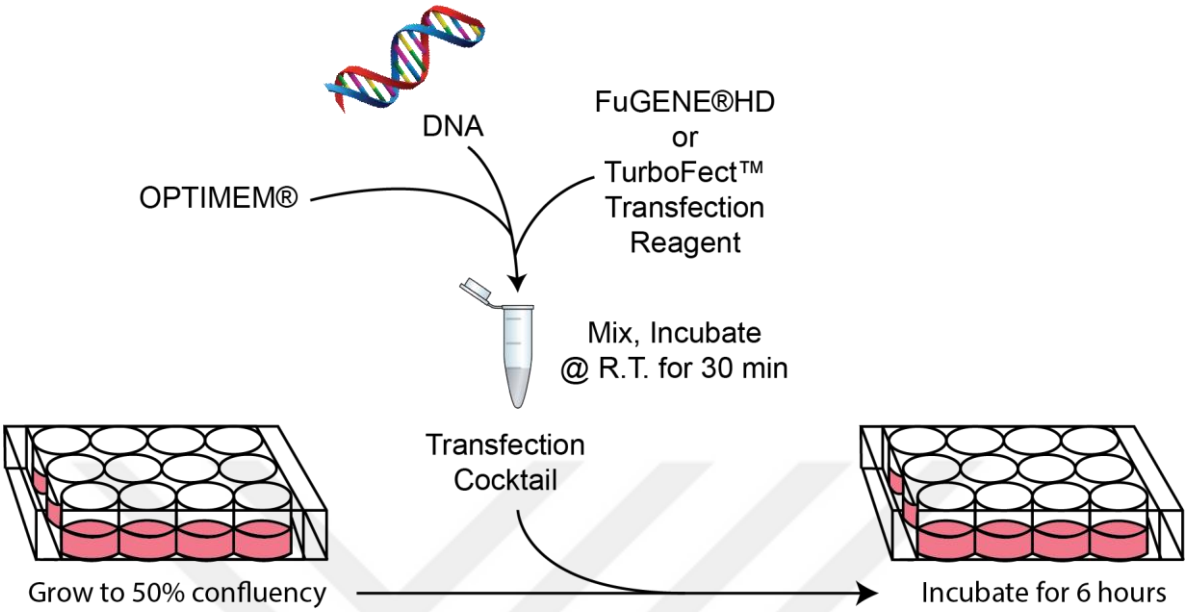

Figure 4-4 : Schematic of mammalian cell transfection protocol.

4.2. FRET Experiments and Data Analysis

4.2.1. Live cell microscopy experiments and single-cell tracking

Olympus Xcellence Xi81 inverted epi-fluorescence microscope equipped with a 20X air objective having numerical aperture of 0.4 was used for image acquisition. The cells were maintained in the microscope incubator for almost 13 hours at 37 ºC temperature with 5 % CO_2 supplement. The images were recorded with an Andor Ixon3-897 reinforced by a quantitative digital camera technology called Electron Multiplying Charge Coupled Device, EMCCD. The images were acquired in four channels: phase, CFP (Exc: 427±10, Emis: 475±20), YFP (Exc: 504±12, Emis: 542±27) and CFP_YFP (FRET) (Exc: 427±10, Emis: 542±27) for fluorescence images. Before starting the experiment, 10-15 points were selected from each well of a 12-well plate and scanned with a 10 min/image frame rate and 75ms exposure time during image acquisition. The movie clips were recorded using custom data

acquisition software and analyzed with MATLAB (R2014a, The MathWorks, Natick, Massachusetts).

In order to estimate the cell trajectories, all experiment movies were processed with a custom written script in MATLAB. It is comprised of four sections including image segmentation, pixel noise removal, cell coordinate identification and coordinate sorting for linking the cell's trajectory. Initially, all images are segmented using a threshold filter calculated from the background signal and convoluted with a low pass Gaussian kernel filter to remove the pixel noise. These smoothed images are used for estimating the cell coordinates in each frame.

Later on, the centroid position of a cell is located from intensity values. . The local maximum which is considered as the centroid of a cell is obtained with respect to intensity values of pixels. In case of having more than one pixel with highest intensity value in a cell, the centroid location of these local maxima points is calculated and used in the following calculations. Each point coming from a single cell and the number of these maxima points are used for defining the centroid positions of the cells'. If the noise pixels were not eliminated, they would count as a cell centroid and this inaccurate counting would cause error in results. Therefore, it is crucial to perform a convolution beforehand to remove the pixel noise from the images and avoid the over count of centroids caused by noise pixels. After finding the number of maxima points which also gives the cell number, the results are generated as a list for each frame. The list shows cell number, x and y coordinates of each cell in the frame and intensity value of the centroid position.

The displacement of an individual cell between consecutive frames was determined by computing the mean square displacement and estimating their positions. After repeating the

procedure for all cells, the positions of cells in each frame were registered for the construction of trajectory and statistical analysis. Later, the tracking part employs probability to connect the positions in each frame sequentially by using previously obtained positions of the identified cells in all frames.

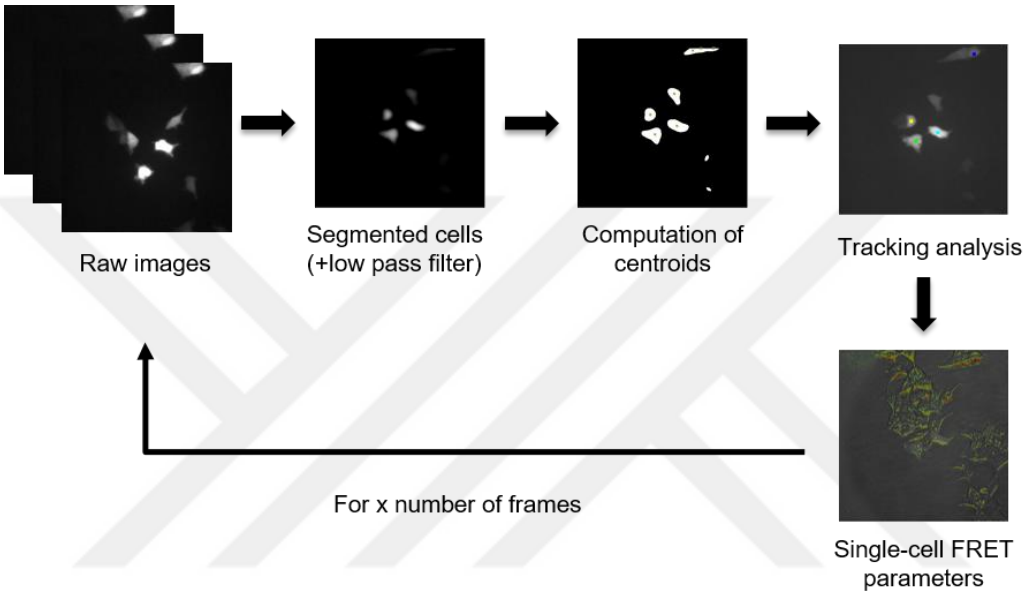

Figure 4-5 : The schematic of single-cell tracking algorithm.

4.2.2. Correction coefficients and FRET signal calculations

Each identified cell's temporal fluorescence intensity change in donor, acceptor and FRET channels are obtained after the completion of single-cell tracking analysis as previously described. Later on, this intensity data is used for the net FRET calculation with the equation below[131],

$$nF = I_{FRET} - I_{YFP} * \alpha - I_{CFP} * \beta \qquad \text{Eq. 6}$$

Where I_{FRET}, I_{YFP}, I_{CFP} are the fluorescence intensities of a specific cell collected in each region of interest under FRET (donor excitation and acceptor emission), YFP (acceptor excitation and acceptor emission), and CFP (donor excitation and donor emission) filter sets respectively.

The coefficients α and β are the ratio of the signal in FRET channel to the signal in YFP channel in the absence of donor and to the signal in CFP channel in the absence of acceptor[132].

$$\alpha = \frac{I_{FRET}}{I_{YFP}} \ , \ \beta = \frac{I_{FRET}}{I_{CFP}} \qquad \text{Eq. } 7-8$$

These coefficients are obtained from the measurement in the cells that are transfected with donor or acceptor protein only. It is important to correct the nFRET signal using these coefficients to prevent the bleed-through of the non-FRET CFP and YFP fluorescence due to their excitation at the excitation wavelength of CFP[133].

Obviously, a positive net FRET signal from the cells transfected with a fusion protein, containing the protein of interest between FRET couple proteins, indicates a non-radiative fluorescence energy transfer from donor to acceptor[134]. Therefore, the magnitude of donor and acceptor fluorescence elimination from FRET channel is crucial for the accurate estimation of nFRET[135]. The amount of fluorescence intensity needed to be removed from the raw FRET (rFRET) channel depends on the fluorescence intensity retrieved from donor or acceptor channel and their corresponding coefficients. Since donor and acceptor channel intensities are collected without any further alteration, the quantity of fluorescence subtraction is coefficient oriented.

In conventional nFRET calculations, these correction coefficients are considered as static values and depend on imaging system conditions. They are determined by analyzing a single image of the cells expressing only CFP or YFP and quantifying the relative intensity ratio under FRET/CFP or FRET/YFP filter sets[136]. However, the fluorescence emission of donor or acceptor transfected cells undergoes an exponential decay in time and reaches to a

saturation after a point. Thus, accepting these coefficients as fixed values would ignore their dynamic fluorescence fluctuation in time and result in incorrect nFRET calculation.

Here, we employ a custom written script to determine the altering profile of correction coefficients. The estimation of donor and acceptor coefficients is the first part of the post-experimental data analysis and the images of cells transfected with donor or acceptor are utilized for the calculations. The movies of donor and acceptor expressing cells are first uploaded and read into generated matrices. The coefficients are then assessed through pixel wise ratio of FRET channel movies to donor or acceptor channel movies for all frames, where each movie has a pixel size of 512x512. At this point, the coefficient distribution of a movie is screened for all frames and each scatter is fitted with a curve.

In the last part, the average of coefficient fitting curves for all frames of the movie is taken to estimate the coefficient profile of the corresponding donor or acceptor sample's ROI. In each experiment 10-15 points are selected from donor and acceptor expressing samples individually. For calculating the overall temporal coefficient values, the frame-by frame average of all ROI's coefficient values are taken after the removal of the outlier data causing unwanted distortion. Later on, these general donor and acceptor coefficients are utilized for the nFRET value calculation in each frame of FRET occurring samples' movies. By this means, a robust temporal nFRET estimation is ensured since non-FRET donor and acceptor fluorescence are removed through the multiplication of their intensities in the corresponding channel with the frame specific global correction coefficients.

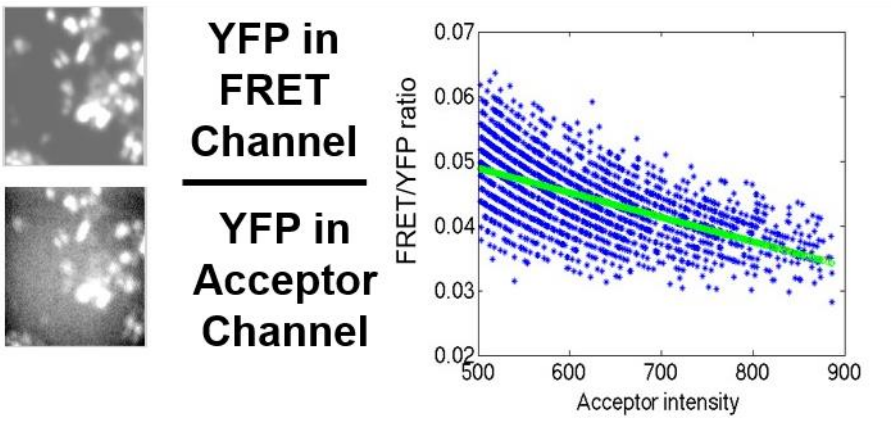

Figure 4-6 : An example of frame specific coefficient distribution calculated by the pixel wise ratio of FRET channel to donor or acceptor channel.

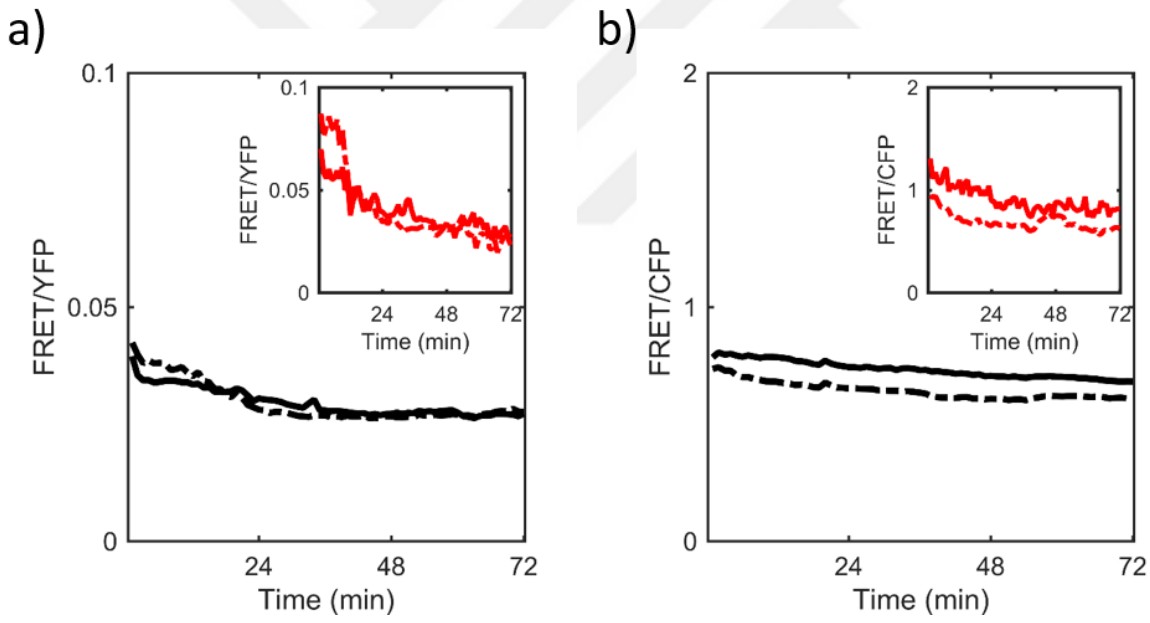

Figure 4-7 : Dynamic nFRET correction coefficients calculated by taking the ratio of the FRET signal to donor or acceptor signal continuously throughout the experiment duration. a) Coefficient for acceptor channel intensity (α) b) Coefficient for donor channel intensity (β). The overall average of coefficient profiles of all ROIs' from donor and acceptor samples with constant (black) and estimated (red) fitting. The spots demonstrating outlier fluctuations are

removed to have a uniform decaying profile among all donor or acceptor ROIs. (Average of selected ROIs: dashed and all ROIs: solid).

The calculated nFRET value by using correction coefficients of donor and acceptor fluorophores, is represented as normalized FRET (NFRET) ratio for providing relevancy with previously studied literature findings. The NFRET ratio is calculated by the equation below[132],

$$NFRET = \frac{nFRET}{\sqrt{I_{CFP} * I_{YFP}}} \qquad \text{Eq. 9}$$

The so-called cross-talk talks between donor and acceptor fluorescence and between FRET and non-FRET fluorescence emitted from donor and/or acceptor are major concerns in FRET measurements with fluorescence microscopy[135]. Therewithal, other factors such as quantum yield of fluorophores, photobleaching/quenching, and molecular position/orientation could also affect the FRET measurements. Hence, it is essential to have reliable positive and negative controls for the accurate FRET quantification[134]. The three-filter cube system like the one used in this study sufficiently eliminates the unwanted effect of the cross-talk between donor and acceptor fluorescence. The photobleaching of GFP and its variants is minor under experimental conditions since they showed no significant emission intensity loss.

NFRET is accepted as a reliable quantification method since it considers the FRET efficiency, calculated as nFRET, and its normalization against donor and acceptor expression[132]. Therefore, NFRET values are functions of both the FRET efficiency (distant dependent) and the ratio of the combined donor acceptor structures to total number of individually present donors and acceptors (concentration and affinity dependent). Moreover, the utilization of frame specific correction coefficients in the NFRET formulization also augments its accuracy level.

4.2.3. Statistical analysis

The presented NFRET or nFRET data refer to independent replicates of independent cell samples that are seeded, transfected, treated and analyzed on different days. The MATLAB Statistics and Machine Learning Toolbox is utilized for testing the statistical significance of the differences in reported values. The P values smaller than 0.05, 0.01, 0.001 were considered statistically significant and indicated with 1, 2, 3 asterisks, respectively. P values equal to or bigger than 0.05 were acknowledged as statistically not significant.

The one-sample Kolmogorov-Smirnov test is used for determining the distribution profile of experimental values. This test returns a decision for the null hypothesis that the entered data comes from a standard normal distribution, against its alternative where data does not come from such distribution[137]. It returns the result, *h*, as 1 with a small *p-value* which is the probability of obtaining a result that is equal or more extreme than what is observed, at 5% significance level if the test rejects the null hypothesis[138]. The testing of calculated nFRET and NFRET data from all samples give a not normal distribution result which confirms the utilization of nonparametric statistical methods for further analysis.

The statistical significance of differences between the samples were assessed through two-sample Kolmogorov-Smirnov test, a non-parametric hypothesis test, which returns the result for the null hypothesis that the provided data in column vector x1 and x2 come from the same continuous distribution[139]. The alternative hypothesis accepts that the column vectors x1 an x2 come from different continuous distributions. The test result h is 1 if the test rejects the null hypothesis at the 5% significance, and 0 in other case. Basically, two-sample Kolmogorov-Smirnov test evaluates the difference between the cumulative distribution functions that are derived from the continuous distributions of the two sample data vectors and, therefore, it is found appropriate for performing the statistical comparison between

different nFRET and NFRET samples where the nature of the data has a spatio-temporal dynamic and the alterings occur as a slight shift in the kinesis profile.

The sample size for each experiment were planned according to an initial pilot experiment. Similar experimental designs reported in previous studies were further consulted to direct sample sizes. No randomization or blinding technique was used during the experiments, and, as well, no data manipulation performed in the analysis part.

4.3. Characterization

4.3.1. Immunofluorescence (IF) staining for protein localization

The adherent mammalian cells are transfected with the desired recombinant DNA constructs according to previously described transfection protocol and incubated for 24 hours to achieve a sufficient transfection efficiency. On the following day, the cells are collected and seeded into an appropriate multi-well well plate with the identified seeding density if they demonstrate an adequate expression. Before seeding, the standard glass coverslips, having 12mm diameter and 1.5 mm thickness, are placed in each well of the plate. The seeded cells are grown for overnight in complete DMEM culture medium under physiological incubation conditions to reach ~50%-60% confluency on the staining day.

On the day of experiment, the permeabilization/blocking solution is freshly prepared by dissolving 0.25 g of BSA in 1X PBS and adding 150 µL of Triton X-100 (TX-100) from 20% stock solution to have a 1XPBS with 2.5 BSA and 0.3%TX-100. Later on the following protocol is performed for IF staining.

A. Fixation

1. Gently, aspirate the complete DMEM medium of the cells and wash with 1X PBS.

2. Take the cover slips with the aid of the needle and tweezer and place them on a parafilm coated petri dish. Aspirate the excess medium by touching a corner of the coverslip with the suction. The facing side the coverslips should have the attached cells.
3. Quickly, place 50-100 µL of freshly thawed 4% paraformaldehyde (prepared by diluting the 16% paraformaldehyde stock solution with 1X PBS and stored at -20ºC in aliquots) on the coverslips by touching one edge of it. Avoid drying of coverslips.
4. Incubate the coverslips in the incubator for 15 min at 37 ºC.
5. Aspirate the fixative and rinse the coverslips 3 times with 1X PBS for 5 min each.

B. Permabilization and Blocking

1. Incubate the coverslips for 30 min with 1X PBS, 2.5% BSA, 0.3% TX-100 at room temperature.

C. Immunostaining

1. Incubate the coverslips with the primary antibody diluted in 1XPBS containing 2.5%BSA and 0.3%Triton X-100 for 2 hour at room temperature or overnight at 4ºC.
2. Aspirate the antibody and rinse 3 times with 1X PBS for 5 min each.
3. Incubate the coverslips with the secondary antibody diluted in 1XPBS containing 2.5%BSA and 0.3%Triton X-100 for 1 hour at room temperature in the dark. After this stepi try to minimize the light interaction of coverslips as much as possible.
4. Aspirate the antibody and rinse 3 times with 1X PBS for 5 min each.

OR

Simultaneous incubation for more than antibody utilization

1. Incubate the coverslips with primary antibodies diluted in 1XPBS containing 2.5%BSA and 0.3%Triton X-100 for 2 hour at room temperature or overnight at 4^{o}C.
2. Aspirate the antibody and rinse 3 times with 1X PBS for 5 min each.
3. Incubate the coverslips with secondary antibodies diluted in 1XPBS containing 2.5%BSA and 0.3%Triton X-100 for 1 hour at room temperature in the dark. After this stepi try to minimize the light interaction of coverslips as much as possible.
4. Aspirate the antibody and rinse 3 times with 1X PBS for 5 min each.

D. Counter Staining

1. Incubate the coverslips with DAPI stain for DNA material colorization diluted in 1XPBS for 10 min.
2. Aspirate the medium and rinse 3 times with 1X PBS for 5 min each. Left the last wash step's PBS on the coverslip and continue with the next section.

E. Mounting

1. Put a drop of mounting media on the glass slide.
2. Handle the coverslips with a tweezer and aspirate the PBS by touching a corner with the suction. Turn down the facing side of the coverslips and leave them gently on the mounting media with a 45^{o} degree. The mounting media will propagate in whole glass are quickly.
3. Seal the edges of the coverslip with a nail polish to prevent drying or movement under the objective.
4. Store the glass slides in dark at 4 ^{o}C and -20 ^{o}C for short and long term use, respectively.

The IF slides are screened and photographed with Nikon Eclipse 90i upright confocal microscopy system equipped with Pan Apo VC 60X Oil objective with a N.A. of 1.40 and argon ion laser. The images are acquired in DAPI, FITC and TexasRed channels having 408/488, 485±15/540±20, 543/630 and excitation/emission filters respectively.

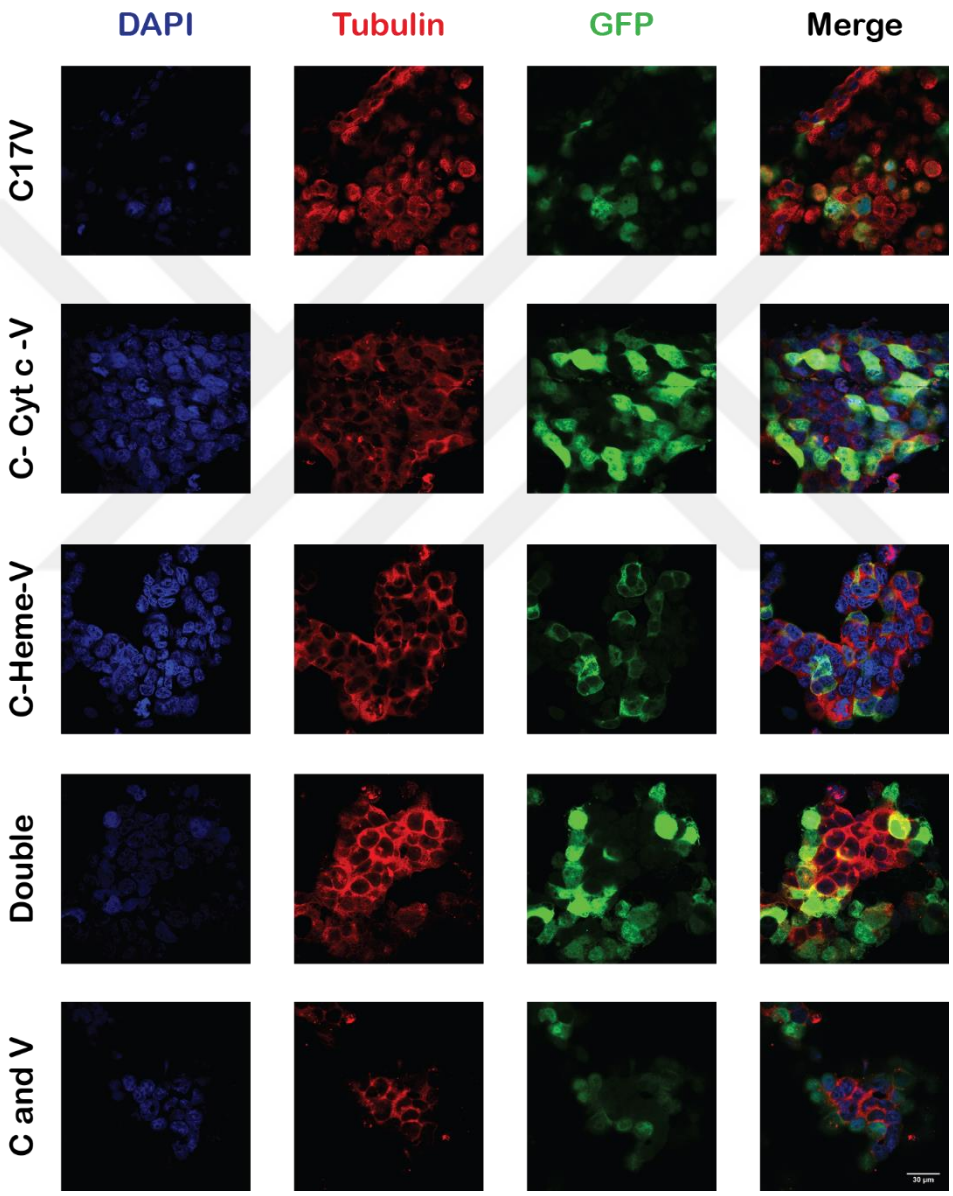

Figure 4-8 : Confocal images of HEK293T cells transfected with C17V, C-Cyt *c*-V, C-Cyt *c* Heme Lyase-V constructs and double transfected with C-Cyt *c*-V/C-Cyt *c* Heme Lyase-V and Cerulean/Venus paired constructs. Microtubules (red) were stained with monoclonal anti-β-

tubulin antibody () and followed by goat Alexa Fluor® conjugated anti-mouse antibody (#4409) with a dilution of 1:1000 and 1:2000 respectively (Cell Signaling, Danvers, MA, USA). In the last step DNA (blue) was stained with DAPI (#4083, Cell Signaling, Danvers, MA, USA) with a dilution of 1:2000. Scale bar, 30 μm.

The IF images were used for determining the protein localization around the cell. Positive control C17V, C-Cyt *c*-V and negative control Cerulean and Venus double transfect samples demonstrated protein expression both in the nucleus and cytosol, whereas C-Cyt *c* Heme Lyase-V sample tended to concentrate in the cytosolic compartment. The double transfection product of C-Cyt *c*-V and C-Cyt *c* Heme Lyase-V constructs, indicated a combinatory localization of its components having cytosol and nucleus and cytosol only appearance.

4.3.2. Protein localization under epi-fluorescence microscopy

The protein localization of 3 different construct designs also examined under epi-fluorescence microscopy. The nuclear and cytosolic expressions of C-17V and C-Cyt *c*-V constructs and only cytosolic expression of C-Cyt *c* Heme Lyase-V construct are found to relevant with IF images. The fluorescence intensities of protein expressions are used for calculating the rFRET and nFRET values for the corresponding constructs.

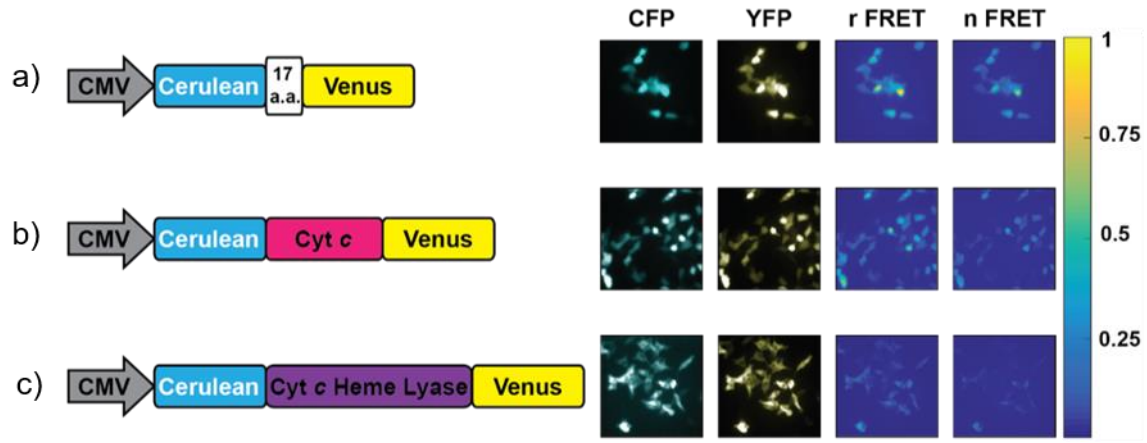

Figure 4-9 : The protein localization of constructs in epi-fluorescence microscopy and the colorbar for assigning the corresponding rFRET and nFRET fluorescence intensities of protein expressions. a) C17V, b) C-Cyt *c*-V, c) C-Cyt *c* Heme Lyase-V.

4.4 Results and Discussion

4.4.1. Estimation of molecular distance through FRET measurements

FRET is a physical phenomenon that describes the energy transfer between two fluorophores. A donor chromophore in its excited state can transfer its energy to an acceptor through nonradiative dipole dipole coupling. The efficiency of FRET is inversely proportional to the sixth power of the distance between donor and acceptor, and therefore makes it very sensitive infinitesimal changes in distance. This property of FRET makes it a useful ruler to measure the molecular distance. The equation below is used for estimating the donor-to-acceptor separation distance r

$$E = \frac{1}{1 + (\frac{r}{R_o})^6} \qquad \text{Eq. 10}$$

Where R_0 is the Förster radius for a specific donor-acceptor couple which corresponds to 50% of the energy transfer efficiency. The corresponding donor-acceptor separation of

each sample is calculated through normalized FRET efficiency value, NFRET. The R_o is taken as 5.3 nm for Cerulean and Venus FRET pair.

The positive control sample, C17V, had the shortest donor-acceptor separation (5.8 nm) since it has only 17 amino acids between two fluorophores. The double transfection of Cerulean and Venus constructs demonstrated the longest separation since the fluorophores are individually expressed and not connected with a linker. Therefore, their separation is considered as bigger than 10 nm which is the critical limit for FRET observance.

Interestingly, C-Cyt *c*-V and C-Cyt *c* Heme Lyase-V FRET constructs exhibited the same separation distance with 6.7 nm even though the insert Heme Lyase protein is 2.5 times longer than Cyt *c*. This finding suggests close proximity of N- and C-termini of Cyt *c* Heme Lyase protein which is a notable inference since it exact crystal structure is not known.

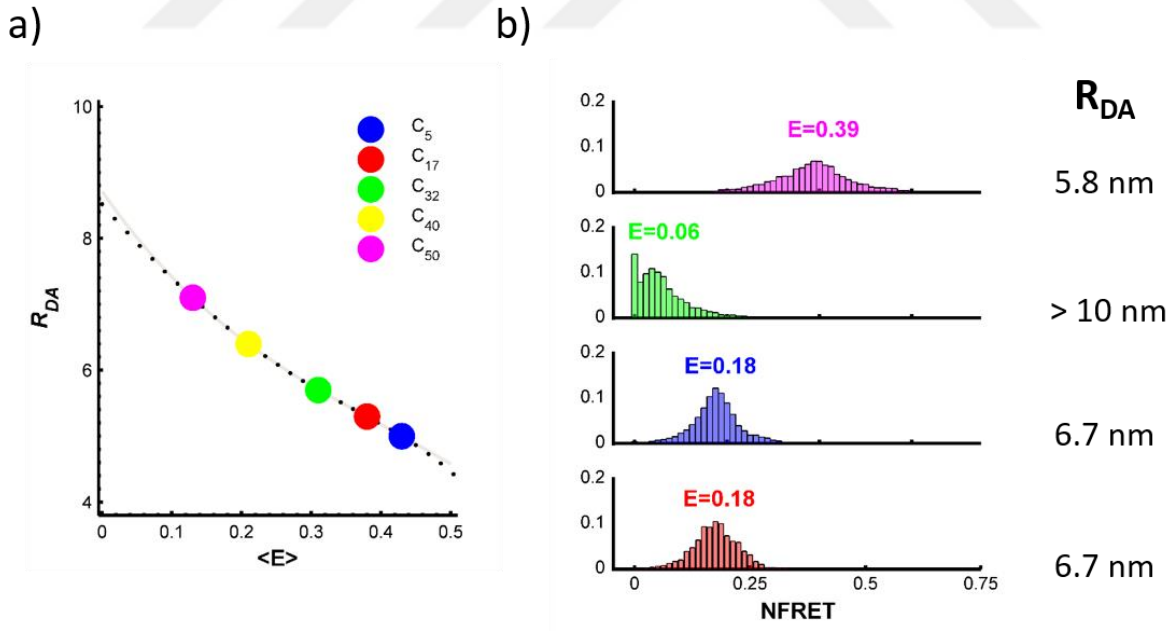

Figure 4-10 : The molecular real distances between donor and acceptor fluorophores for a given FRET efficiency value. a) The calculated R_{DA} values, the real molecular distance, for measured FRET efficiencies, <E>, of mCerulean and mVenus constructs with varying linker length of 5 (blue), 17 (red), 32 (green), 40 (yellow) and 50 (magenta) amino acids. The R_o,

Förster radius, is taken as 5.3 nm[140]. b) The NFRET histograms of C17V (magenta), Cerulean&Venus (green), C-Cyt *c*-V (blue), C-Cyt *c* Heme Lyase-V samples and their corresponding histogram averages. The average NFRET values are used for estimating the R_{DA} of each sample through the interpolation curve that is generated with the literature data.

4.4.2. The change in NFRET profiles under different hemin concentrations

The NFRET calculations of samples are carried out using Eqn. 9 where the nFRET is normalized with square root of I_{CFP} and I_{YFP} multiplication. The statistical significance of the NFRET difference between deficient and excess hemin conditions are assessed for each sample. Two-sample Kolmogorov-Smirnov test is employed for the statistical analysis where the extrinsic hemin addition is present and not present NFRET vector matrices of each sample are provided as continuous distributions for a population.

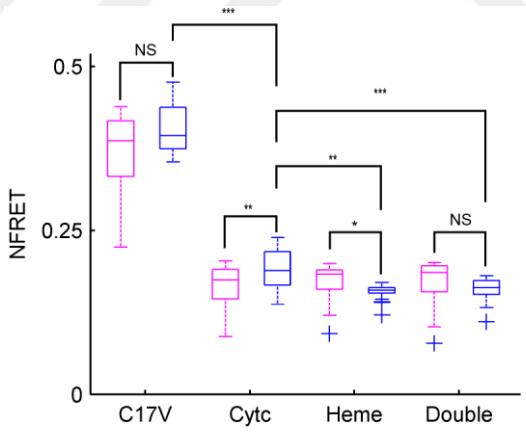

Figure 4-11 : The box plot of NFRET distributions of each sample where the extrinsic addition of hemin cofactor is present (blue) and not present (pink). The statistical significance of NFRET distribution differences among two conditions of a sample or two sample for one condition is indicated with asterisks. The P values equal or smaller than 0.05, 0.01, 0.001

were considered as statistically significant and indicated with 1, 2, 3 asterisks, respectively. P values equal to or bigger than 0.05 were acknowledged as statistically not significant (NS).

The positive control sample, C17V, didn't exhibit a significant change with the presence of hemin cofactor which was expected since it doesn't have any tendency or dependence to hemin for its folding or maturation. On the other hand, C-Cyt *c*-V sample demonstrated a significant increase in its NFRET value due to hemin cofactor mediated increase of its folding which results in higher NFRET signal. The NFRET distribution difference in the catalyzer protein, C-Cyt *c* Heme Lyase-V, was not as significant as C-Cyt *c*-V's NFRET change and its average NFRET value didn't shifted above due to hemin presence. This result suggests the independent folding and maturation of C-Cyt *c* Heme Lyase-V which probably doesn't have an affinity for hemin attachment or presence.

Much to our surprise, the double transfect of C-Cyt *c*-V and C-Cyt *c* Heme Lyase-V constructs didn't indicate a significant rise in the hemin added condition. This outcome put forward some theories that are both related with the system limitations and interplay dynamics. Even though C-Cyt *c* Heme Lyase-V protein was expected to facilitate the folding of Cyt *c* by catalyzing the hemin cofactor insertion process, this event could be restricted due to proximity failure which may arouse from the bulky presence of donor and acceptor proteins at the N- and C-termini. The large size of these GFP variant proteins may cause steric hindrance at the cofactor binding site and, therefore, prevent the interplay between Cyt *c* and Cyt *c* Heme Lyase. The second theory can be the relatively limited contribution of the Cyt *c* Heme Lyase catalyzer protein in promoting the folding of Cyt *c*. Similarly, the significant increment in the folding of Cyt c under excess hemin cofactor but absence of catalyzer protein supports this theory. Apart from these possibilities, the hemin binding affinity of Cyt *c* Heme

Lyase could be higher than Cyt *c*'s and this may interdict with the hemin access of Cyt c since its competitor is more advantageous.

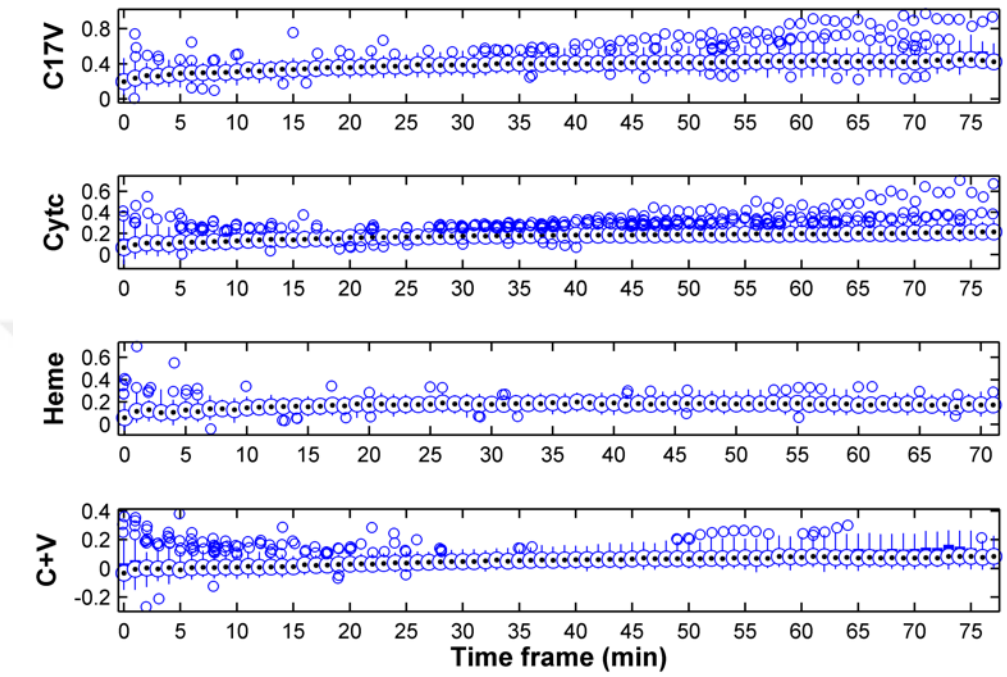

Figure 4-12 : The box plot of frame by frame NFRET values of each sample.

4.4.3. The effect of non-specific donor and acceptor interactions on NFRET measurements

The donor and acceptor fluorescence arising from non-FRET events is a major concern in FRET measurements since they may lead to miscalculations. The non-FRET events arise due to non-specific interactions between donor and acceptor fluorophores different than their convergence due to FRET.

The number of expressed donor and acceptor proteins increase in time and the fluorophores start to fall close to each other by means of accelerating molecular crowdedness. Hence, this fortuitous proximity between donor and acceptor protein can invoke non-FRET interactions. The expression of an individual donor or acceptor protein or a FRET pair is relatively straightforward compared to a FRET construct since it requires the successive

folding of the protein of interest to induce the approaching of donor and acceptor fluorophores. Therefore, the FRET pairs or donor and acceptor constructs can easily increase their fluorescence emission with their smooth expression dynamics until they reach a saturation point.

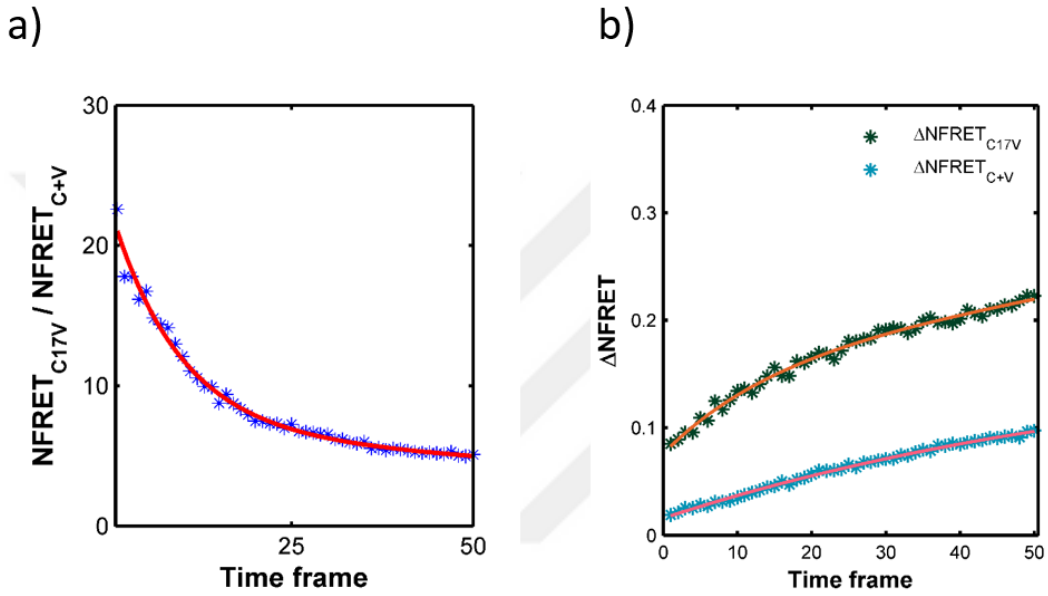

Figure 4-13 : The NFRET dynamics of FRET pairs and donor and acceptor coexisting samples. a) NFRET ratio of C17V FRET pair to Cerulean and Venus double transfect sample b) ΔNFRET profiles of C17V and Cerulean&Venus samples throughout the experiment duariton.

Chapter 5 : CONCLUSION AND OUTLOOK

In this thesis, I have demonstrated a genetically encoded method to determine the redox state of Cyt *c* and studied the role of Heme Lyase and hemin insertion on Cyt *c* folding in vitro by fluorescence resonance energy transfer. The first approach is the redox state monitoring of Cyt *c* using pcFRET method where direct and continuous redox measurements were carried out in purified microbial proteins. A fluorescent protein, Venus, attached to C-termini of the Cyt *c* for reporting the instantaneous oxidation state of Cyt *c* through its emission altering. The strategy of composing this genetic design was creating a spectral overlap between the emission of the donor, Venus, and the absorption of the acceptor, Cyt *c*, that changes with the redox state. The spectral overlap benefitting property of pcFRET technique is utilized for indicating the redox state of Cyt *c* via emission of Venus which is quenched at reduced Cyt *c* and bright at oxidized Cyt *c* form.

pcFRET method was used to determine the redox state in bulk purified protein samples, but further studies can be carried out to observe the Cyt *c* dynamics in biological systems. The redox activity of Cyt *c* in cells may affected by its interactions with other proteins, or, most significantly, due to the presence of a membrane potential that therefore remains uncertain. The binding of IP3R protein to Cyt *c* was known to initiate Ca^{2+} release from ER, but its role of Cyt *c* oxidation state remains unclear. The sensitivity of Cyt *c* redox cycle to mitochondrial membrane potential may be measured simultaneously by two-color fluorescence imaging where a small molecule probe, GCaMP or PROPS may be used as a voltage indicator.

Cyt *c*-Venus probe may also be used to indicate the energy metabolism within the cell, therefore it can be used to detect small compounds and peptides that would inhibit the oxidase or reductase activity that affects the apoptosis mechanism. However, it requires an optimization for synthesis and sensitivity desired in vitro studies. It is currently characterized by the delocalization of GFP labeled Cyt *c* from mitochondria. The immediate oxidation state changes of Cyt c, if occurs during these events, has been far less studied due to lack of sensitive and specific molecular probes. Therefore, the demonstrated tool could expand the scope of the photochromic fluorescent method to monitor heme protein dynamics.

The measurements of Cyt *c* redox activity will provide a crucial information about the redox state of the protein where the changes affect the function of Cyt *c* and plays a role for cellular decision. Although Venus was used as a photochromic FRET acceptor, mBanana that has emission maxima at 553 nm can be fused to Cyt *c*. Moreover the linker composed by three alanine residues between the Cyt *c* and Venus can be shortened as a means to increase the magnitude of pcFRET signal. Such constructs may enable the fluorescence signal-to-noise ratio of redox dynamics inside living cells where the ΔFluorescence/Fluorescence has to be maximized.

Novel approaches such as directed molecular evolution approach can accelerate the search for finding an optimized Cyt *c*-Venus molecular probe, therefore higher pcFRET signal may be collected from Cyt *c*-Venus probe. The use of pcFRET for detecting redox activity could be used to detect other biologically important heme proteins such as Cytochrome P450 (Cyt P450) that is essential for the oxidation of organic compounds. One could use a fluorescent protein labeled Cyt P450 to detect changes in its activity.

As mentioned before, Cyt *c* is a key player in mitochondrial biogenesis due to its crucial presence in the completion of electron transport chain through respiration and

apoptosis cascade initialization where these two mechanisms are highly related with the maintenance of redox homeostasis in living systems. However, the folding of Cyt *c* followed by its maturation still remains elusive and the interplay between the components of this mechanism is still not fully understood.

In the second study, we introduced a quantitative monitoring method to study the folding dynamics of Cyt *c* in the presence of catalyzer protein Cyt *c* Heme Lyase and hemin cofactor as the prosthetic group. A conventional technique, FRET, was employed for reporting the folding event which causes a convergence in the molecular structure. The FRET signals retrieved from the living cells as a sign of successive folding, are analyzed through a custom written script that reduces the ambiguity due to protein expression heterogeneity, cell motility, and photobleaching.

The novel FRET computation method was described to calculate the nFRET from rFRET data by subtracting the donor and acceptor fluorescence intensities multiplied with their corresponding coefficients. Conventionally, these coefficient are considered as static values for live experiments and calculated from one frame only. In this work, we generated dynamic correction coefficients by taking the ratio of the FRET signal to acceptor or donor signal for each frame throughout the experiment time. By doing this, the instantaneous and single cell specific nFRET values are calculated with a reliable accuracy, considering the fluorescence decay of fluorophores and its contribution to measured FRET efficiency.

The magnitude of the retrieved FRET signal can be augmented through truncated version of Cyt *c* and Cyt *c* Heme Lyase proteins where the critical hemin attachment and folding facilitator sites are preserved. This signal enhancement could be useful for studying Cyt *c* dynamics in some model organism such as *C. elegance*, zebrafish, drosophila where

higher signals should be obtained to monitor the redox events in 3D geometry of the whole biological integrity.

As a future work the generated recombinant DNA designs can be transferred to a bacterial expression backbone for studying the Cyt *c* folding dynamics in *E.Coli* and purified microbial proteins. Since Cyt *c* biogenesis defers between different organism groups the proposed method can be used for monitoring the Cyt c maturation process in other less complex systems.

In continuation of the work presented here, the quantitative contribution of the hemin cofactor and Cyt *c* Heme Lyase catalyzer protein in folding and maturation of Cyt *c* will be examined through Western Blot analysis for assessing the synthesized protein amount under different protein, catalyzer, and cofactor conditions with varying concentrations. Furthermore, it is planned to introduce a mutation in one of the cysteine residues that enables the covalent attachment of hemin cofactor to chromophore site via thiol bonds. The strategy behind this molecular modification is to generate a concentration based hemin sensor for Cyt *c* where hemin attachment partially occurs through thiol bond of one active cysteine residue. Therefore, the presence of excess hemin concentration would assist more folding evets, whereas less hemin concentration will shift the equilibrium in the reverse direction and result in less number of or not folded Cyt *c* proteins. The proposed methodology can be utilized in other small molecule attachment mediated folding of proteins.

BIBLIOGRAPHY

1. Kholodenko, B. N., Hancock, J. F. & Kolch, W. Signalling ballet in space and time. *Nat. Rev. Mol. Cell Biol.* **11,** 414–426 (2010).
2. Scott, J. D. & Pawson, T. Cell Signaling in Space and Time: Where Proteins Come Together and When They're Apart.
3. Brown, M. D. & Sacks, D. B. Protein scaffolds in MAP kinase signalling. *Cell. Signal.* **21,** 462–9 (2009).
4. Kolch, W. Coordinating ERK/MAPK signalling through scaffolds and inhibitors. *Nat. Rev. Mol. Cell Biol.* **6,** 827–37 (2005).
5. Dehmelt, L. & Bastiaens, P. I. H. Spatial organization of intracellular communication: insights from imaging. *Nat. Rev. Mol. Cell Biol.* **11,** 440–452 (2010).
6. Pan, C. Q., Sudol, M., Sheetz, M. & Low, B. C. Modularity and functional plasticity of scaffold proteins as p(l)acemakers in cell signaling. *Cell. Signal.* **24,** 2143–65 (2012).
7. Sample, V. *et al.* Genetically encoded molecular probes to visualize and perturb signaling dynamics in living biological systems. *J. Cell Sci.* **127,** 1151–60 (2014).
8. Dean, K. M. & Palmer, A. E. Advances in fluorescence labeling strategies for dynamic cellular imaging. *Nat. Chem. Biol.* **10,** 512–23 (2014).
9. Lohr, C. Monitoring neuronal calcium signalling using a new method for ratiometric confocal calcium imaging. *Cell Calcium* **34,** 295–303 (2003).
10. Ettinger, A. & Wittmann, T. Fluorescence live cell imaging. *Methods Cell Biol.* **123,** 77–94 (2014).
11. Shimomura, O. Discovery of green fluorescent protein (GFP) (Nobel Lecture). *Angew. Chem. Int. Ed. Engl.* **48,** 5590–602 (2009).
12. Chalfie, M., Tu, Y., Euskirchen, G., Ward, W. W. & Prasher, D. C. Green fluorescent protein as a marker for gene expression. *Science* **263,** 802–5 (1994).
13. Prasher, D. C., Eckenrode, V. K., Ward, W. W., Prendergast, F. G. & Cormier, M. J. Primary structure of the Aequorea victoria green-fluorescent protein. *Gene* **111,** 229–

33 (1992).

14. Tsien, R. Y. The green fluorescent protein. *Annu. Rev. Biochem.* **67,** 509–44 (1998).
15. Olenych, S. G., Claxton, N. S., Ottenberg, G. K. & Davidson, M. W. The fluorescent protein color palette. *Curr. Protoc. Cell Biol.* **Chapter 21,** Unit 21.5 (2007).
16. Schmid, J. A. & Neumeier, H. Evolutions in Science Triggered by Green Fluorescent Protein (GFP). *ChemBioChem* **6,** 1149–1156 (2005).
17. Balla, T. Green light to illuminate signal transduction events. *Trends Cell Biol.* **19,** 575–86 (2009).
18. Tantama, M., Hung, Y. P. & Yellen, G. Optogenetic reporters: Fluorescent protein-based genetically encoded indicators of signaling and metabolism in the brain. *Prog. Brain Res.* **196,** 235–63 (2012).
19. Newman, R. H., Fosbrink, M. D. & Zhang, J. Genetically encodable fluorescent biosensors for tracking signaling dynamics in living cells. *Chem. Rev.* **111,** 3614–66 (2011).
20. Gray, A., Van der Kaay, J. & Downes, C. P. The pleckstrin homology domains of protein kinase B and GRP1 (general receptor for phosphoinositides-1) are sensitive and selective probes for the cellular detection of phosphatidylinositol 3,4-bisphosphate and/or phosphatidylinositol 3,4,5-trisphosphate. *Biochem Jounal* **344,** 929–936 (1999).
21. Nakai, J., Ohkura, M. & Imoto, K. A high signal-to-noise Ca2+ probe composed of a single green fluorescent protein. *Nat. Biotechnol.* **19,** 137–141 (2001).
22. Akerboom, J. *et al.* Crystal structures of the GCaMP calcium sensor reveal the mechanism of fluorescence signal change and aid rational design. *J. Biol. Chem.* **284,** 6455–64 (2009).
23. Zhao, Y. *et al.* An expanded palette of genetically encoded Ca^{2+} indicators. *Science* **333,** 1888–91 (2011).
24. Akerboom, J. *et al.* Genetically encoded calcium indicators for multi-color neural activity imaging and combination with optogenetics. *Front. Mol. Neurosci.* **6,** 2 (2013).
25. Ibraheem, A. & Campbell, R. E. Designs and applications of fluorescent protein-based biosensors. *Curr. Opin. Chem. Biol.* **14,** 30–36 (2010).
26. Campbell, R. E. Fluorescent-Protein-Based Biosensors: Modulation of Energy Transfer as a Design Principle. *Anal. Chem.* **81,** 5972–5979 (2009).

27. Zaccolo, M. Use of chimeric fluorescent proteins and fluorescence resonance energy transfer to monitor cellular responses. *Circ. Res.* **94,** 866–73 (2004).
28. Hochreiter, B., Garcia, A. P. & Schmid, J. A. Fluorescent proteins as genetically encoded FRET biosensors in life sciences. *Sensors (Basel).* **15,** 26281–314 (2015).
29. Fritz, R. D. *et al.* A Versatile Toolkit to Produce Sensitive FRET Biosensors to Visualize Signaling in Time and Space. *Sci. Signal.* **6,** (2013).
30. Zhang, J., Ma, Y., Taylor, S. S. & Tsien, R. Y. Genetically encoded reporters of protein kinase A activity reveal impact of substrate tethering. *Proc. Natl. Acad. Sci. U. S. A.* **98,** 14997–5002 (2001).
31. Violin, J. D., Zhang, J., Tsien, R. Y. & Newton, A. C. A genetically encoded fluorescent reporter reveals oscillatory phosphorylation by protein kinase C. *J. Cell Biol.* **161,** 899–909 (2003).
32. Harvey, C. D. *et al.* A genetically encoded fluorescent sensor of ERK activity. *Proc. Natl. Acad. Sci. U. S. A.* **105,** 19264–9 (2008).
33. Spencer, D. M., Wandless, T. J., Schreiber, S. L. & Crabtree, G. R. Controlling signal transduction with synthetic ligands. *Science* **262,** 1019–24 (1993).
34. Crabtree, G. R. & Schreiber, S. L. Three-part inventions: intracellular signaling and induced proximity. *Trends Biochem. Sci.* **21,** 418–22 (1996).
35. DeRose, R., Miyamoto, T. & Inoue, T. Manipulating signaling at will: chemically-inducible dimerization (CID) techniques resolve problems in cell biology. *Pflügers Arch. Eur. J. Physiol.* **465,** 409–17 (2013).
36. Umeda, N., Ueno, T., Pohlmeyer, C., Nagano, T. & Inoue, T. A Photocleavable Rapamycin Conjugate for Spatiotemporal Control of Small GTPase Activity. *J. Am. Chem. Soc.* **133,** 12–14 (2011).
37. Inoue, T., Heo, W. Do, Grimley, J. S., Wandless, T. J. & Meyer, T. An inducible translocation strategy to rapidly activate and inhibit small GTPase signaling pathways. *Nat. Methods* **2,** 415–418 (2005).
38. Karginov, A. V, Ding, F., Kota, P., Dokholyan, N. V & Hahn, K. M. Engineered allosteric activation of kinases in living cells. *Nat. Biotechnol.* **28,** 743–747 (2010).
39. Tischer, D. & Weiner, O. D. Illuminating cell signalling with optogenetic tools. *Nat. Publ. Gr.* **15,** (2014).

40. Fenno, L., Yizhar, O. & Deisseroth, K. The development and application of optogenetics. *Annu. Rev. Neurosci.* **34,** 389–412 (2011).
41. Gautier, A. *et al.* How to control proteins with light in living systems. *Nat. Chem. Biol.* **10,** 533–541 (2014).
42. Nagel, G. *et al.* Channelrhodopsin-2, a directly light-gated cation-selective membrane channel. *Proc. Natl. Acad. Sci. U. S. A.* **100,** 13940–13945 (2003).
43. Zhang, F. *et al.* Multimodal fast optical interrogation of neural circuitry. *Nature* **446,** 633–639 (2007).
44. Nagel, G. *et al.* Channelrhodopsins: directly light-gated cation channels. *Biochem. Soc. Trans.* **33,** 863–6 (2005).
45. Zhang, F. *et al.* The Microbial Opsin Family of Optogenetic Tools. *Cell* **147,** 1446–1457 (2011).
46. Bruegmann, T. *et al.* Optogenetic control of heart muscle in vitro and in vivo. *Nat. Methods* **7,** 897–900 (2010).
47. Stroh, A. *et al.* Tracking stem cell differentiation in the setting of automated optogenetic stimulation. *Stem Cells* **29,** 78–88 (2011).
48. Boyden, E. S., Zhang, F., Bamberg, E., Nagel, G. & Deisseroth, K. Millisecond-timescale, genetically targeted optical control of neural activity. *Nat. Neurosci.* **8,** 1263–8 (2005).
49. Kralj, J. M., Douglass, A. D., Hochbaum, D. R., Maclaurin, D. & Cohen, A. E. Optical recording of action potentials in mammalian neurons using a microbial rhodopsin. *Nat. Methods* **9,** 90–95 (2011).
50. Shcherbakova, D. M., Shemetov, A. A., Kaberniuk, A. A. & Verkhusha, V. V. Natural photoreceptors as a source of fluorescent proteins, biosensors, and optogenetic tools. *Annu. Rev. Biochem.* **84,** 519–50 (2015).
51. Wu, Y. I. *et al.* A genetically encoded photoactivatable Rac controls the motility of living cells. *Nature* **461,** 104–8 (2009).
52. Wang, X., He, L., Wu, Y. I., Hahn, K. M. & Montell, D. J. Light-mediated activation reveals a key role for Rac in collective guidance of cell movement in vivo. *Nat. Cell Biol.* **12,** 591–7 (2010).
53. Yoo, S. K. *et al.* Differential regulation of protrusion and polarity by PI3K during

neutrophil motility in live zebrafish. *Dev. Cell* **18,** 226–36 (2010).

54. Gautier, A. *et al.* Genetically encoded photocontrol of protein localization in mammalian cells. *J. Am. Chem. Soc.* **132,** 4086–8 (2010).
55. Levskaya, A., Weiner, O. D., Lim, W. A. & Voigt, C. A. Spatiotemporal control of cell signalling using a light-switchable protein interaction. *Nature* **461,** 997–1001 (2009).
56. Zhou, X. X. *et al.* Optical control of protein activity by fluorescent protein domains. *Science* **338,** 810–4 (2012).
57. Toettcher, J. E., Gong, D., Lim, W. A. & Weiner, O. D. Light-based feedback for controlling intracellular signaling dynamics. *Nat. Methods* **8,** 837–9 (2011).
58. Thevathasan, J. V. *et al.* The small GTPase HRas shapes local PI3K signals through positive feedback and regulates persistent membrane extension in migrating fibroblasts. *Mol. Biol. Cell* **24,** 2228–37 (2013).
59. Petreanu, L., Huber, D., Sobczyk, A. & Svoboda, K. Channelrhodopsin-2-assisted circuit mapping of long-range callosal projections. *Nat. Neurosci.* **10,** 663–8 (2007).
60. Prigge, M. *et al.* Color-tuned channelrhodopsins for multiwavelength optogenetics. *J. Biol. Chem.* **287,** 31804–12 (2012).
61. Ohkura, M. *et al.* An Improved Genetically Encoded Red Fluorescent Ca2+ Indicator for Detecting Optically Evoked Action Potentials. *PLoS One* **7,** e39933 (2012).
62. Wu, J. *et al.* Improved Orange and Red Ca $^{2+}$ Indicators and Photophysical Considerations for Optogenetic Applications. *ACS Chem. Neurosci.* **4,** 963–972 (2013).
63. Ursini, F., Maiorino, M. & Forman, H. J. Redox homeostasis: The Golden Mean of healthy living. *Redox Biol.* **8,** 205–215 (2016).
64. Circu, M. L. & Aw, T. Y. Reactive oxygen species, cellular redox systems, and apoptosis. *Free Radic. Biol. Med.* **48,** 749–62 (2010).
65. Sohal, R. S. & Orr, W. C. The Redox Stress Hypothesis of Aging. doi:10.1016/j.freeradbiomed.2011.10.445
66. Limongi, D. & Baldelli, S. Redox Imbalance and Viral Infections in Neurodegenerative Diseases. *Oxid. Med. Cell. Longev.* **2016,** 6547248 (2016).
67. Liu, Y. *et al.* Cancer drug resistance: redox resetting renders a way. *Oncotarget* (2016). doi:10.18632/oncotarget.8600
68. Stangherlin, A. & Reddy, A. B. Regulation of circadian clocks by redox homeostasis.

J. Biol. Chem. **288,** 26505–11 (2013).

69. Piantadosi, C. A. & Suliman, H. B. Redox regulation of mitochondrial biogenesis. *Free Radic. Biol. Med.* **53,** 2043–2053 (2012).
70. Shadel, G. S. & Horvath, T. L. Mitochondrial ROS Signaling in Organismal Homeostasis. *Cell* **163,** 560–569 (2015).
71. Scarpulla, R. C. Transcriptional activators and coactivators in the nuclear control of mitochondrial function in mammalian cells. *Gene* **286,** 81–89 (2002).
72. Yoboue, E. D. *et al.* The role of mitochondrial biogenesis and ROS in the control of energy supply in proliferating cells. *Biochim. Biophys. Acta - Bioenerg.* **1837,** 1093–1098 (2014).
73. Nickel, A., Kohlhaas, M. & Maack, C. Mitochondrial reactive oxygen species production and elimination. *J. Mol. Cell. Cardiol.* **73,** 26–33 (2014).
74. West, A. P., Shadel, G. S. & Ghosh, S. Mitochondria in innate immune responses. *Nat. Rev. Immunol.* **11,** 389–402 (2011).
75. Murphy, M. P. How mitochondria produce reactive oxygen species. *Biochem. J.* **417,** 1–13 (2009).
76. Cherry, A. D. & Piantadosi, C. A. Regulation of Mitochondrial Biogenesis and Its Intersection with Inflammatory Responses. *Antioxidants Redox Signal.* **22,** 965–976 (2015).
77. Chen, Y., Zhang, H., Zhou, H., Ji, W. & Min, W. Mitochondrial Redox Signaling and Tumor Progression. *Cancers (Basel).* **8,** 40 (2016).
78. Daiber, A. Redox signaling (cross-talk) from and to mitochondria involves mitochondrial pores and reactive oxygen species. *Biochim. Biophys. Acta - Bioenerg.* **1797,** 897–906 (2010).
79. Kalogeris, T., Bao, Y. & Korthuis, R. J. Mitochondrial reactive oxygen species: A double edged sword in ischemia/reperfusion vs preconditioning. *Redox Biol.* **2,** 702–714 (2014).
80. Giegé, P., Grienenberger, J. M. & Bonnard, G. Cytochrome c biogenesis in mitochondria. *Mitochondrion* **8,** 61–73 (2008).
81. Babbitt, S. E., Sutherland, M. C., San Francisco, B., Mendez, D. L. & Kranz, R. G. Mitochondrial cytochrome c biogenesis: no longer an enigma. *Trends Biochem. Sci.* **40,**

446–55 (2015).

82. Hüttemann, M. *et al.* The multiple functions of cytochrome c and their regulation in life and death decisions of the mammalian cell: From respiration to apoptosis. *Mitochondrion* **11,** 369–81 (2011).
83. Welchen, E. & Gonzalez, D. H. Cytochrome c, a hub linking energy, redox, stress and signaling pathways in mitochondria and other cell compartments. *Physiol. Plant.* (2016). doi:10.1111/ppl.12449
84. Bertini, I., Cavallaro, G. & Rosato, A. Cytochrome *c* : Occurrence and Functions. *Chem. Rev.* **106,** 90–115 (2006).
85. Travaglini-Allocatelli, C. & Travaglini-Allocatelli, C. Protein Machineries Involved in the Attachment of Heme to Cytochrome c: Protein Structures and Molecular Mechanisms. *Scientifica (Cairo).* **2013,** 1–17 (2013).
86. Zaidi, S., Hassan, M. I., Islam, A. & Ahmad, F. The role of key residues in structure, function, and stability of cytochrome-c. *Cell. Mol. Life Sci.* **71,** 229–55 (2014).
87. Hamel, P., Corvest, V., Giegé, P. & Bonnard, G. Biochemical requirements for the maturation of mitochondrial c-type cytochromes. *Biochim. Biophys. Acta - Mol. Cell Res.* **1793,** 125–138 (2009).
88. Gray, H. B. & Winkler, J. R. Electron flow through metalloproteins. *Biochim. Biophys. Acta - Bioenerg.* **1797,** 1563–1572 (2010).
89. Tuominen, E. K. *et al.* ATP induces a conformational change in lipid-bound cytochrome c. *J. Biol. Chem.* **276,** 19356–62 (2001).
90. Welchen, E., García, L., Mansilla, N. & Gonzalez, D. H. Coordination of plant mitochondrial biogenesis: keeping pace with cellular requirements. *Front. Plant Sci.* **4,** 551 (2014).
91. Li, K. *et al.* Cytochrome c deficiency causes embryonic lethality and attenuates stress-induced apoptosis. *Cell* **101,** 389–99 (2000).
92. Martínez-Fábregas, J., Díaz-Moreno, I., González-Arzola, K., Díaz-Quintana, A. & De la Rosa, M. A. A common signalosome for programmed cell death in humans and plants. *Cell Death Dis.* **5,** e1314 (2014).
93. Ow, Y.-L. P., Green, D. R., Hao, Z. & Mak, T. W. Cytochrome c: functions beyond respiration. *Nat. Rev. Mol. Cell Biol.* **9,** 532–542 (2008).

94. Riemer, J., Fischer, M. & Herrmann, J. M. Oxidation-driven protein import into mitochondria: Insights and blind spots. *Biochim. Biophys. Acta* **1808,** 981–9 (2011).

95. Vempati, U. D., Han, X. & Moraes, C. T. Lack of Cytochrome c in Mouse Fibroblasts Disrupts Assembly/Stability of Respiratory Complexes I and IV. *J. Biol. Chem.* **284,** 4383–4391 (2009).

96. Van Aken, O. *et al.* Licensed to Kill: Mitochondria, Chloroplasts, and Cell Death. *Trends Plant Sci.* **20,** 754–766 (2015).

97. Nicholls, P. Cytochrome *c* A Multidisciplinary Approach Edited by R. A. Scott (University of Georgia) and A. G. Mauk (University of British Columbia). University Science Books: Sausalito, CA. 1996. vi + 738 pp. $85.00. ISBN 0-935702-33-4. *J. Am. Chem. Soc.* **118,** 9459–9460 (1996).

98. Brown, G. C. & Borutaite, V. Regulation of apoptosis by the redox state of cytochrome c. *Biochim. Biophys. Acta - Bioenerg.* **1777,** 877–881 (2008).

99. Hollis, V. S., Palacios-Callender, M., Springett, R. J., Delpy, D. T. & Moncada, S. Monitoring cytochrome redox changes in the mitochondria of intact cells using multi-wavelength visible light spectroscopy. *Biochim. Biophys. Acta - Bioenerg.* **1607,** 191–202 (2003).

100. Garrido, C. *et al.* Mechanisms of cytochrome c release from mitochondria. *Cell Death Differ.* **13,** 1423–33 (2006).

101. Llopis, J., McCaffery, J. M., Miyawaki, A., Farquhar, M. G. & Tsien, R. Y. Measurement of cytosolic, mitochondrial, and Golgi pH in single living cells with green fluorescent proteins. *Proc. Natl. Acad. Sci. U. S. A.* **95,** 6803–8 (1998).

102. Ott, M., Robertson, J. D., Gogvadze, V., Zhivotovsky, B. & Orrenius, S. Cytochrome c release from mitochondria proceeds by a two-step process. *Proc. Natl. Acad. Sci. U. S. A.* **99,** 1259–63 (2002).

103. Cottet-Rousselle, C., Ronot, X., Leverve, X. & Mayol, J.-F. Cytometric assessment of mitochondria using fluorescent probes. *Cytometry. A* **79,** 405–25 (2011).

104. Scaduto, R. C. & Grotyohann, L. W. Measurement of mitochondrial membrane potential using fluorescent rhodamine derivatives. *Biophys. J.* **76,** 469–77 (1999).

105. Miller, E. W., Bian, S. X. & Chang, C. J. A fluorescent sensor for imaging reversible redox cycles in living cells. *J. Am. Chem. Soc.* **129,** 3458–9 (2007).

106. Kuznetsova, S. *et al.* A Förster-resonance-energy transfer-based method for fluorescence detection of the protein redox state. *Anal. Biochem.* **350,** 52–60 (2006).
107. Jiang, X. & Wang, X. Cytochrome C-mediated apoptosis. *Annu. Rev. Biochem.* **73,** 87–106 (2004).
108. JM, S., T, U., O, D. & SJ, F. Covalent cofactor attachment to proteins: cytochrome c biogenesis. *Biochem. Soc. Trans.* **33,** 792–795 (2005).
109. Bowman, S. E. J. & Bren, K. L. The chemistry and biochemistry of heme c: functional bases for covalent attachment. *Nat. Prod. Rep.* **25,** 1118–30 (2008).
110. San Francisco, B., Bretsnyder, E. C. & Kranz, R. G. Human mitochondrial holocytochrome c synthase's heme binding, maturation determinants, and complex formation with cytochrome c. *Proc. Natl. Acad. Sci. U. S. A.* **110,** E788–97 (2013).
111. Kleingardner, J. G. & Bren, K. L. Comparing substrate specificity between cytochrome c maturation and cytochrome c heme lyase systems for cytochrome c biogenesis. *Metallomics* **3,** 396–403 (2011).
112. Can, M., Zoppellaro, G., Andersson, K. K. & Bren, K. L. Modulation of ligand-field parameters by heme ruffling in cytochromes c revealed by EPR spectroscopy. *Inorg. Chem.* **50,** 12018–24 (2011).
113. Murgida, D. H. & Hildebrandt, P. Electron-transfer processes of cytochrome C at interfaces. New insights by surface-enhanced resonance Raman spectroscopy. *Acc. Chem. Res.* **37,** 854–61 (2004).
114. Okada, M. *et al.* Label-free Raman observation of cytochrome c dynamics during apoptosis. *Proc. Natl. Acad. Sci. U. S. A.* **109,** 28–32 (2012).
115. Nagai, Y. *et al.* A fluorescent indicator for visualizing cAMP-induced phosphorylation in vivo. *Nat. Biotechnol.* **18,** 313–6 (2000).
116. Lee, A. J., Ensign, A. A., Krauss, T. D. & Bren, K. L. Zinc porphyrin as a donor for FRET in Zn(II)cytochrome c. *J. Am. Chem. Soc.* **132,** 1752–3 (2010).
117. Kuznetsova, S. *et al.* The enzyme mechanism of nitrite reductase studied at single-molecule level. *Proc. Natl. Acad. Sci. U. S. A.* **105,** 3250–5 (2008).
118. Jares-Erijman, E. A. & Jovin, T. M. FRET imaging. *Nat. Biotechnol.* **21,** 1387–95 (2003).
119. Bayraktar, H. *et al.* Ultrasensitive measurements of microbial rhodopsin photocycles

using photochromic FRET. *Photochem. Photobiol.* **88,** 90–7

120. Selvin, P. R. The renaissance of fluorescence resonance energy transfer. *Nat. Struct. Biol.* **7,** 730–4 (2000).
121. Manioglu, S. *et al.* Direct conversion of Cytochrome c spectral shifts to fluorescence using photochromic FRET. *Chem. Commun.* **50,** 12333–12336 (2014).
122. Valeur, B. & Berberan-Santos, M. N. *Molecular Fluorescence: Principles and Applications*. (Wiley-VCH Verlag & Co. KGaA, 2012). doi:10.1002/9783527650002
123. Shaner, N. C., Steinbach, P. A. & Tsien, R. Y. A guide to choosing fluorescent proteins. *Nat. Methods* **2,** 905–9 (2005).
124. Banci, L. *et al.* Solution Structure of Oxidized *Saccharomyces cerevisiae* Iso-1-cytochrome *c* †, ‡. *Biochemistry* **36,** 8992–9001 (1997).
125. Baistrocchi, P. *et al.* Three-Dimensional Solution Structure of *Saccharomyces cerevisiae* Reduced Iso-1-cytochrome *c* †. *Biochemistry* **35,** 13788–13796 (1996).
126. Verissimo, A. F. & Daldal, F. Cytochrome c biogenesis System I: An intricate process catalyzed by a maturase supercomplex? *Biochim. Biophys. Acta - Bioenerg.* **1837,** 989–998 (2014).
127. Pollock, W. B., Rosell, F. I., Twitchett, M. B., Dumont, M. E. & Mauk, A. G. Bacterial expression of a mitochondrial cytochrome c. Trimethylation of lys72 in yeast iso-1-cytochrome c and the alkaline conformational transition. *Biochemistry* **37,** 6124–31 (1998).
128. Ascenzi, P., Santucci, R., Coletta, M. & Polticelli, F. Cytochromes: Reactivity of the ‘dark side’ of the heme. *Biophys. Chem.* **152,** 21–27 (2010).
129. Asher, W. B. *et al.* Cytochrome c heme lyase can mature a fusion peptide composed of the amino-terminal residues of horse cytochrome c. *Chem. Commun.* **48,** 8344 (2012).
130. Kurchan, E., Roder, H. & Bowler, B. E. Kinetics of loop formation and breakage in the denatured state of iso-1-cytochrome c. *J. Mol. Biol.* **353,** 730–43 (2005).
131. Hoppe, A., Christensen, K. & Swanson, J. A. Fluorescence resonance energy transfer-based stoichiometry in living cells. *Biophys. J.* **83,** 3652–64 (2002).
132. Xia, Z. & Liu, Y. Reliable and global measurement of fluorescence resonance energy transfer using fluorescence microscopes. *Biophys. J.* **81,** 2395–402 (2001).
133. Jares-Erijman, E. A. & Jovin, T. M. Imaging molecular interactions in living cells by

FRET microscopy. *Curr. Opin. Chem. Biol.* **10,** 409–416 (2006).

134. Berney, C. & Danuser, G. FRET or no FRET: a quantitative comparison. *Biophys. J.* **84,** 3992–4010 (2003).
135. Gordon, G. W., Berry, G., Liang, X. H., Levine, B. & Herman, B. Quantitative fluorescence resonance energy transfer measurements using fluorescence microscopy. *Biophys. J.* **74,** 2702–13 (1998).
136. Zeug, A., Woehler, A., Neher, E. & Ponimaskin, E. G. Quantitative intensity-based FRET approaches--a comparative snapshot. *Biophys. J.* **103,** 1821–7 (2012).
137. Massey, F. J. The Kolmogorov-Smirnov Test for Goodness of Fit. *Source J. Am. Stat. Assoc.* **46,** 68–78 (1951).
138. Miller, L. H. Table of Percentage Points of Kolmogorov Statistics. *J. Am. Stat. Assoc.* **51,** 111 (1956).
139. Marsaglia, G., Tsang, W. W. & Wang, J. Evaluating Kolmogorov's Distribution. *J. Stat. Softw.* **8,** 1–4 (2003).
140. Vogel, S. S., van der Meer, B. W. & Blank, P. S. Estimating the distance separating fluorescent protein FRET pairs. *Methods* **66,** 131–8 (2014).